TEST MASS METROLOGY FOR TESTS OF THE EQUIVALENCE PRINCIPLE

by

SACHIE SHIOMI

A thesis submitted to
The University of Birmingham
for the degree of
DOCTOR OF PHILOSOPHY

Birmingham Gravitation Group
School of Physics and Astronomy
The University of Birmingham
March 2002

Abstract

The Equivalence Principle is accepted as one of the most fundamental principles in modern Physics. However, theories towards the unification of the four forces typically predict violations of this principle. Testing it at a high sensitivity is expected to make a breakthrough in the current understanding of Physics.

A space-based project, STEP (Satellite Test of the Equivalence Principle), aims at testing the principle to the level of 10^{-18}. This corresponds to an improvement of the current limits, established by ground-based experiments, by approximately five orders of magnitudes. To achieve the sensitivity, imperfections in STEP test masses, such as density inhomogeneity and thermal distortion, could be a problem.

This thesis presents preliminary work on the verification of STEP test masses. We have measured density inhomogeneities in materials intended to be used as STEP test masses (beryllium and niobium). In addition, we have developed a device to measure differential thermal expansion of samples that cannot be machined, by using a capacitive sensing method. It is shown that the device has a precision of approximately 0.3 % in the differential thermal expansion of beryllium. This device could in principle be applied for the measurements of the real STEP test masses in the final shape. Our analysis based on the results of our measurements and literature survey shows that it is feasible to obtain materials that satisfy STEP requirements.

Acknowledgements

First of all, I would like to thank my supervisor, Dr C. C. Speake, for giving me the opportunity to work in the field of Gravitational Physics, which I found very interesting. Through the work presented in this thesis, I have learnt many essential skills for an experimentalist. I appreciate his sincere advices and encouragements, throughout this work and during the preparation for this thesis. He gave me many comments on this thesis. Through those comments I had many opportunities to learn something new to me and I enjoyed it very much. He arranged a studentship for me to cover my living cost of March 2002. In addition, I am grateful for his help and patience with improvements of my English skills.

I would like to thank all the members of the Birmingham Gravitation group and the STEP team. Especially, I would like to thank my colleagues: Dr C. Trenkel always kindly answered my any questions, such as experimental skills, English and usages of experimental facilities. Also, he read my drafts of this thesis and gave me very useful comments. Mr C.-C. Chang has helped me with computer software. More importantly, he has helped me with the experimental works for the measurements of differential thermal expansion (DTE, Chapter 7), when I needed another hand. It would have been impossible to carry out all the experimental works on my own. Also, I had useful arguments on the three-terminal capacitance bridge with him. I have enjoyed discussion on theoretical physics with Mr A. Pulido-Patón. Dr G. D. Hammond gave me comments on some chapters of this thesis and patiently explained me any details of English expressions.

I would like to thank Dr R. S. Davis for his supervision on the measurements of the density inhomogeneities (Chapter 5) at BIPM (Bureau International des Poids et Mesures). Also, I would like to thank Dr D. K. Gill for his supervision during my visit at Stanford University and for his information throughout the work. He arranged us the samples used for this work.

All the metal pieces needed for the measurements of DTE were manufactured by the main mechanical workshop, the space research mechanical workshop, Mr R. Januszewski at Epsilon and myself under the supervision of Mr A. A. Barnes at the main mechanical workshop. Mr R. Januszewski's quick work was essential at the final stage of the development of the DTE experiment. Liquid helium and liquid nitrogen to cool the experiment of DTE were supplied by the condensed matter workshop. Some of the apparatus used for the experiment of DTE, such as dewars, were originally

developed for the spin-coupling experiment led by Dr C. C. Speake.

Developments of the experiment of DTE were proceeded with useful information from many experts: the glassblowers at School of Chemical Science at this university, Dr K. Kawano and Dr G. Yang at the Institute of Metallurgy and Material Science at this university, and Mr M. Parkhurst at the Engelhard-clal. Also, I had very interesting information on HIPed beryllium from Mr R. A. Paquin at Advanced Materials Consultant, and Mr T. Parsonage and Dr D. E. Dombrowski at Brush Wellman Inc.

The experiment of DTE was funded by Stanford University. Samples used for this work were supplied by Stanford University. I appreciate Mr G. Green at Stanford University for his help to proceed with this work. In addition, I would like to thank Mr G. Green and his wife, Marcia, for their hospitality during my visit at Stanford.

I would like to thank my ex-supervisor, Prof. T. Kishimoto, at Department of Physics, Osaka University, for his outspoken comments on my work throughout my postgraduate research at Osaka University. My experience there was the basis of my research activity here.

I appreciate my friends and house mates who encouraged me all the time when I got tired of working for the experiment that seemed never to work properly.

My study was fully funded by my hard-working parents, Toshio Shiomi and Katsumi Shiomi (except my living cost of March 2002, when I received the studentship). Their dedication and love for their business have been encouraging me all the time and motivating me to work hard for my research.

Finally, I would like to thank my grandparents and all of my families, relatives and ancestors for their support.

Contents

List of Figures

List of Tables

Chapter 1

Introduction

1.1 Equivalence Principle

1.1.1 Weak Equivalence Principle

Newton's law of gravitation can be written as:

$$\vec{F} = m_P \, \vec{g} \tag{1.1}$$

where $\vec{g}$ is a gravitational field and m_P is the mass of a point mass. Bondi called m_P passive gravitational mass[1] [1] to distinguish from the inertial mass, which appears in Newton's second law.

Newton's second law of motion of a point mass can be expressed as:

$$\vec{F} = m_I \, \vec{a} \tag{1.2}$$

where $\vec{a}$ is the acceleration of the inertial mass, m_I.

The passive gravitational mass responds to gravity, while the inertial mass responds

[1]Bondi classified masses into three kinds; inertial, passive and active gravitational mass. The first two are described in Section 1.1.1. The last one is the mass that is the source of gravitational fields. Newton's third law, the law of action and reaction, implies the equality of active and passive gravitational mass.

to the external force which is applied to the mass. The postulate stating that these masses are equivalent for every material is called the Equivalence Principle.

If there is a coordinate system which is freely falling in a homogeneous and static gravitational field, g, Newton's second law of motion of an observer (a point particle) who is in free fall with the coordinate system can be written as follows (see Figure 1.1):

$$m_I a = -m_P g + m_I a_C, \tag{1.3}$$

for the observer himself/herself. Where a is the acceleration of the observer. The second term of the right-hand side of Equation (1.3) corresponds to the fictitious force which originates from the acceleration of the coordinate system, a_C.

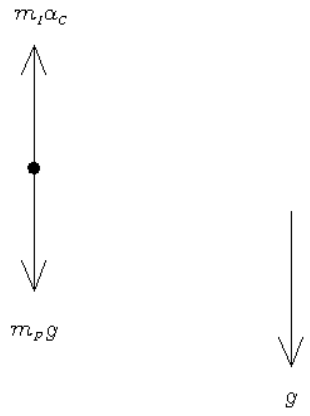

Figure 1.1: Free fall of an observer (a point mass, m) in the gravitational field g.

If it is possible to make the acceleration of the observer zero, $a = 0$, by adjusting the fictitious force, Equation (1.3) reduces to the following condition:

$$\frac{m_P}{m_I} = \frac{a_C}{g} = k, \tag{1.4}$$

where

$$a_C = kg \tag{1.5}$$

and k is a constant.

Therefore, if Equation (1.4) is valid for every material in the coordinate system, that is to say, the ratio of m_P and m_I takes the same value for any material (material 1, material 2, material 3, ...) in the coordinate system:

$$\left(\frac{m_P}{m_I}\right)_1 = \left(\frac{m_P}{m_I}\right)_2 = \left(\frac{m_P}{m_I}\right)_3 = ... = k, \tag{1.6}$$

the observer does not observe the effects of the gravitational field. He/she feels that he/she is in a region free of gravitation. In other words, in the coordinate system, the laws of motion take the same form as in an unaccelerated coordinate system in absence of gravitation. The condition (1.6) expresses the Equivalence Principle.

The value of k is included in the gravitational constant. When one determines the gravitational acceleration (g) by a free-fall experiment, g always includes a coefficient of $1/k$ (Equation (1.5)). The acceleration g is proportional to m_A/r^2, where m_A is the (point) source mass (active gravitational mass) and r is the distance between the source mass and the mass in free-fall. Therefore, the sole coefficient of g, the gravitational constant, is proportional to $1/k$. The gravitational constant is conventionally fixed so that $k = 1$.

In summary, the Equivalence Principle allows any (freely falling) coordinate system in an arbitrary gravitational field to be a coordinate system in absence of gravitation.

(If the gravitational field is not uniform, an infinitesimal region, in which the gravitational field can be considered as uniform, can be considered as the coordinate system. This coordinate system referred to as a local Lorenz system of coordinates (e.g. [2]).) In this coordinate system, the laws of motion take the same form as in an unaccelerated inertial frame of reference in absence of gravitation.

This principle has to be tested experimentally. It is said that Galilei did the famous leaning tower experiment at Pisa to check whether different materials freely fall at the same rate. Newton compared the periods of pendulums for various materials (gold, silver, lead, glass, sand, common salt, wood, water and wheat) and checked this principle to $\Delta k < 10^{-3}$ [3], where Δk is the difference in k between materials. Currently, it is verified to the 10^{-13} level (see Section 2.2). This principle is now generally referred to as the Weak Equivalence Principle (e.g. [4, 5]) or as the Universality of Free Fall, to distinguish it from the Strong Equivalence Principle, which will be described in the following section.

1.1.2 Strong Equivalence Principle

The Weak Equivalence Principle only refers to the uniformity of the laws of motion, as discussed in the previous section. In 1911, Einstein introduced a principle which extends the validity of the Weak Equivalence Principle to all the laws of nature [6]. That is to say, in a freely falling coordinate system, all the laws of nature take the same form as in an unaccelerated Lorentz coordinate system in the absence of gravitation. This extended Weak Equivalence Principle is called Strong Equivalence Principle (e.g.

[4]).

According to the Strong Equivalence Principle, light in a freely falling coordinate system S', for example, behaves in the same way as in an unaccelerated Lorentz coordinate system (e.g. [2]). In S', the square of the distance which light travelled from x'^{μ} to $x'^{\mu} + \Delta x'^{\mu}$ can be expressed as:

$$\Delta s^2 = -(c\Delta t')^2 + (\Delta x')^2 = \eta_{\mu\nu}\Delta x'^{\mu}\Delta x'^{\nu} \tag{1.7}$$

where c is the velocity of light. For an observer in an inertial coordinate system S, S' is freely falling. Therefore, the observer in the system S sees that the light path is distorted. If there is a general relation between S and S' as follows:

$$x'^{\mu} = f^{\mu}(x) \tag{1.8}$$

then $\Delta x'^{\mu}$ can be written as:

$$\Delta x'^{\mu} = \frac{\partial f^{\mu}(x)}{\partial x^{\nu}}\Delta x^{\nu}. \tag{1.9}$$

Substituting Equation (1.9) in Equation (1.7), Δs^2 can be expressed with space-time of S, x^{μ}, as:

$$\Delta s^2 = \eta_{\rho\sigma}\frac{\partial f^{\mu}}{\partial x^{\rho}}\frac{\partial f^{\nu}}{\partial x^{\sigma}}\Delta x^{\mu}\Delta x^{\nu} = g_{\mu\nu}(x)\Delta x^{\mu}\Delta x^{\nu}, \tag{1.10}$$

where

$$g_{\mu\nu}(x) \equiv \eta_{\rho\sigma}\frac{\partial f^{\mu}}{\partial x^{\rho}}\frac{\partial f^{\nu}}{\partial x^{\sigma}}. \tag{1.11}$$

By comparing Equations (1.7) and (1.10), it can be seen that $g_{\mu\nu}$ is a quantity which expresses the deflection of the light path. $g_{\mu\nu}$ is called the Einstein's gravitational

potential in Einstein's General Relativity [2]. However, $g_{\mu\nu}$ is mathematically called a metric tensor, which determines the characteristic of geometry. Geometry in which the definition of distance is given by Equation (1.10) is called Riemannian Geometry (e.g. [2]).

Therefore, it can be said that the Strong Equivalence Principle introduced an unprecedented idea; it gives the metric tensor of geometry the meanings of gravitational potential. In other words, the Strong Equivalence Principle implies that the physical substances, which produce gravitational fields, determine the geometry of space-time. He presented his gravitational theory of General Relativity in 1916, postulating the Strong Equivalence Principle as the basis of the theory [7].

In summary, it can be said that the Weak Equivalence Principle is the basis of both of Newtonian mechanics and Einstein's General Relativity. These theories are fundamental in modern physics and should be tested as precisely as possible. One of the most sensitive tests is to search for the violation of the Universality of Free Fall. This experimental search will be discussed in Chapter 2.

The Strong Equivalence Principle is also called Einstein Equivalence Principle (e.g. [5]). The Strong Equivalence Principle is sometimes distinguished to two versions [4]: a "very strong" principle, which applies to all phenomena, and a "medium-strong" principle, which applies to all phenomena except gravitation itself. Nordtvedt noted that the very strong principle can be tested by using the Lunar Laser Ranging[2] (LLR)

[2]As we will describe in Section 2.3.2, measurements of geodesic precession by the Lunar Laser Ranging experiment put one of the most stringent limits on a composition dependent force.

to compare the acceleration of the Earth and the Moon, whose gravitational self-energy is not negligible, toward the Sun [8, 9]. The ambiguity in the results of LLR, due to the composition difference between the Earth and Moon, is removed by laboratory experiments [10].

1.2 Predictions of new interactions

1.2.1 Introduction

It is now believed that there are four fundamental interactions in nature, namely, strong, weak, electromagnetic and gravitational interactions. All the interactions are believed to be based on a gauge theory. We will briefly describe what a gauge theory is below (see for example [11] for more detailed description).

For electromagnetism, local gauge transformation is individual rotation of phase (by an angle $\alpha(x)$) of a wave function of a charged particle (e.g. [11]):

$$\psi_j(x) \rightarrow e^{i\alpha(x)Q_j}\psi_j(x) \tag{1.12}$$

With the introduction of a vector field ($\mathbf{A}_\mu$) into the theory of electromagnetism, any interactions of wave functions are invariant under the local gauge transformation because of the conservation of charge, Q. The requirement that interactions are invariant under local gauge transformations is called gauge principle.

The gauge principle generally requires introduction of fields like $\mathbf{A}_\mu$ in electromagnetism. The fields are called gauge fields. Quantized gauge fields are called gauge bosons. In the gauge theory, gauge bosons mediate forces between the conserved quan-

Interactions	Gauge bosons	Gauge groups
Strong interaction	gluons	SU(3)
Weak interaction	W-bosons, Z-bosons	SU(2)
Electromagnetic interaction	Photons	U(1)
Gravitational interaction	Gravitons	

Table 1.1: Interactions based on the gauge principle. Weak interaction and electromagnetic interaction are unified as electroweak interaction based on SU(2)×U(1) gauge group. Gauge theory of the three interactions except gravitational interaction, based on SU(3)×SU(2)×U(1) gauge group, is called the Standard Model of Particle Physics (see Section 1.3).

tities (electric charges in electromagnetism). Because of the required invariance under local gauge transformation, gauge bosons are generally massless particles. In the electroweak field theory, spontaneously broken symmetry in Higgs mechanism gives mass to gauge bosons.

Each interaction has different gauge transformations and gauge bosons. The local gauge transformation (1.12) is called U(1) group in mathematics. Other interactions are summarised in Table 1.1.

As we will describe in more detail in Section 1.2.4, properties of a force (repulsive/attractive, spin dependence and effective range) are determined by the property of gauge bosons (spin, parity and mass). We will briefly describe the relation between the mass of gauge bosons and the effective range of a force below.

Heisenberg's uncertainty relation is given as follows (e.g. [11]):

$$\Delta E \times \Delta t \geq \hbar, \tag{1.13}$$

where $\hbar = h/2\pi$ (h is Planck's constant). ΔE and Δt are uncertainties in energy and time, respectively. Virtual particles can exist within the allowed uncertainty. Gauge

bosons are considered to exist as virtual particles and mediate forces. The range that they can travel is the range over which the force is effective. By assuming that the velocity of virtual particle (mass, m) may be approximately the speed of light, c, and $\Delta E \approx mc^2$, the distance they can travel is $c\Delta t \approx \hbar/mc$. This range, λ, is called Compton wavelength (e.g. [11]). When m is zero, the virtual particle can travel an infinite distance. For example, photons are massless particles and mediate electromagnetic forces, whose effective range is infinite. We will describe in Section 1.2.3 that forces mediated by massless gauge bosons obey an inverse-square law, while gauge bosons with mass result in Yukawa-type interactions.

In summary, in gauge theory, properties of a force are determined by properties of the gauge bosons that are necessarily introduced by the gauge principle. The charge of the force is the conserved quantity. The strength of the force has to be determined by experiments.

We will first see below a force, suggested by Lee and Yang, which is mediated by massless vector particles. Then we will see more general case when the mediating particles have a mass.

1.2.2 Lee and Yang's work

As described above, conservation of electric charge is related to gauge invariance. In 1955, Lee and Yang [12] suggested that the conservation of baryon number should also be related to some gauge invariance. If it is so, there should be a gauge boson which corresponds to the gauge invariance, in analogy with photons that correspond to the

U(1) gauge invariance in electromagnetism. The gauge boson would mediate a new force between baryons.

In this assumption, the potential energy between point baryon charges, B_1 and B_2, can be written as:

$$V(r) = \beta \frac{B_1 B_2}{r} \tag{1.14}$$

from analogue of electromagnetism:

$$V(r) = \alpha \frac{Q_1 Q_2}{r} \tag{1.15}$$

where $\alpha = e^2/4\pi\epsilon_0$ and $\beta = f_B^2/4\pi\epsilon_0$. e and f_B are the fundamental electric charge and fundamental charge of the new force, respectively. Q_1 and Q_2 are point electric charges.

The bosons that mediate the suggested force would be vector massless particles (like photons). The baryon number differs for each chemical element. Therefore, this suggested force would violate the Universality of Free Fall[3].

1.2.3 Yukawa-potential type

We can proceed with Lee and Yang's idea; instead of the massless vector boson, we can think of more general cases; bosons with natural parities ($J^P = 0^+$, 1^-, 2^+) and with mass m_5. For these generalized bosons, the Schrödinger equation becomes the Klein-Gordon equation, which is obtained by quantization of the relativistic relation

[3]We will see in Section 2.1 that the differential acceleration of two test masses made of different chemical compositions is expected to be proportional to the difference in the putative charge, such as the baryon number.

between energy (E) and momentum (p): $E^2 = p^2c^2 + m_5^2c^4$. The static Klein-Gordon equation is as follows:

$$\left\{\nabla^2 + \left(\frac{m_5 c}{\hbar}\right)^2\right\}\phi = 0 \tag{1.16}$$

When $m_5 = 0$, the Klein-Gordon equation reduces to the Laplace equation:

$$\nabla^2\phi = 0 \tag{1.17}$$

The potential appearing in the electromagnetism (Equation (1.15)) and Lee and Yang's work (Equation (1.14)) is proportional to $1/r$. This type of potential is a solution of the Laplace equation.

A solution to the Klein-Gordon equation is proportional to $e^{-r/\lambda}/r$, which is called Yukawa-potential. Then the potential energy between some point charges Q_{5i} and Q_{5j} would be:

$$V(r) = \pm\beta_5 \frac{Q_{5i}Q_{5j}}{r} e^{-r/\lambda} \tag{1.18}$$

where $\beta_5 = f_5^2/4\pi\epsilon_0$, and f_5 is a fundamental charge. The subscript of 5 is used as this type of putative forces is often referred to as fifth force.

More generally, Q_5 may be written as a linear combination of baryon number (B), Lepton number (L) and Isospin (I_z) [13]:

$$Q_{5i} = B\cos\theta_5 + I_z \sin\theta_5 \tag{1.19}$$

or

$$Q_{5i} = B\cos\bar{\theta}_5 + L\sin\bar{\theta}_5, \tag{1.20}$$

where $-90^\circ < \bar{\theta}_5 \leq 90^\circ$. Most experiments to search for new forces uses electrically neutral bulk matter because the presence of charges would introduce spurious effects from electromagnetic forces. For neutral matter, $L = Z$, where Z is proton number. Therefore:

$$B = Z + N \tag{1.21}$$

$$I_z = N - Z = B - 2L, \tag{1.22}$$

where N indicates neutron number.

To sum up, the new interactions have been introduced naturally basing on the conservation of baryon number and the gauge principle. The potential of Equation (1.18) is the typical form of new putative interactions suggested by various theories. We will review these theories in Section 1.3.

If a new force exists, the total potential energy of (neutral) point masses of m_i and m_j may be written as a sum of Newtonian potential energy and Equation (1.18) (e.g. Equation (2.1.6) in [13]):

$$V(r) = -G_\infty \frac{m_i m_j}{r} \pm \beta_5 \frac{Q_{5i} Q_{5j}}{r} e^{-r/\lambda} \tag{1.23}$$

$$= -G_\infty \frac{m_i m_j}{r} \left(1 - \frac{\pm\beta_5 Q_{5i} Q_{5j}}{G_\infty m_i m_j} e^{-r/\lambda}\right) \tag{1.24}$$

$$= -G_\infty \frac{m_i m_j}{r} \left(1 + \alpha_{ij} e^{-r/\lambda}\right) \tag{1.25}$$

where

$$\alpha_{ij} \equiv -\frac{Q_{5i}}{\mu_i}\frac{Q_{5j}}{\mu_j}\xi \equiv -q_{5i} q_{5j} \xi \tag{1.26}$$

$$\xi \equiv \frac{\pm\beta_5}{G_\infty m_H^2} \tag{1.27}$$

Where $m_H \equiv m({}_1H^1) = (1.00782519 \pm 0.00000008)u$ and, therefore, $m_i = \mu_i m_H$. G_∞ is the value of the Newtonian constant when $r/\lambda \gg 1$ (see Equation (1.29)).

Differentiating Equation (1.25), $\vec{F} = -\vec{\nabla}V(r)$, we obtain the force:

$$\vec{F} = G(r)\frac{m_i m_j}{r^2}\vec{r}, \tag{1.28}$$

where

$$G(r) \equiv G_\infty \left\{1 + \left(1 + \frac{r}{\lambda}\right)\alpha_{ij}e^{-r/\lambda}\right\}. \tag{1.29}$$

1.2.4 Characters of putative forces

The following aspects may characterize a force:

1. whether it is a repulsive or attractive force,
2. what the range (λ) of the force is,
3. whether it depends on spin or not,
4. how strong the interaction is,
5. what kind of charges (Q) is associated with the force.

The first aspect is determined by the spin of the mediated bosons. Whether a force is attractive or repulsive, namely the sign in Equation (1.18) or in ξ (Equation (1.27)), depends on the spin of mediated bosons [14]. The force mediated by bosons whose spin is even (0,2, ...) is attractive, while the force mediated by bosons with odd-spin (1,3, ...) can be either repulsive or attractive, depending on the signs of charges, and takes

either a positive or negative sign. For positive charges, the sign in Equation (1.18) or in ξ (Equation (1.27)) is negative for forces mediated by even-spin bosons and positive for forces mediated by odd-spin bosons. Gravitation is an example of attractive forces as it is mediated by spin-2 particle (graviton). Electromagnetic forces, mediated by a spin-1 particle (photon), are attractive or repulsive, depending on the charges.

As we have discussed previously, the second aspect is determined by the mass of mediating bosons. It can be examined by experiments with different distances between source mass and test masses. The third aspect is determined by whether the mediating bosons have a natural parity or unnatural parity. Natural parities ($J^P = 0^+, 1^-, 2^+$) generally results in spin-independent forces, while unnatural parities ($J^P = 0^-, 1^+, 2^-$) generally results in spin-dependent forces. The fourth aspect corresponds to ξ. $\xi - \lambda$ plots show the constraints on a new force, as we see below. The fifth aspect would be investigated by operating experiments with various combinations of test mass materials and source mass materials. These aspects are summarized in Table 1.2.

The properties of a force are generally predicted theoretically but these predictions depend strongly on the models and/or unknown parameters. Therefore, they must be determined by experiments. It is clear that a single experiment would never be enough to constrain the theoretical models with various combinations of the above factors.

We limit our discussion to spin-independent forces. Searches for spin-dependent interactions can be found, for example in [13]. Also, detailed descriptions on developments of an instrument to search for a spin-mass coupling new force can be found in

Parameters	Characters
Spin of mediating bosons	Repulsive/attractive
Mass (m_5)	Effective range
Parity	spin dependency
Coupling constant (ξ)	strength
Charge (Q)	Charge

Table 1.2: Parameters that determine the characters of forces are summarized. The first three parameters are characteristics of the mediating bosons.

[15, 16].

1.3 Predictions from theories towards unification of four forces

One of the dreams of many physicists is to build an ultimate theory that unifies all the interactions satisfactory. The Standard Model of Particle Physics is accepted as a fundamental theory for three of these interactions, excluding the gravitational interaction (see Table 1.1). The Standard Model is consistent with experimental data, but it is not satisfactory as a ultimate theory. First of all, it is rather complicated. For example, the three interactions are all based on a gauge theory, but there are three different gauge coupling constants corresponding to each interaction. The biggest problem of the Standard Model is that it does not include gravitational interaction, whose existence is well known. New theories beyond the Standard Model have been suggested towards the unification of the four interaction (e.g. [11, 17]):

Grand Unified Theory (GUT) unifies the three interactions into a single gauge group and introduces a large mass scale of approximately 10^{15} GeV. However, GUT

does not explain the origin of the large ratio of the large mass scale and the mass scale of weak interaction, about 100 GeV. A solution to this problem is introduction of supersymmetry, which is a new symmetry between fermions and bosons.

Supergravity is a theory that has supersymmetry and could include gravity. In Supergravity, a fermion with spin 3/2 appears as a partner of graviton (spin 2). This spin 3/2 fermion has a boson partner with spin 1, and this boson with spin 1 has a fermion partner with spin 1/2. This spin 1/2 fermion has a spin 0 partner. The bosons (spin 1 and spin 0) introduced here could mediate new forces related to gravitational force. The bosons with spin 1 and spin 0 are called graviphotons and graviscalars, respectively (e.g. [18]).

As we have seen before, the mass of the mediated particle decides the effective range of the force and the spin of the mediated particle decides the sign of the forces. Supersymmetric particles are expected to have the same mass as their partner. Experimental searches for supersymmetric particles using high energy accelerators have been done [e.g. [19]]. However, none of supersymmetric particles has been observed so far. Therefore, it seems that supersymmetry is broken and masses of the supersymmetric particles are too heavy to be created with the current accelerators. Therefore, the range of the force would be finite and the force would be the Yukawa-potential type. Force mediated by graviphotons could be repulsive or attractive like electromagnetism, while force mediated by graviscalars would be attractive like gravity.

It is said that the most promising theory that unifies gravitation with the other

forces is superstring theory. This theory also generally introduces new bosons called dilatons and moduli. These bosons could also mediate new forces that could violate the Universality of Free Fall.

Because there are many unknown factors in those theories, no precise estimation of the predicted violations of the Universality of Free Fall have been made. However, Damour and Polyakov's work [20] (see Table 1.3), motivated by string theory, presents a level of a violation of the Universality of Free Fall as $10^{-14} \sim 10^{-23}$. The mediating particles are massless, therefore, the range of the new force would be infinite.

As we will briefly describe below, Damour and Polyakov's proposal suggests that the putative charge would be baryon numbers ($B = N + Z$), isospins ($I_Z = N - Z$, neutron excess) and electrostatic energy density of a nucleus ($E = Z(Z-1)(N+Z)^{-1/3}$):

According to [20], the coupling constant of dilatons (ϕ) to mass A (m_A) is given as (Equation (3.6) in [20]):

$$\alpha_A(\phi) = \frac{\partial \ln m_A(\phi)}{\partial \phi} \tag{1.30}$$

while m_A(atom) can be given as follows:

$$m_A = Zm_p + Nm_n + Zm_e + E_s + E_c \tag{1.31}$$

where m_p, m_n and m_e denote masses of proton, neutron and election. E_s and E_c denote the strong-interaction contribution to the binding energy of the nucleus and the Coulomb interaction energy of the nucleus. This equation may be written:

$$m_A = a_0 + a_1 B + a_2 I_Z + a_3 E \tag{1.32}$$

where a_0, a_1, a_2 and a_3 are constants. The difference in the rate of free-fall (Δa) between two test masses made of different chemical compositions (A and B) in a gravitational field (g) would be proportional to the difference in the coupling constant, namely $\Delta a/g \propto \alpha_A - \alpha_B$. Therefore, the expected violation of the Universality of Free Fall depends on B, I_Z and E.

Damour and Polyakov's proposal is interesting as a motivation for experimental searches of violations of the Universality of Free Fall; the current limits are approximately 10^{-13} and the space-based experiment, STEP (Satellite Test of the Equivalence Principle), is aiming at a sensitivity of 10^{-18}.

In short, those theories towards the unification of four forces typically predict new bosons, which would mediate new forces. The proposed charges for the new forces depend on models. Table 1.3 lists some of the theories that predict violations of the Universality of Free Fall. The putative charges predicted by the theories can be classified into three categories: the baryon number, isospin (neutron excess) and electrostatic energy density (Table 1.3).

1.4 Summary

It can be said that the equivalence of two quantities (inertial mass and gravitational mass) that apparently relates to the completely different forces is a surprising coincidence. However, the basis of modern physics, namely the Newtonian mechanics and Einstein's general relativity, is based on the Weak Equivalence Principle. Therefore,

Motivated by	Bosons (Spin)	Mass	Charge	References
Conservation of baryon charge	vector bosons (1)	No	B	[12]
Supersymmetry	U-bosons (1)	Yes (very light)	B, I_z	[21]
String theory	dilatons (0)	Yes	Ordinary matter	[22, 23]
	dilatons (0)	No	B, I_z, E	[20]
	moduli (0)	Yes (millimeter range)	Ordinary matter	[24]

Table 1.3: A list of proposals of (spin-independent) new forces. Yes and No in the third column indicate that the mediating particles have/do not have a mass, respectively. B, I_z and E are the baryon number, the isospin and a contribution proportional to electrostatic energy of a nucleus.

experimental approaches are necessary to test the Weak Equivalence Principle as precisely as possible.

Another motivation for the experimental tests of the Weak Equivalence Principle is due to the predictions of violations of the Weak Equivalence Principle from theories towards the unification of four forces. Those theories typically predict Yukawa-potential type interactions. The predicted putative charge falls into three kinds: baryon number, isospin and electrostatic energy density. Results from sensitive experiments, such as STEP, could guide a way towards the unified theory.

Chapter 2

Experimental tests of the Weak Equivalence Principle

In this chapter, experimental tests of the Weak Equivalence Principle will be presented. After an introduction in Section 2.1, we will review the current limits that result from experimental searches. In Section 2.4, space-based future experiments will be described. We will focus on the description of STEP, which aims at the most sensitive test of the Weak Equivalence Principle.

2.1 Introduction

Experimental Search for a Yukawa-potential type new force can be viewed from two aspects [25]:

- Search for deviation from the inverse-square law and
- Search for violations of the Universality of Free Fall.

The former is to search for the variation of G(r) (Equation (1.29)) and often referred to as a search for composition independent effects. This type of search also can study

composition dependent effects if test masses of different chemical compositions are used.

The latter aims at measuring the differential acceleration between test masses of different compositions. It is often referred to as a search for composition dependent effects. The differential acceleration of a new force of Yukawa potential-type between point objects j and j' can be written as follows from Equation (1.28):

$$\frac{\Delta\vec{a}_{j-j'}}{a_g} = -\xi q_{5i}\Delta q_{5j-j'} e^{-r/\lambda}\left(1+\frac{r}{\lambda}\right)\vec{r}, \tag{2.1}$$

where

$$\Delta q_{5j-j'} = q_{5j} - q_{5j'} \tag{2.2}$$

$$a_g = G_\infty \frac{m_i}{r^2} \tag{2.3}$$

Here $\overrightarrow{r}$ is a unit vector and a_g is the gravitational acceleration toward the point source mass i. $\frac{\Delta\vec{a}_{j-j'}}{a_g}$ is equal to the difference in k (see Equation (1.4)) between the objects, Δk. The experimental results often expressed in terms of a parameter $\eta(j,j')$ [26]:

$$\eta(j,j') = \frac{(m_P/m_I)_j - (m_P/m_I)_{j'}}{\frac{1}{2}\{(m_P/m_I)_j + (m_P/m_I)_{j'}\}} \tag{2.4}$$

It should be noted that η is equivalent to Δk by taking k as 1.

According to Equation (2.1), the sensitivity of searches for composition dependent effects may depend on the following factors:

1. attracting field of the source, a_g,

2. charge of the source mass, q_{5i}, and

3. difference in charge between test masses, $\Delta q_{5j-j'}$.

Increasing these values, one obtains a better sensitivity.

As we have seen in Section 1.2.2, a force mediated by massless bosons could not produce deviations from the inverse-square law. Therefore, the search for composition independent effects is insensitive to forces mediated by massless bosons. However, the search for composition dependent effects is inevitably insensitive to the case when $q_{5j} = q_{5j'}$. Therefore, these two searches are complementary to each other as searches for new Yukawa-potential type forces. However, we will focus on the searches for the composition dependent forces, which can be viewed as the search for the violation of the Universality of Free Fall.

2.2 Current limits

Figures 2.1 and 2.2 (adapted from [13]) are the current limits on the Yukawa-type new forces mediated by bosons with an odd-spin[1]. Values of (ξ, λ) above the curves are excluded with a confidence level of 2σ. The values are estimated from Equation (2.1), basing data from the most sensitive experiments. Where ξ_B and ξ_I denote the coupling constants to baryon number, when $\theta_5 = 0°$ in Equation (1.19), and to isospin, when $\theta_5 = 90°$ in Equation (1.19), respectively (see also Equation (1.27)).

Almost all the ranges of λ are constrained by torsion balance experiments (referred to as Eötvös in Figures 2.1 and 2.2) done by the Seattle group [27, 28, 29, 30], except

[1]Limits on Yukawa-type new forces mediated by bosons with an even-spin can be obtained by estimating $-\xi_B$ and $-\xi_I$ from experimental results, and are presented, for example, in [27, 28].

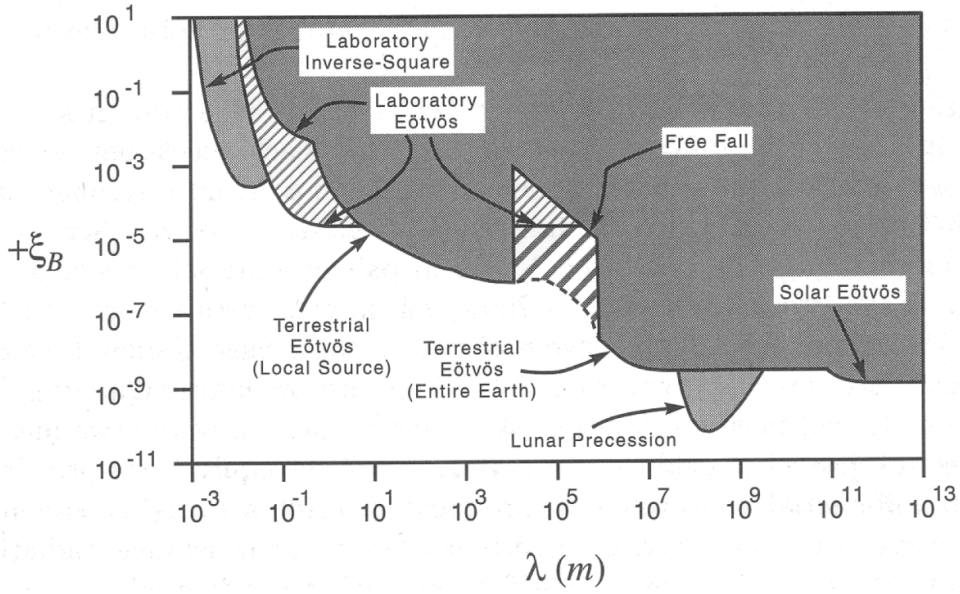

Figure 2.1: Limits on Yukawa-type new forces, plotted assuming that the charge is the baryon number (see the text). Eötvös refers to torsion balance experiments.

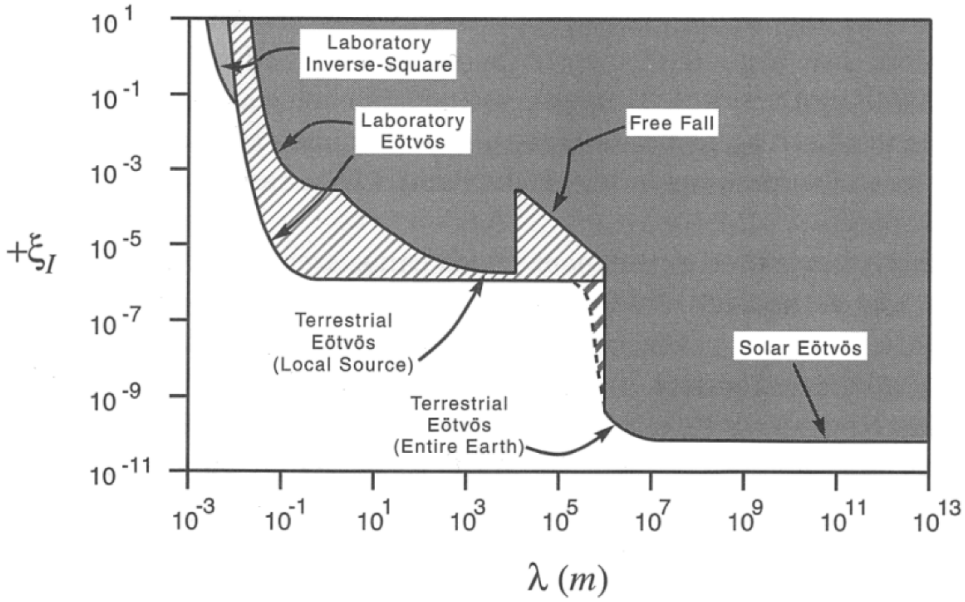

Figure 2.2: Limits on Yukawa-type new forces, plotted assuming that the charge is isospin (see the text). Eötvös refers to torsion balance experiments.

the short range ($\lambda \sim 10^{-1}m$ for ξ_B and $\lambda \sim 10^{-2}m$ for ξ_I) limited by inverse-square law experiments [31] and the range from approximately 10^8 to 10^9 m for ξ_B, where the Lunar Precession data are sensitive. The regions denoted by Solar Eötvös were obtained by a solar torsion-balance experiment by Braginskii and Panov [32].

The wide-diagonally shaded regions denote the region where the constrains are uncertain. The uncertainty is due to the difficulty in modelling Earth's mass distribution with sufficient accuracy on length scales where Earth cannot be approximated as a fluid in equilibrium [27]. The diagonally shaded regions show the constrains by recent data from the Seattle group [30, 28].

We summarise these three sensitive experiments (torsion balance experiments, inverse-square laboratory experiments and lunar laser ranging experiments) in the following sections. Reviews of various experiments can be found, for example, in [13, 25].

The plotted results in those figures can be converted into the limit on η (Equation (2.4)). For example, the best limit, obtained from the result of the lunar precession, is the level of 10^{-13} in η as $B/\mu \sim 1$ and $\Delta B/\mu \sim 10^{-3}$ (see Table 2.1 in [13] for the first 92 elements in the periodic table or Table 1.3 in this thesis for some of the elements).

The constraints on ξ_B are less sensitive than for ξ_I by a factor of approximately 10 over most of the range. This is because of the magnitude of relative charge for non-Newtonian force in Equation (2.1):

$$|\Delta(B/\mu)|(B/\mu)_{source} \sim \frac{1}{10}|\Delta(I_z/\mu)|(I_z/\mu)_{source} \tag{2.5}$$

2.3 Sensitive methods at various ranges

2.3.1 Torsion balance experiments

The region denoted by Solar Eötvös, Terrestrial Eötvös (Entire Earth), Terrestrial Eötvös (Local Source) and Laboratory Eötvös in Figures 2.1 and 2.2 were limited by torsion balance experiments using the Sun [32], the Earth [27], local terrestrial source (hill) [27] and laboratory source (U^{238}) [30, 28] as the source.

As shown in Equation (2.1), for a given q_{5i} and $\Delta q_{5j-j'}$ and a fixed ξ, the maximum sensitivity is achieved when $r < \lambda$. This tendency is shown Figures 2.1 and 2.2.

We will briefly review the experiments in this section.

Detection principle

Torsion balances are used to compare the horizontal accelerations ($a_\perp$) of two test masses. To describe the detection principle of the torsion balance, we consider an ideal simplified torsion balance, as shown in Figure 2.3, which has one arm (with length s) that is holding two test masses (m) made of different chemical compositions (A and B) at both ends. The total force on a test mass would have contributions from gravity, centrifugal force and possibly from a new force. If one of the test mass is attracted more than the other toward a putative charge, and if the net force on each test mass does not lie in the same plane, the torsion balance experiences a torque:

$$T_5 = \frac{1}{2} sm\Delta a_\perp = \frac{1}{2} sm\Delta a \sin\delta \tag{2.6}$$

where δ is an angle between the average new force and the sum of all the forces (gravity, centrifugal force and the new force). As we will describe later, the experiments should be designed so that the net force does not lie in the same plane and $\sin\delta$ is maximised.

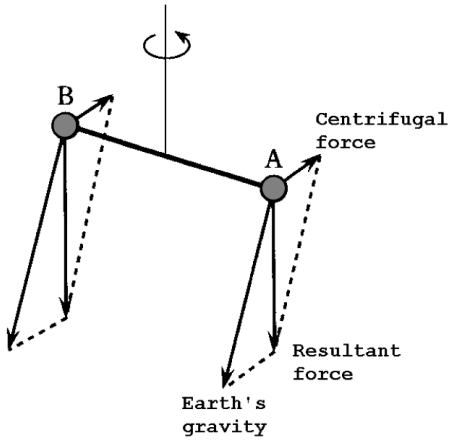

Figure 2.3: A schematic view of a torsion balance (This figure was quoted from [33].)

Disturbances

Torsion-balance experiments are generally limited by systematic error (e.g. [25]). In general, experiments are designed as symmetrical as possible to have less susceptibility to sources of systematic error. For a sensitive experiment, significant efforts are required to reduce systematic errors associated with gravity gradients, thermal variations and mechanical disturbances.

To reduce gravity gradient effects, the leading-order gravitational moments of test masses are generally minimized and also the ambient source mass gravitational moments are reduced by means of a compensating mass distribution (see [27, 30] for Seattle group's procedures).

Temperature variations are typically minimized by controlling the thermal environment of the apparatus and by maximising the symmetry of the experiment.

Mechanical disturbances of the suspension fiber can easily produce systematic errors. For example, a tilt of the fiber attachment changes the orientation of the pendulum and can cause a rotation on the torsion fiber that mimics a new force. Nonlinearities in the fiber can convert vertical seismic noise into the torsional period, though the peak of seismic noise is at larger frequencies than the typical torsion period.

Solar source experiments

Modulation of a signal can eliminate spurious disturbance. As the Sun has approximately one-day period, the expected signal of a solar source experiment has the same period of approximately 24 hours. However, this is not a very convenient period as many sources of disturbances, such as temperature and vertical seismic motion, vary with the same cycle.

The solar experiments loose sensitivity for range of less than 1 AU.

Terrestrial and laboratory source experiments

To explore ranges shorter than 1 AU, terrestrial sources and laboratory sources are used.

For a range which is larger than the radius of the Earth, a new force and the gravitational force would be aligned. However, because of the Earth's rotation (angular

velocity ω), the torsion fiber tilts from those forces by (e.g. [25]):

$$\delta \simeq \frac{\omega^2 R_E}{2g_E} \sin 2\Theta \tag{2.7}$$

where Θ, R_E and g_E are the latitude of the experiment, the radius of the Earth and the Earth's gravity, respectively. The maximum sensitivity of terrestrial source experiments is obtained at a latitude of 45°. In addition, in the configuration with the torsion arm aligned along the North-South direction, the effect of a new force towards the Earth would not produce a torque because their resultant forces are in the same plane. Theretofore, East-West configuration is preferred for terrestrial source experiments.

The Seattle group continuously rotates their torsion balance by means of a high-precision turntable [27]; they can choose a convenient period of signal modulation, which is considerably shorter than the 24 hours period of the Sun. This eliminates the disturbances with daily cycle that was involved in the solar source experiments. Even though the rotation of the apparatus principally introduces noise, they achieved a sensitivity comparable to the solar source experiment (see Figures 2.1 and 2.2) that does not involve the active rotation of the apparatus, using the entire Earth as the source. This high sensitivity is because of the advantage of the choice of the period and because of the larger signal by using the Earth as the source (roughly three times as large as the case of the solar source experiment).

To obtain a sensitivity to terrestrial local source, experiments are set at the edge of a cliff or on the slop of a hill. The Seattle group's experiments are located on a hillside at the University of Washington [27]. To investigate shorter ranges, they rotate their

laboratory source mass of U^{238} around the stationary balance [30, 28].

Seattle group's experiments, using the entire Earth [27], the local terrestrial source [27] and the laboratory source [30, 28], put the constraints on the regions shown in Figures 2.1 and 2.2.

Summary

Modern torsion balance experiments have a sensitivity of better than 10^{-12} in $\Delta a/a_g$ (η). The sensitivity is limited by thermal noise and seismic noise. The thermal noise could be reduced by a factor of ten or so by operating a cryogenic torsion balance [34]. There are no good solutions to the problem of the seismic noise. A large fraction of the vertical seismic motion originates from human activity. Only one solution to avoid this noise source may be to set the experiment at a quiet place, such as a remote region or in space. There are Indian torsion balance experiments that are operated in an underground laboratory at a remote village in South India [35]. The Indian group aims at a sensitivity of 10^{-14} in $\Delta a/a_g$ (η). Also, several space-based experiments have been proposed as future experiments. We will discuss them in Section 2.4.

2.3.2 Lunar laser ranging

Lunar Laser Ranging Experiment (e.g. [36]) is to measure the distance between the Earth and the Moon by laser ranging. Laser retro-reflectors were placed on the Moon by astronauts of Apollo (11, 14, 15) and French-Russian collaboration during 1967 to 1973.

General relativity predicts geodetic precession of the lunar orbit with respect to inertial frame of the solar system by 19 ms of arc per year [36]. Search for deviation from this predicted value of precession can investigate a new force.

For a putative Yukawa-type new force of the form given in Equation (1.25), the deviation from the lunar precession angle can be given by the rate of precession per orbit [37]:

$$\delta\varphi \cong +\pi\alpha_{ij}(a/\lambda)^2 e^{-a/\lambda} \tag{2.8}$$

where a is the semi-major axis of the Moon from the Earth. One can see the effective sensitivity of this method from Equation (2.8). For a fixed value of α_{ij}, the maximum sensitivity is achieved at $a/\lambda = 2$. As shown in Figure 2.1, the sensitivity vanishes for both of $a/\lambda \to \infty$ and $a/\lambda \to 0$.

A result of the Lunar Laser Ranging experiment shows a deviation of $-0.3 \pm 0.9\%$ from the predicted value of 19 ms of arc per year [26]. This uncertainty corresponds to $\delta\varphi \sim 2$ nrad/orbit. With this value and Equation (2.8), we obtain the exclusion plot in Figure 2.1.

2.3.3 Inverse-square law experiments

For the shortest range in Figures 2.1 and 2.2, the inverse-square law experiments establish the most stringent limits. This type of experiment belongs to the category of search for composition-independent effects, which examines the variation of the Newton's constant with r ($G(r)$), as described in the Section 2.1.

In order to check the variation of $G(r)$, measurements of G at two different positions of r_1 and r_2 are compared. Torques, τ_1 and τ_2, experienced on a torsion balance toward a source mass at position r_1 and r_2, respectively, are measured. Uncertainties in each of the torques are attributed to the mass measurements of the proof masses and the source mass, the determination of the distances (r_1 and r_2) and the Newton's gravitational constant. In order to eliminate the uncertainty due to the absolute accuracy of the mass measurements and the value of the Newton's constant, the ratio of the torque difference is generally considered:

$$\Delta = \frac{\tau_2 - \tau_1}{\tau_1}. \tag{2.9}$$

In order to conduct the short-range experiments, various experimental geometries have been investigated. One of these ideas is to use a principle that a test body inside the gravitational field of a spherical shell or a cylindrical shell with an infinite length ideally does not feel the force from the shell as it is moved. This is the case when the inverse-square law is valid. If one measures a torque of the test body inside the source mass of cylindrical shell, it would be attributed to a new non-inverse square force.

Hoskins et al. [31] carried out experiments with this type of experimental geometry (cylindrical shell with inner radius 3 cm) and put the most sensitive limit at the range of a few centimeters as shown in Figures 2.1 and 2.2.

2.4 Space-based Experiments

As we have seen in Section 2.2, Seattle group's experiments give the most stringent limits on the Yukawa-type new force at almost all over the range of λ in Figures 2.1 and 2.2. Thermal effects, gravity gradients and seismic noise basically limit the sensitivity of the experiments. Although the ground-based experiment can be improved, the seismic effects may ultimately limit the improvement of sensitivity. Space-based experiments have been planned as future experiments to explore the violation of the Universality of Free Fall. They are designed to improve the current sensitivity by, at least, one order of magnitude. As described in Section 1.3, Damour and Polyakov suggested that a superstring theory would violate the Universality of Free Fall at the level of 10^{-14} to 10^{-23} [20], which could be explored by some of the suggested space-based experiments.

We will summarise some space-based experiments in this section. We will emphasize the STEP project as the main body of this thesis discusses disturbances associated with test masses for STEP. We will compare other space-based projects with STEP.

2.4.1 STEP

Overview

STEP (e.g. [38]) is an international project and was originally proposed by Stanford University nearly 30 years ago [39]. STEP aims at testing the Universality of Free Fall to the level of 10^{-18}.

As shown in Figure 2.4, pairs of test masses made of different chemical compositions are to be put in a low Earth orbit (approximately 500 km above the surface of

the Earth). The test masses are to be in free fall in the Earth's gravity field. The difference in acceleration between the test masses is to be detected using a SQUID (Superconducting Quantum Interference Device) position detector (we will describe these details later.).

As shown in Figure 2.4, test masses are belted cylindrical shapes (see below for details on the shape design). The test masses can move relative to each other along the axial axis, z. Figure 2.4 shows the case when the inner test mass is attracted by the Earth with a larger acceleration than the outer test mass. The expected signature of a violation of the Universality of Free Fall is a modulation of once per Earth orbit (see Figure 2.5). However, in the normal mode of operation, the spacecraft is to be spun about an axis perpendicular to the orbital plane to shift the expected signal frequency from the orbital frequency (the spin frequency is to be in the range from -3 to +3 revolutions per orbit to prevent it from disturbances due to destabilization). Many disturbances potentially have the orbital frequency, such the electric charging from South Atlantic Anomaly and gravitational couplings of the test masses to the Earth's higher moments when the spacecraft is in an elliptical orbit.

A schematic view of the STEP cryostat and the test mass housing are shown in Figures 2.6 and 2.7, respectively. The cylindrical dewar vessel (length 1.3 m, diameter 1.0 m, Figure 2.6) can contain 180 l of liquid helium. The experiment operates throughout the mission at 1.8 K. The liquid helium holds about seven months. Detailed descriptions of the spacecraft can be found, for example, in [40, 41].

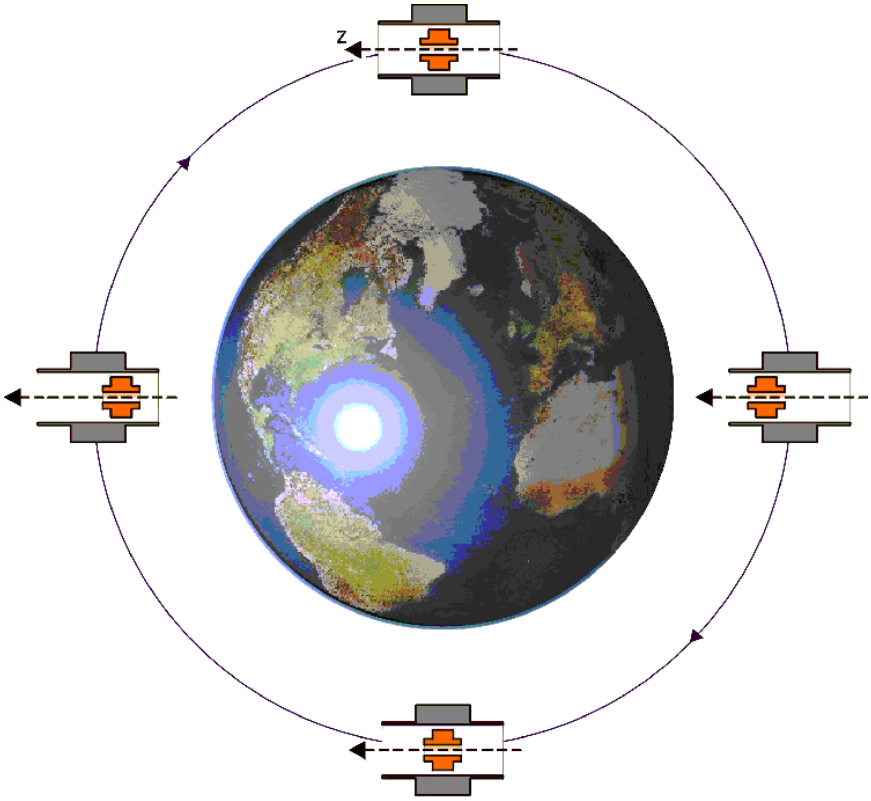

Figure 2.4: A schematic view of STEP (adapted from [42], not drawn to scale). A pair of test masses (belted cylinders) is in a low Earth orbit. The test masses can only move relative to each other along the z-axis. If the inner test mass is attracted by the Earth with a larger acceleration than the outer test mass, the relative motion would be schematically as shown in this figure. (Spin of the spacecraft (see text) is omitted in this figure for simplicity.)

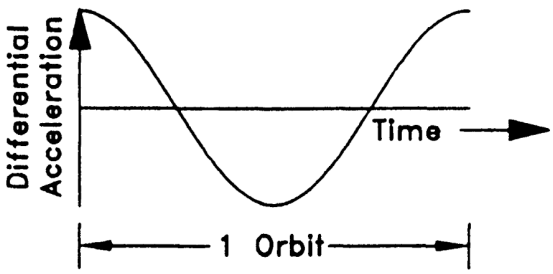

Figure 2.5: An expected signal of a violation of the Weak Equivalence Principle (quoted from [43]) when the spacecraft was not spun.

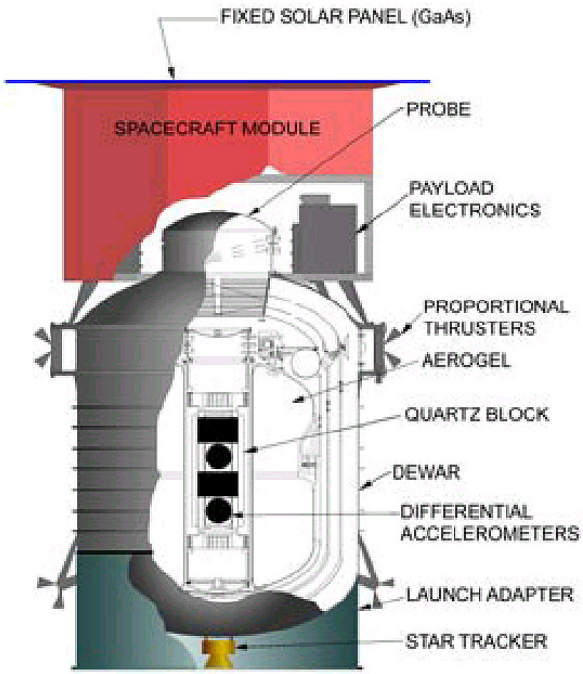

Figure 2.6: A schematic view of the STEP cryostat (quoted from [41]). The height and the diameter of the dewar are roughly 1.3 m and 1 m, respectively (p. 5 in [40]).

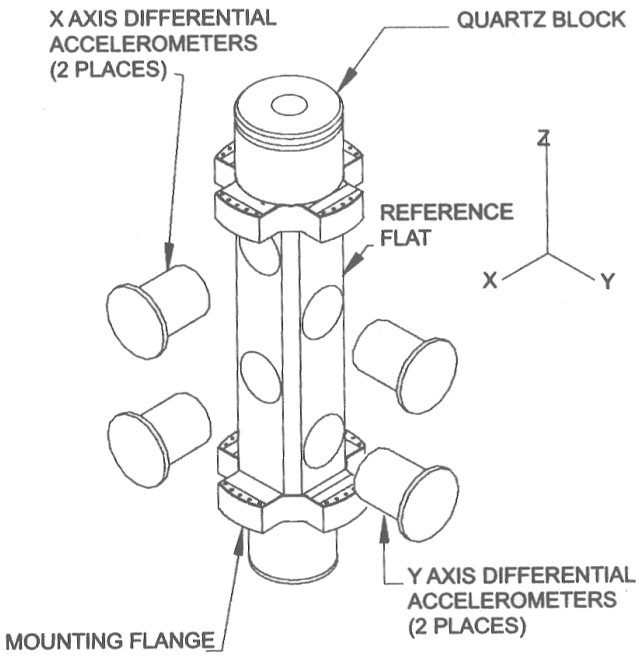

Figure 2.7: A schematic view of the STEP test-mass housing (quoted from [41]). The length of each differential accelerometer is approximately 165 mm.

Advantages in STEP

The STEP spacecraft orbits around the Earth at approximately 500 km altitude; the full value of the Earth's gravity field at that altitude ($\simeq$ 8.4 m/s^2) is to be balanced against the spacecraft's orbital acceleration. The Earth's gravity is larger than the Sun's gravity by a factor of roughly 1000. Also, the Earth's gravity is larger than the maximum centrifugal force due to the Earth's rotation (at a latitude 45°) by a factor of approximately 700. The increase of the attracting field (a_g in Equation (2.1)) improves on the sensitivity of the ground-based experiments by approximately 3 orders of magnitude for the range larger than roughly 7000 km (radius of the Earth plus the latitude of the orbit ($\sim$ 500 km)).

Another improvement of approximately 2 orders of magnitude comes from the reduction of the seismic noise in space. In space, the disturbance due to the seismic noise of the ground-based experiments is replaced by noise due to atmospheric drag. This disturbance is reduced by the drag compensation system which maintains the test masses in an almost absolute inertial reference.

These two advantages, taken together, could produce an improvement on the limits established by the ground-based experiments by approximately 5 orders of magnitude. According to the error analysis by Worden et al. [44], the STEP sensitivity would be limited by the SQUID noise.

The experiment chamber is cooled to cryogenic temperatures (1.8 K). This cryogenic operation has several advantages [38]:

- The SQUID magnetometer, a very stable and sensitive position detector, is available (it can detect a relative acceleration of 10^{-15}m/s^2 in 1 sec.).

- Superconductors can be used to shield the Earth's magnetic field (a thin lead bag around the experiment chamber, together with niobium coating of test masses (see the description of detection system below), attenuates the Earth's magnetic field by a factor of at least 10^{10}.).

- Gas pressure can be reduced because all gases except helium are frozen at 1.8 K (pressures less than 10^{-10} torr are feasible).

- Radiation pressure disturbances due to temperature gradients can be reduced.

Detection system

The differential acceleration, between the test masses is monitored by a SQUID position detector.

A single accelerometer is composed of a test mass placed between two superconducting pickup coils (spiral pancake coils of inductances L_1 and L_2 in Figure 2.8) wired in series, with a persistent supercurrent flowing around the circuit. The test mass is coated by a thin film of superconducting niobium. The coating is used to constrain the test mass's movement on a magnetic bearing that is aligned with the axial direction (z-direction) of the test mass. Motion of the test mass towards one of the pickup coils will change the magnetic flux of the pickup coils and a current will flow to the third coil (L_3) in parallel with the two pickup coils. This signal current is proportional to

the first order to the displacement and is to be detected by the SQUID magnetometer.

By employing two such detection circuits in an accelerometer, the differences in displacement between test masses can be measured (see Figure 2.9). STEP uses this principle for the measurement of differential acceleration between a pair of test masses. The common mode signal of two test masses will be detected by SQUIDs and be used for the drag-free control.

Test mass design

The Equivalence Principle only holds for test masses in an uniform gravitational field. However, according to gravitational theories, uniform gravitational fields do not exist (see Section 3.1). Gravity gradients in general disturb tests of the Universality of Free Fall. Possible origins of gravity-gradients effects in STEP are in the spacecraft and from the Earth's gravity.

The Earth's gravity-gradients effects are to be eliminated by adjustment of the centres of mass of the test masses. The effects are at twice per signal frequency. The adjustment is to be done until the gradient signal is nulled. This adjustment eliminates not only the Earth's gravity gradient effect, but also most of the gravity gradients due to the spacecraft.

With this adjustment and the drag-free control system, the test masses are controlled to be in free fall in the same gravitational field.

Even though they are put in the same gravitational field by the adjustment of their centres of mass, they would not fall at the same rate unless they have the same

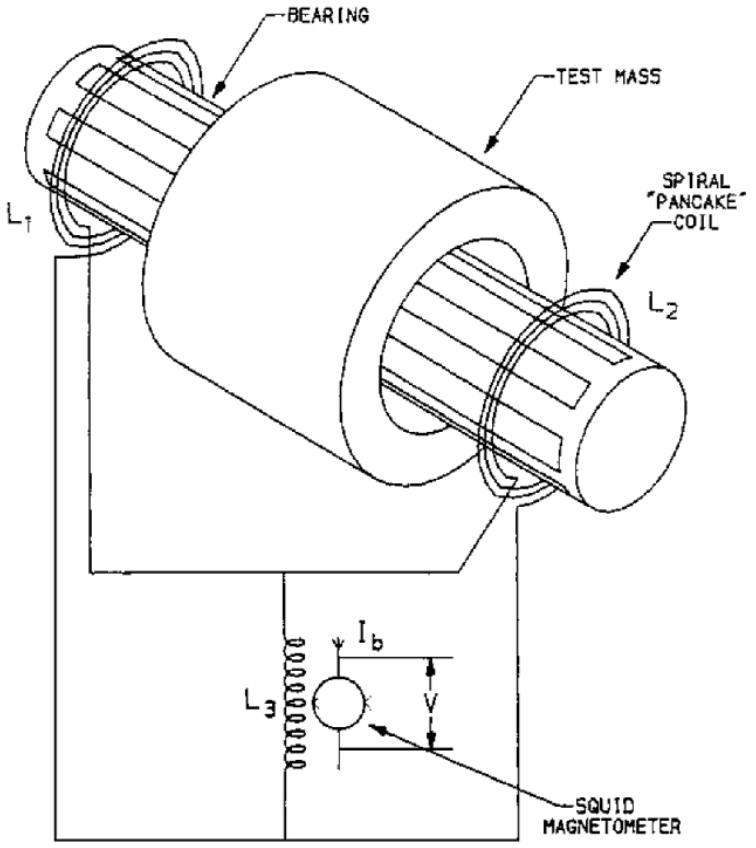

Figure 2.8: Concept of an accelerometer (quoted from [43])

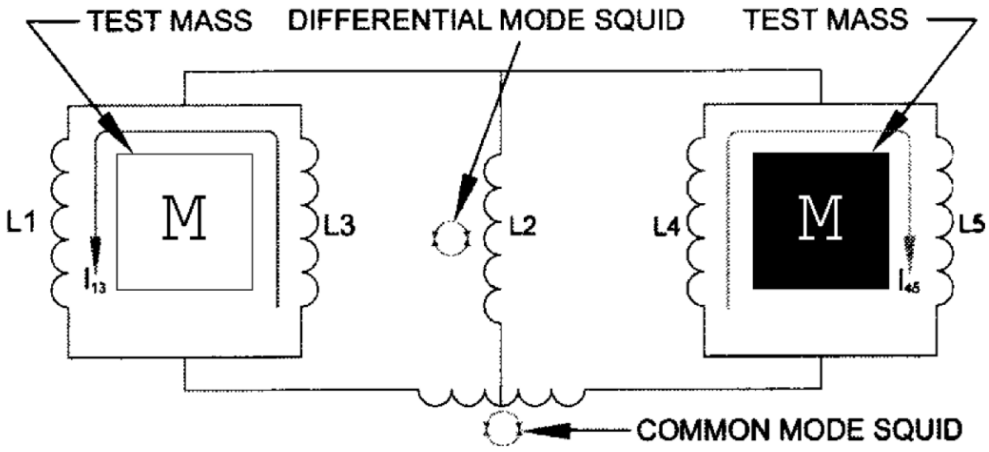

Figure 2.9: Measurement of differential acceleration (quoted from [41])

gravitational higher moments. Their gravitational higher moments would couple to the higher moments of surrounding materials around the test masses (see analysis in Section 3.2).

The possible disturbances at the signal frequency are due to the helium tide (see below) and thermal deformation of the spacecraft (by thermal radiation from the Earth) (p. 59 in [40]).

Helium bubbles are evaporated from the liquid helium in the dewar (see Figure 2.6 for the configuration of the cryostat). The tidal bulge on the body of the liquid helium would give disturbances at twice per signal frequency. As the surface tension of the body of liquid helium tries to minimize its surface area, helium bubbles, formed in the dewar, may pump up and form a single large bubble. This bubble would follow the tidal force and rotate around the test masses at the expected signal frequency. This motion of helium could produce a spurious acceleration at the same frequency as the signal of the violation of the Weak Equivalence Principle by coupling differently to higher moments of each test mass in a pair (see Chapter 3 for further analysis).

To eliminate those disturbances two approaches have been done for STEP: one is to reduce the higher moments of the test masses and the other is to suppress the helium motion.

The shapes of STEP test masses are optimized to reduce the gravitational higher moments and simultaneously to have the same gravitational higher moments [45], by taking the advantage of the belted cylindrical shapes suggested by Speake [46] (see

Section 3.5). Other factors that could produce gravitational higher moments are density inhomogeneities and thermal distortion of test masses. These aspects will be discussed in this thesis.

To suppress the helium motion, a two-chamber dewar (the inner and outer radii of approximately 25 cm and 50 cm, respectively) (Section 3.4.2 in [43]) and aerogel confinement techniques [47, 48] (see Figure 2.6 for the configuration of the cryostat) are under study. The inner and outer chambers of the dewar are designed to have the same volume. This dewar is designed so that the inner chamber is kept full with liquid helium during the first half of the mission and empty during the second half; there would be no helium motion. Aerogel filled in the inner chamber is expected to suppress the helium motion.

Disturbance due to the thermal deformations of the spacecraft would be less than that due to the helium motion because the spacecraft is farther away from the test masses. However, the spacecraft should be designed so that thermal deformations are minimised as source.

Test mass selection

Materials selection is a compromise between the technical requirements and theoretical motivation. Technical requirements includes machinability, coatability (with superconducting thin film), dimensional stability, density homogeneities and low magnetic susceptibility.

As discussed in Section 2.1, a signal of a violation of the Weak Equivalence Principle

is expected to be proportional to the difference in charge to a new force between test masses ($\Delta q_{5j-j'}$ in Equation (2.1)). One would like to chose test masses so that the difference in charge is as large as possible to achieve a better sensitivity. Three kinds of putative charges, baryon numbers ($B = N+Z$), isospins ($I_z = N-Z$) and electrostatic energy density of a nucleus ($E = Z(Z-1)(N+Z)^{-1/3}$), have been proposed by the theories to be related to new forces (see Sections 1.2 and 1.3, and Table 1.3).

Figure 2.10 shows the relative differences[2] in the baryon number, isospin and electrostatic energy density all relative to atomic mass (μ) for various elements that could possibly be used as STEP test masses. Table 2.1 lists the absolute values.

As one can see in Figure 2.10, beryllium is expected to be a key element to obtain high sensitivities; no elements have similar levels of those putative charges with beryllium.

From a theoretical point of view, Be, Pt and Si (or elements close to Si in the plot, such as Mg and Al) are suggested as test mass materials to distinguish between the three putative charges [49]. However, the choice of materials is still under discussion because of lack in the information on the technical aspects. Technical aspects have to be experimentally checked for all candidate materials. At the moment, pairs of Be-Pt, Be-Nb and Nb-Pt are the strongest candidate as STEP test masses. The main reason why niobium was chosen is its superconductivity; there is no need to coat with a niobium thin film. A prototype outer beryllium test mass and inner niobium test

[2]The relative differences are given by $(q_i - q_{\rm Be})/(q_{\rm Bi} - q_{\rm Be})$, where q_i is a charge (B/μ, I_Z/μ or E/μ) of an element i.

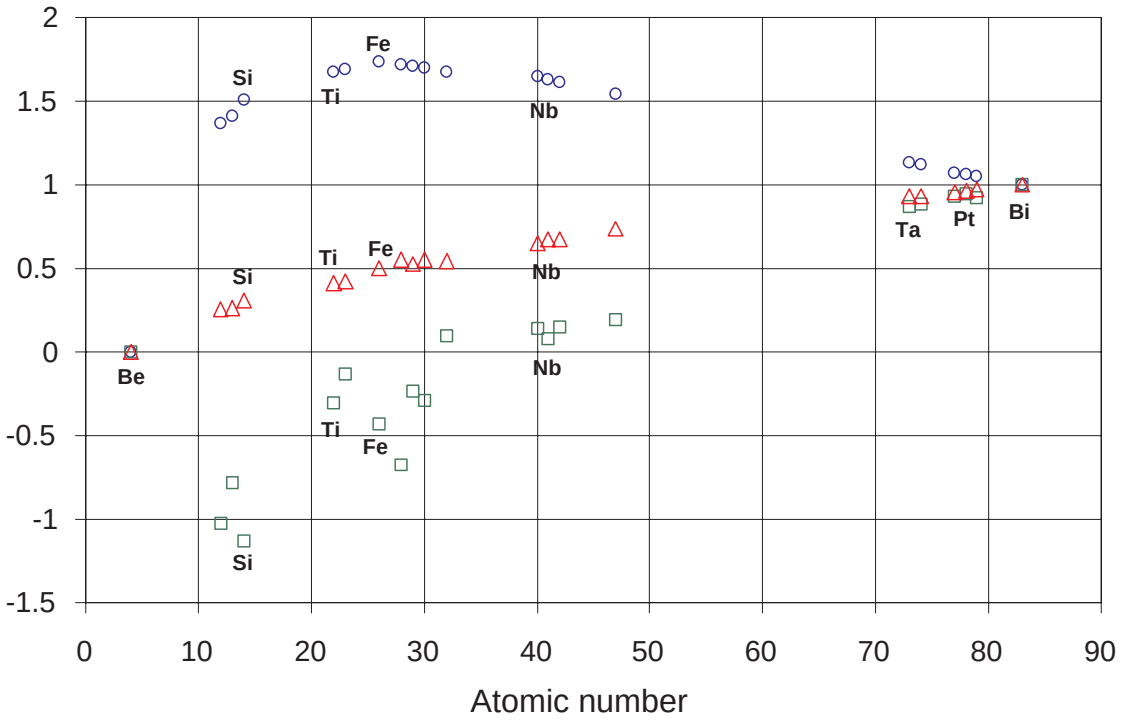

Figure 2.10: Relative differences in B/μ (circle), I_z/μ (square) and E/μ (triangle) between elements considered as STEP test mass materials, plotted as a function of atomic number. The absolute values are listed in Table 2.1.

Element	Z	B	μ	B/μ	I_z/μ	E/μ
Beryllium	4	9	8.942211	1.006462	0.11183	0.64514
Magnesium	12	24.3247	24.120799	1.008453	0.01346	1.88871
Aluminium	13	27	26.772043	1.008515	0.03735	1.94232
Silicon	14	28.1088	27.867542	1.008657	0.00390	2.14796
Titanium	22	47.9305	47.507173	1.008911	0.08273	2.67719
Vanadium	23	50.9976	50.546037	1.008934	0.09887	2.69948
Iron	26	55.9121	55.413691	1.008994	0.07060	3.06757
Nickel	28	58.771192	58.249142	1.008962	0.04757	3.33819
Copper	29	63.616522	63.052162	1.008951	0.08908	3.22601
Zinc	30	65.4595	64.879191	1.008944	0.08414	3.32728
Germanium	32	72.708329	72.066646	1.008904	0.12084	3.29799
Zirconium	40	91.3185	90.515443	1.008872	0.12504	3.82721
Niobium	41	93	92.185017	1.008841	0.11933	3.92665
Molybdenum	42	95.9838	95.145077	1.008815	0.12595	3.95288
Silver	47	107.96341	107.030804	1.008713	0.13046	4.24217
Tantalum	73	180.999877	179.542926	1.008115	0.19494	5.17521
Tungsten	74	183.890595	182.414337	1.008093	0.19675	5.20766
Iridium	77	192.254	190.723678	1.008024	0.20057	5.31628
Platinum	78	195.116262	193.565933	1.008009	0.20208	5.34965
Gold	79	197	195.437208	1.007996	0.19955	5.41867
Bismuth	83	209	207.35778	1.007920	0.20737	5.53082

Table 2.1: Average values of B/μ, I_z/μ and E/μ (over the stable isotopes) for the elements plotted in Figure 2.10, calculated using the values of Z, B and μ in [13]. The values of B are weighed by stable isotropic abundances.

mass were fabricated as a trial (platinum test masses were not made because of the cost.). Technical aspects of density inhomogeneities and thermal dimensional stability of the materials for the prototype test masses will be examined in this thesis.

In practice, Pt/Ir alloy is considered to be used as test masses, instead of pure platinum. Pure platinum is probably too soft. Also, HIPed (Hot Isostatically Pressed) beryllium is considered to be used because crystalline beryllium has anisotropic thermal expansion (see Section 6.1.1).

2.4.2 Microscope

Microscope is a space-based French project of ONERA (Office National d'Etudes et de Recherches) [50, 51]. This experiment can be viewed as a simple version of STEP. The objective is to test the violation of the Universality of Free Fall at the level of 10^{-15}. This is the only one project that is funded and will be launched in 2004. The main differences between STEP and Microscope are: it operates at room temperature; test masses are straight hollow cylindrical shapes (without belts); two electrostatic accelerometers to be used; one pair of test masses made of 90Pt-10Rh (weight percent) alloy and Ti (0.5 kg - 0.4 kg) and another pair made of the same material, 90Pt-10Rh alloy (0.5 kg - 1.7 kg), are to be used [52].

2.4.3 Galileo Galilei

Galileo Galilei (GG) [53, 54] is an Italian project and funded by ASI (Agenzia Spaziale Italiana). It is designed to achieve a sensitivity of 10^{-17} at room temperature. It

consists only one electrostatic accelerometer to simplify the apparatus. It uses hollow cylindrical test masses that are nested within each other (see Figure 2.11). It modulates the signal of the violation of the Universality of Free Fall, by spinning the spacecraft at 2 Hz along the test masses' axial axis which is directed parallel to the Earth orbit of the spacecraft. This modulation frequency is higher than STEP and Microscope by approximately three orders of magnitude. This high frequent signal of GG reduces low frequency noise. Two pairs of capacitance plates between the test masses measure any relative displacements of the centre of mass of the test masses.

Another feature of this experiment is the room temperature operation. The reason why GG could achieve the sensitivity compatible to the cryogenic experiment of STEP is that they use roughly 100 times heavier test masses of 10 kg. Thermal noise is proportional to $(T/M)^{1/2}$, where T is temperature and M is mass. Therefore, one can reduce thermal noise by increasing the weight of the test masses.

According to [54], residual air drag is the limiting factor of the GG experiment.

2.5 Summary

We have seen the current limits on the violation of the Weak Equivalence Principle and reviewed sensitive experiments and future experiments. The current limits are established by the torsion balance experiments of the Seattle group over the most of the range. To improve the current limits, space-based experiments have been suggested. Some of them would have the sensitivity to test the prediction motivated by string

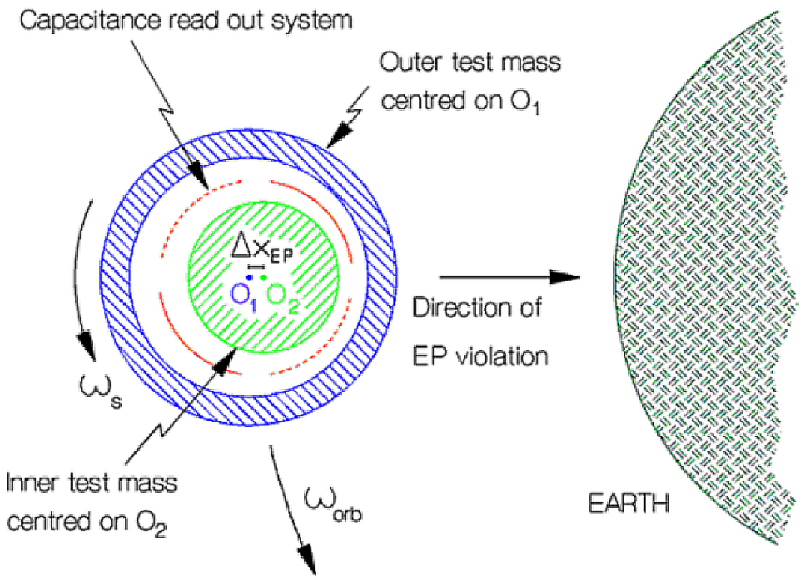

Figure 2.11: A schematic view of GG (quoted from [54], not drawn to scale). A cross section of the coaxial test cylinders and capacitance sensors in the plane perpendicular to the spin axis. The entire spacecraft spins at an angular velocity of ω_s while orbiting around the Earth at an angular velocity of ω_{orb}. This figure shows the case when the inner test mass is attracted by the Earth more than the outer test mass because of a violation of the Universality of Free Fall. The signal is modulated at ω_s as the capacitance sensors that detect the relative motion between test masses spin at ω_s with the spacecraft.

theory. However, the space-based experiments are sensitive only for ranges longer than approximately the Earth's radius, while the laboratory experiments are sensitive to short ranges and long ranges; simple models suggest that elimination of short range forces also eliminates long range forces. Single experiment is never enough to test the principle because of the variety of the possible new forces that violate the principle.

Chapter 3

STEP test masses

In this chapter, we review the design of STEP test masses and discuss the allowable magnitude of gravitational higher moments of the test masses. After an introduction, we describe the acceleration of a test mass in a gravitational field in Section 3.2 and differential acceleration of a pair of test masses in Section 3.3. We describe quantities that express the magnitude of the gravitational multipole moments in Section 3.4. We describe the current shape design of STEP test masses in Section 3.5 and discuss the allowable magnitudes of the gravitational multipole moments in Section 3.7. Metrological issues, density inhomogeneities and thermal distortion, follow in Sections 3.6.1 and 3.6.2.

3.1 Introduction

Newton's inverse square law can be written as a Poisson equation:

$$\nabla^2\Phi = 4\pi G\rho \tag{3.1}$$

where Φ is a gravitational potential due to an active mass with density ρ. G is the gravitational constant. This equation is replaced by the Einstein equation in Einstein's General Relativity (e.g. [2]):

$$G^{\mu\nu} = \frac{8\pi G}{c^4} T^{\mu\nu} \tag{3.2}$$

The above equations show that the gravity gradients (the left-hand sides of those equations) are determined by mass/energy densities (the right-hand sides). From these equations, one can see that if there is mass/energy, there are gravity gradients produced by them; there are no uniform gravitational fields.

In Section 1.1, we have seen that the Equivalence Principle allows any free falling coordinate system in arbitrary gravitational field to be a coordinate system in absence of gravitation. However, the cancellation of the gravitational force and the fictitious force occurs only at one point. In reality, as we have seen above, there are no uniform gravitational fields. Therefore, to test the Universality of Free Fall to a high precision, it is essential to design the test masses to be gravitational monopole (point mass)-like as much as possible. As we will see later in this chapter, the STEP test masses are designed to be virtually a monopole-like. Other possible causes to make the test masses differ from the gravitationally monopole-like behavior are imperfections in test masses, such as density inhomogeneities and thermal distortion. We will discuss these metrological aspects in this thesis.

3.2 Acceleration of a test mass

Previously during the process of optimizing the geometry of the test masses, axial symmetry was assumed [38, 55]. However, as shown in Section 5.4, our measurements of the density inhomogeneities in real materials indicate that a more general approach is required. The acceleration of a non-axially symmetric test mass will be described in this section. We will first review the form of gravitational potential.

3.2.1 Gravitational potential

The gravitational potential energy of a point test mass (M_{TM}) in a gravitational field due to a point source mass (M_{SM}) can be written as follows:

$$V(r) = -G\frac{M_{TM}M_{SM}}{r} \tag{3.3}$$

where r is the distance between the test mass at $\mathbf{x}'$ and the source mass at $\mathbf{x}$, $|\mathbf{x}-\mathbf{x}'|$.

When M_{TM} and M_{SM} are not point masses, they are derived by integrating the density distribution, $\rho(\mathbf{x}')$ for the test mass and $\rho(\mathbf{x})$ for the source mass, over the volume, v, for the test mass or V for the volume of the source mass:

$$M_{TM} = \int_v \rho(\mathbf{x}')d^3x', \tag{3.4}$$

$$M_{SM} = \int_V \rho(\mathbf{x})d^3x. \tag{3.5}$$

Therefore, Equation (3.3) becomes:

$$V(\mathbf{x}) = -G\int_v\int_V \frac{\rho(\mathbf{x}')\rho(\mathbf{x})}{|\mathbf{x}-\mathbf{x}'|}d^3x'd^3x. \tag{3.6}$$

$1/|\mathbf{x}-\mathbf{x}'|$ can be expanded as follows (Equation (3.70) in [56]):

$$\frac{1}{|\mathbf{x}-\mathbf{x}'|} = 4\pi \sum_{l=0}^{\infty} \sum_{m=-l}^{l} \frac{1}{2l+1} \frac{r'^l}{r^{l+1}} Y^*{}_{lm}(\theta', \phi')\, Y_{lm}(\theta, \phi). \tag{3.7}$$

By substituting Equation (3.7) into Equation (3.6), we obtain:

$$V(\mathbf{x}) = -4\pi G \sum_{l=0}^{\infty} \sum_{m=-l}^{l} \frac{1}{2l+1} q_{lm} Q_{lm} \tag{3.8}$$

where

$$q_{lm} = \int_v \rho(\mathbf{x}') r'^l Y^*_{lm}(\theta', \phi') d^3x', \tag{3.9}$$

$$Q_{lm} = \int_V \rho(\mathbf{x}) r^{-(l+1)} Y_{lm}(\theta, \phi) d^3x. \tag{3.10}$$

q_{lm} and Q_{lm} represent the mass distribution of the test mass and the source mass, respectively. q_{lm} are called gravitational multipole moments.

3.2.2 Shift of multipole moments

As described in Section 2.4.1, the STEP test masses are to be belted-cylindrical shapes and their movement is restricted to the axial direction. The force between the test mass and the source mass in the axial direction can be obtained by shifting the multipole moments of the test mass along the axis by dZ' [57].

The leading order term of the shifted multipole moments ($\widetilde{q}_{LM}$) can be obtained as follows using the formula by D' Urso and Adelberger, Equation (10) in [58]:

$$\widetilde{q}_{LM} = \sqrt{\frac{4\pi(2L+1)!}{3!(2l+1)!}} dZ' Y^*_{10}(0) C(1, 0, l, m, L, m) q_{lm}, \tag{3.11}$$

where $L = l + l' (= l+1)$. Because of the small displacement l' is taken as 1. Also, because the displacement is along the axial direction, the selection rule of $M = m$ [58]

is applied in Equation (3.11). The spherical harmonics [56] and the Clebsh-Gordan coefficient [59] in Equation (3.11) are given as follows, respectively:

$$Y_{10}^{*}(0) = \sqrt{\frac{3}{4\pi}}, \tag{3.12}$$

$$C(1,0,l,m,L,m) = \sqrt{\frac{(l-m+1)(l+m+1)}{(2l+1)(l+1)}}. \tag{3.13}$$

By substituting Equation (3.12) and (3.13) into Equation (3.11) we obtain:

$$\widetilde{q}_{LM} = \sqrt{\frac{(2L+1)(L-m)(L+m)}{2L-1}} dZ' q_{L-1,m}. \tag{3.14}$$

With Equation (3.14), the force ($= -dV/dZ'$) is given as follows:

$$F_Z = 4\pi G \sum_{L=1}^{\infty} \sum_{m=-L}^{L} \sqrt{\frac{(L-m)(L+m)}{(2L-1)(2L+1)}} q_{L-1,m} Q_{Lm}. \tag{3.15}$$

By dividing Equation (3.15) by the mass of the test mass (M_{TM}), the acceleration of the test mass is given as follows[1]:

$$a_Z = \frac{4\pi G}{M_{TM}} \sum_{L=1}^{\infty} \sum_{m=-L}^{L} \sqrt{\frac{(L-m)(L+m)}{(2L-1)(2L+1)}} q_{L-1,m} Q_{Lm}. \tag{3.16}$$

By replacing $L-1$ by l,

$$a_Z = \frac{4\pi G}{M_{TM}} \sum_{l=0}^{\infty} \sum_{m=-l}^{l} \sqrt{\frac{(l+1-m)(l+1+m)}{(2l+1)(2l+3)}} q_{lm} Q_{l+1,m} \tag{3.17}$$

This equation agrees with [61], which was obtained by direct differentiation of the gravitational potential. A detailed description of the differentiation is given in Appendix A of [62].

[1]Equation (3.16) was firstly obtained by Speake in September 2000 [60] and described in [57].

3.3 Differential acceleration of test masses

The differential acceleration between a pair of test masses can be obtained by taking their difference in acceleration (3.16):

$$\Delta a_Z = {a_Z}^{outer} - {a_Z}^{inner}, \tag{3.18}$$

where *outer* and *inner* stand for outer test mass and inner test mass, respectively.

When the test masses are in the same gravitational field ($Q_{l+1,m}$), the differential acceleration is given as follows:

$$\Delta a_Z = 4\pi G \sum_{l=0}^{\infty} \sum_{m=-l}^{l} \sqrt{\frac{(l+1-m)(l+1+m)}{(2l+1)(2l+3)}} \left(\frac{\Delta q_{lm}}{M_{TM}}\right) Q_{l+1,m} \tag{3.19}$$

where

$$\frac{\Delta q_{lm}}{M_{TM}} = \frac{q_{lm}^{outer}}{M_{TM}^{outer}} - \frac{q_{lm}^{inner}}{M_{TM}^{inner}}. \tag{3.20}$$

As described in Section 2.4.1, the differential acceleration of STEP test masses is to be measured with a sensitivity of 10^{-18}g ($g = 8.4\text{m/s}^2$ at the orbital latitude of 500 km). Thus, the differential acceleration noise levels should be kept, say, to below 10^{-18}m/s^2.

STEP test masses are not designed to monitor the noise sources; it is impossible to perfectly discriminate real signals due to the violations of the Weak Equivalence Principle and false signals due to the noise source masses. Therefore, it is essential for the STEP experiment to have the accelerometer sufficiently insensitive to the noise source masses. As mentioned in Section 2.4.1, this requirement may be achieved by either or both of the following approaches; one is eliminating the higher multipole

moments of the test masses (or the difference in higher multipole moments between the test masses) and the other is reducing the noise source ($Q_{l+1,m}$). The STEP team used the former approaches in the process of the design of the test masses (see Section 3.5 for the detailed design). In addition, higher multipole moments produced by the imperfections in test masses, due to for example density inhomogeneities and thermal distortion, have to be examined. These metrological aspects will be dealt in this thesis. The latter approach is under study; the new aerogel confinement techniques [47, 48] are being developed to exclude helium motions as a source of disturbance (see Section 2.4.1).

3.4 Gravitational multipole moments of test masses

In this section, we review three quantities that express the magnitude of gravitational multipole moments of the STEP test masses. The first two quantities, the differential gravitational quadrupole moments and the gravitational susceptibility [55], have been conventionally used by the STEP team.

3.4.1 Differential gravitational quadrupole moments

The shape design of STEP test masses has been done by assuming that their density is homogeneous [38, 45, 55]. When test masses are homogeneous, Equation (3.16) becomes simpler; all the odd terms ($l = 1, 3, 5, ...$) of the multipole moments (Equation (3.9)) vanish because of the integrals over the cylindrical (belted) test masses with mirror-symmetry about a mid-plane perpendicular to the z-axis [55]; because of the

axial symmetry, $m = 0$.

The multipole moments of a simple cylinder (with radius R, half-length L and density ρ) can be written as follows:

$$q_{lm} = \rho \int_v r'^l Y_{lm}^*(\theta', \phi') d^3x' \tag{3.21}$$

$$= M_{TM} k_{lm} \tag{3.22}$$

where

$$k_{lm} = \frac{1}{2\pi R^2 L} \int_v r'^l Y_{lm}^*(\theta', \phi') d^3x'. \tag{3.23}$$

k_{lm} are determined by the geometry of the test mass. Equation (3.20) becomes:

$$\frac{\Delta q_{lm}}{M_{TM}} = k_{lm}^{outer} - k_{lm}^{inner} = \Delta k_{lm} \tag{3.24}$$

The first terms ($l = 0$) of multipole moments (Equation (3.9)) generally corresponds to a point or spherical test mass[2]:

$$q_{00} = \int_v \rho(\mathbf{x}') Y_{00} d^3x' \tag{3.25}$$

$$= \frac{1}{\sqrt{4\pi}} M_{TM} \tag{3.26}$$

Therefore, the first terms in the multipole moment expansion to contribute to the differential acceleration are quadrupole moments (q_{20}) by assuming the axial symmetry of the test mass. The contribution from the quadrupole moments is most likely to be

[2]Spherical objects are not the only one gravitational monopole. A non-spherical gravitational monopole shape was discussed for STEP by Connes et al [63]. An asymmetric monopole was discussed by Barrett [64].

dominant; when l gets larger the contribution become smaller as $Q_{l+1,m} \propto 1/r^{l+2}$ (see Equation (3.10)). The differential acceleration (Equation (3.19)) is given as follows:

$$\Delta a_{Z,20} = \frac{12\pi G}{\sqrt{35}}(\Delta k_{20})Q_{30}, \tag{3.27}$$

As mentioned before, the differential acceleration should be kept below the required noise level, S_Z ($= 10^{-18}\mathrm{m/s^2}$):

$$|\Delta a_Z| < S_Z. \tag{3.28}$$

With this requirement and Equation (3.27), the difference in quadrupole moments should satisfy the following condition:

$$\left|\frac{\Delta q_{20}}{M_{TM}}\right| < \frac{\kappa \cdot S_Z}{Q_{30}} \tag{3.29}$$

where κ is a coefficient:

$$\kappa = \frac{\sqrt{35}}{12\pi G} = 2.4 \times 10^9. \tag{3.30}$$

The moment of inertia of the cylinder can be given as follows:

$$I_Z = \rho \int_{-L}^{L} \int_0^{2\pi} \int_0^R \sigma'^2 \cdot \sigma' d\sigma' d\phi' dz' \tag{3.31}$$

$$= \frac{M_{TM} \cdot R^2}{2} \tag{3.32}$$

where $M_{TM} = 2\pi R^2 L \rho$.

By dividing Equation (3.29) by the moment of inertia of test masses (Equation (3.32)), which has the same dimensions as quadrupole moments, we obtain:

$$\left|\frac{\Delta q_{20}}{I_Z}\right| < \frac{2\kappa \cdot S_Z}{Q_{30} \cdot R^2}, \tag{3.33}$$

We call $|\Delta q_{20}/I_Z|$ differential (gravitational) quadrupole moment.

We can use the same argument for the other quadrupole moments (q_{21} and q_{22}) when the axial-symmetry is not assumed. If the density of test masses is not homogeneous, other terms in the multipole moments could be dominant. It depends on the exact form of the inhomogeneities. We will discuss this in more detail in Section 3.6.1. For the density inhomogeneities which we observed, q_{20} were dominant (see Section 5.4).

3.4.2 Gravitational susceptibility

Gravitational susceptibility can be defined as follows [55]:

$$\chi_{diff} = \frac{\Delta a_Z}{a_{CM}} \tag{3.34}$$

$$= 4\pi G \sum_{l=0}^{\infty} \sum_{m=-l}^{l} \sqrt{\frac{(l+1-m)(l+1+m)}{(2l+1)(2l+3)}} \left(\frac{\Delta q_{lm}}{M_{TM}}\right) \frac{Q_{l+1,m}}{a_{CM}} \tag{3.35}$$

where a_{CM} is the first-order common-mode acceleration of test masses:

$$a_{CM} = G\frac{M_{SM}}{r^2} \tag{3.36}$$

where r is the distance between the centre of mass of the test mass and the source mass, as defined previously. Gravitational susceptibilities have to satisfy:

$$|\chi_{diff}| < \frac{S_Z}{a_{CM}} \tag{3.37}$$

3.4.3 Differential gravitational multipole moments per unit mass

From Equations (3.17) and (3.28), differential gravitational multipole moments per unit mass can be defined:

$$\left|\sum_{l=0}^{\infty}\sum_{m=-l}^{l}\left(\frac{\Delta q_{lm}}{M_{TM}}\right)\right| < \left|\frac{1}{4\pi G}\sum_{l=0}^{\infty}\sum_{m=-l}^{l}\sqrt{\frac{(2l+1)(2l+3)}{(l+1-m)(l+1+m)}}\frac{S_Z}{Q_{l+1,m}}\right| \tag{3.38}$$

Differential gravitational multipole moments per unit mass are determined only by the details of the test mass. The limit on them is determined only by the details of source mass ($Q_{l+1,m}$).

3.4.4 Summary

We have described the definitions of three quantities that express the magnitude of multipole moments of test masses. The characteristics of the quantities are summarized in Table 3.1. Differential gravitational multipole moments per unit mass ($\Delta q_{lm}/M_{TM}$) and differential quadrupole moments ($\Delta q_{20}/I_Z$) do not depend on the details of the source mass. However, susceptibilities (χ_{diff}) depend on r. The limits on $\Delta q_{lm}/M_{TM}$ and on χ_{diff} are determined only by the details of the source mass, while the limit on $\Delta q_{20}/I_Z$ depends on the size of the test mass (R) (see the right-hand side of Equation (3.33)).

$\Delta q_{lm}/M_{TM}$ is useful when one wishes to independently determine the quantity, to indicate the magnitude of multipole moments of a test mass, and the limit on the quantity. However, $\Delta q_{lm}/M_{TM}$ is not dimensionless. χ_{diff} has been used during the optimization of the shape design of STEP test masses (see Section 3.5). We use $\Delta q_{lm}/M_{TM}$

Quantity	Dependence on details of TM	Dependence on details of SM	Limit is determined by
q_{20}/I_Z	Yes (q_{20} and R)	No	Q_{30} and R
χ_{diff}	Yes (q_{lm})	Yes ($Q_{l+1,m}$ and a_{CM} (or r^l))	a_{CM}
q_{lm}/M_{TM}	Yes (q_{lm} and M_{TM})	No	$Q_{l+1,m}$

Table 3.1: Summary of the quantities to express the magnitudes of multipole moments of STEP test masses. The second and the third columns are the dependence of the quantities on details of the test mass (TM) and the source mass (SM), respectively. Yes/No means that the quantity depends/does not depend on the details of the test mass or the source mass. The fourth column is the parameters that determine the limits on the quantities.

when we estimate the allowable levels of density inhomogeneities as the calculation becomes simple due to cancellation of M_{TM} and also dimensionless arguments are not required in the calculations (Chapter 4). Use of $\Delta q_{20}/I_Z$ is not convenient to estimate the allowable levels of density inhomogeneities as the moment of inertia depends on the density distribution. We use $\Delta q_{20}/I_Z$ in the estimation of the allowable level of anisotropy of thermal expansion of a test mass as dimensionless arguments without any information on the source mass is convenient for this purpose (Section 6.2).

3.5 Shape design of STEP test masses

The current design of the STEP test masses by Lockerbie is shown in Figure 3.1 [45]. The dimensions (R1, R2, R3, L1 and L2 in Figure 3.1) are given in Table 3.2. The contributions to the susceptibility for a source mass at $r = 250$ mm is given in Table 3.3. Radii of 0.2 mm for the internal machined edges, and 0.2 mm external chamfers on these test masses were taken into account in the estimation.

A test mass in the form of a solid or hollow cylinder without a belt can be designed to have $q_{20} = 0$ and q_{60}, q_{80}, q_{10}, etc. very close to zero. However, q_{40} can never be nulled. The belted cylindrical shapes allow to have $q_{20} = q_{40} = 0$. Also, there are sufficient dimensional degrees of freedom to control the higher moments in the belted cylindrical shapes. The belted cylindrical shapes were originally discussed by Cook [65] and were suggested for STEP by Speake [46].

By taking advantage of the belted cylindrical shapes, the current designs were chosen to have q_{20}, q_{40} and q_{60} nominally zero for the two test masses, and to minimize the absolute difference of q_{80} terms [42, 45] (see Table 3.3).

By summing each contributions of multipole moments to the susceptibility in Table 3.3, we obtain +0.06 ppm and -4.71 ppm for the inner test mass and the outer test mass, respectively. Therefore, the gravitational susceptibility is -4.77 ppm (outer-inner) by taking the difference between them.

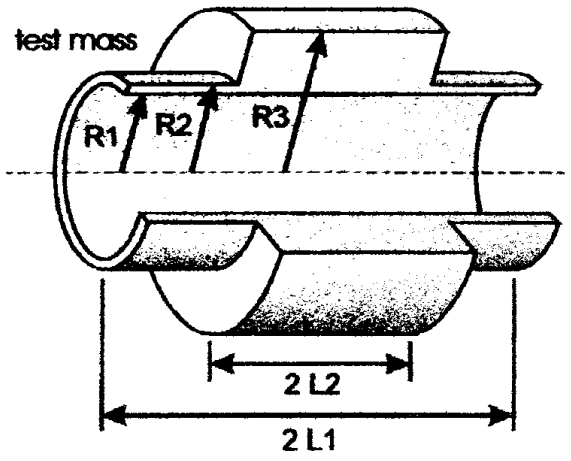

Figure 3.1: A cut-away view of a STEP test mass (quoted from [45]). Nomenclature used in Table 3.2 is defined in this figure.

	Outer test mass [mm]	Inner test mass [mm]
R1	24.237	5.100
R2	26.739	10.950
R3	43.122	19.237
L1	69.416	21.158
L2	31.364	11.948

Table 3.2: Dimensions of STEP test masses at the operating temperature, 1.8 K

	Quadrupole	Hexadecapole	64-pole	256-pole	1024-pole
Inner test mass	0.02	0.01	0.03	0.00	0.00
Outer test mass	-0.03	-0.01	0.03	-4.25	-0.45

Table 3.3: Contributions to the gravitational susceptibility of the STEP test masses, expressed in parts per million, for a source mass at 250 mm from the common centre of mass of the test masses (quoted from [45]).

Machining tolerances on the test masses, including those on parallelism and concentricity, were derived by Lockerbie to limit the multipole moments. From his analysis, the machining tolerances required for the STEP test masses are better than 1 μm [66, 67].

3.6 Metrological aspects

As one can see in the definition of the gravitational multipole moments (Equation (3.9)), they depends on the density variation ($\rho(\mathbf{x}')$). Thermal distortion changes the shape of a test mass and affects the limits of the integral of the gravitational multipole moments. In this section, an introduction to the main topics of this thesis will be presented.

3.6.1 Density inhomogeneities

Davis and Quinn have demonstrated high precision measurements of density inhomogeneities for STEP using a hydrostatic weighing method [68]. We will estimate allowable density variations for STEP test masses in Chapter 4. We will report measurements of the density inhomogeneities in materials intended to be employed in STEP by using the hydrostatic weighing method in Chapter 5. In addition, we will estimate the disturbance which would be produced by these density inhomogeneities (Chapter 5).

Density inhomogeneities of lth power dominantly contribute to lth multipole moments. Density inhomogeneities of higher terms (such as a cubic variation ($l = 3$) or higher ($l > 3$)) would be more unlikely to occur in materials. In addition, as mentioned before, higher terms in acceleration decay more quickly.

Dipole moments could be the dominant term for some density variations (e.g. a linear density variation along the z-axis). As one can see in Equation (3.19), dipole moments (q_{10}) couple to Q_{20} [56]:

$$Q_{20} = \sqrt{\frac{5}{4\pi}} \left(\frac{3}{2} \cos^2 \theta - \frac{1}{2} \right) \frac{M_{SM}}{r^3} \tag{3.39}$$

$$= \sqrt{\frac{5}{4\pi}} \left(\frac{3}{4} \cos 2\theta - \frac{1}{4} \right) \frac{M_{SM}}{r^3} \tag{3.40}$$

One can see that Q_{20} does not have $\cos\theta/\sin\theta$ terms, which produce spurious signals at the expected signal frequency. Other Q_{2m} do not have $\cos\theta/\sin\theta$ terms either. However, Q_{3m}, which couple to quadrupole moments of test masses, include $\cos\theta$ terms

(see Equations (3.42) and (3.42)). Therefore, quadrupole moments would be generally the dominant term to contribute the differential acceleration.

In fact, Q_{3m} do not fully contribute to produce spurious acceleration at the signal frequency [69], as shown below [56]:

$$Q_{30} = \sqrt{\frac{7}{4\pi}}\left(\frac{5}{2}\cos^2\theta - \frac{3}{2}\cos\theta\right)\frac{M_{SM}}{r^4} \tag{3.41}$$

$$= \sqrt{\frac{7}{4\pi}}\left(\frac{5}{8}\cos 3\theta + \frac{3}{8}\cos\theta\right)\frac{M_{SM}}{r^4} \tag{3.42}$$

Other Q_{3m} terms have a similar $\cos\theta$ dependence.

However, during the process of designing STEP test masses, χ_{diff} was estimated by assuming that all the terms of Q_{3m} contribute to the spurious acceleration (see the definition of χ_{diff} in Equation (3.35)). This overestimates, for example the contribution of q_{20} to χ_{diff}, by approximately a factor of 3.

However, at the moment, it is impossible to give precise arguments on the allowable level of multipole moments of STEP test masses because of lack in information on the details of source masses. We follow the conventional way of estimation of the gravitational multipole moments, used for the shape design of STEP test masses (Section 3.5); we consider all terms in Q_{3m} and use its maximum value in the estimation of allowable level. We will review the allowable level in Section 3.7.

3.6.2 Thermal distortion

STEP test masses will be operated in liquid helium. Even test masses designed by carefully considering their gravitational behavior could disturb the STEP experiment

if they deform at the cryogenic temperature from the machined shape at room temperature. We discuss the acceptable level of thermal distortion for STEP test masses by considering a change of the aspect ratio of a simple cylinder (Chapter 6). Also, we investigate thermal distortion of the materials intended to be employed in STEP by surveying existing literature (Chapter 6) and by experiments developed by ourselves (Chapter 7).

3.7 Allowable levels of the differential gravitational multipole moments

In this section, we review allowable levels of the gravitational moments of test masses. We focus on quadrupole moments because they would be the dominant term to contribute spurious acceleration.

As described before, the differential acceleration, between a pair of test masses, is to be measured with a sensitivity of 10^{-18}g in the STEP experiment. Thus, the target noise level should be below $10^{-18}\mathrm{m/s^2}$.

In Section 3.5, we have reviewed that the gravitational susceptibility of a pair of perfect STEP test masses is approximately 5 ppm (r = 250 mm). For this pair of test masses to achieve the required noise level of $10^{-18}\mathrm{m/s^2}$, the source mass has to be smaller than 0.5 g (Equation (3.37)).

The requirements for the performance of aerogel confinement, which is expected to reduce the helium bubble motion, depends on how small the gravitational susceptibility is. In other words, the allowable level of the gravitational susceptibility depends on

how good the performance of the aerogel confinement technique is. The STEP team plans to estimate the noise level due to the helium bubble by checking the performance of the aerogel confinement techniques [70]. At the moment, we use a conventional noise source described below.

Conventionally, the design of the STEP test masses has been done by aiming to achieve the gravitational susceptibility ($r = 250$ mm) less than a few parts per million [38, 42]. A part per million (1 ppm) of the gravitational susceptibility ($r = 250$ mm) corresponds to the level that is just enough to achieve the required noise level (10^{-18} m/s^2) when a 1-g spherical helium bubble[3] at 250 mm away from the test mass is acting as a source mass (the common mode acceleration is approximately 1×10^{-12} m/s^2). We use this conventional noise source of 1-g helium-bubble at 250 mm throughout this thesis.

For this noise source, Q_{30} in Equation (3.33) is as follows from Equation (3.10)[4]:

$$Q_{30} = \sqrt{\frac{7}{4\pi}} \frac{0.001[\mathrm{kg}]}{0.25^4[\mathrm{m}^4]} \sim 0.2 \tag{3.43}$$

Therefore, the condition (3.33) becomes:

$$\left| \frac{\Delta q_{20}}{I_Z} \right| < 1 \times 10^{-5}, \tag{3.44}$$

for a test mass with radius of 50 mm. 50 mm-radius was used here because it is roughly the size of an outer STEP test mass (see Figure 3.1 and Table 3.2).

[3]The radius of 1-g spherical liquid helium (density of 145.6 kg/m^3 at 2 K) is roughly 12 mm.

[4]As described in Section 3.6.1, we use all the terms of Q_{30} though we note that only the $\cos\theta$ (or $\sin\theta$) term could be a significant disturbance for STEP.

From Equations (3.38) and (3.43), we obtain the following condition for quadrupole moment per unit mass by assuming the conventional noise source,

$$\left|\frac{\Delta q_{20}}{M_{TM}}\right| < 1 \times 10^{-8}[\mathrm{m}^2] \tag{3.45}$$

It would be impossible to make the imperfections, such as density inhomogeneities and thermal distortion, identical for each test mass of a pair. Therefore, each test mass should satisfy the conditions described above, namely:

$$\left|\frac{q_{20}}{I_Z}\right| < 10^{-5}(R = 50\mathrm{mm}) \tag{3.46}$$

$$\chi_a < 10^{-6}(r = 250\mathrm{mm}) \tag{3.47}$$

$$\left|\frac{q_{20}}{M_T}\right| < 10^{-8}[\mathrm{m}^2] \tag{3.48}$$

where $\chi_a = a_Z/a_{CM}$. Here, the limits are expressed in terms of q_{20} (except χ_{diff}) for simplicity. But other quadrupole moments (q_{21} and q_{22}) are equally important.

3.8 Summary

We have seen that the shapes of STEP test masses are optimized to reduce spurious differential acceleration of the test masses. Even if the test masses are designed carefully, imperfections in test mass materials, such as their density inhomogeneities and thermal distortion, could produce extra gravitational multipole moments. The differential acceleration due to those imperfections should be sufficiently smaller than the required noise level of $10^{-18}\mathrm{m/s}^2$. We have reviewed three quantities that express the magnitude of gravitational moments of test masses and discussed the allowable levels:

the gravitational quadrupole moments of each test mass ($|q_{20}/I_Z|$) should be less than a level of 10 ppm ($R = 50$ mm); the gravitational susceptibility should be less than 1 ppm ($r = 250$ mm); the quadrupole moments per unit mass should be less than 10^{-8} m^2. We assume the conventional noise source of 1-g helium bubble at 250 mm from the test masses. In this thesis, we deal with the density inhomogeneities and thermal distortion.

Chapter 4

Allowable levels of density inhomogeneities

We have measured the density inhomogeneities of two materials, which are intended to be used as the STEP test masses: HIPed beryllium and niobium, using the hydrostatic weighing method (see Chapter 5). Before we get into the description of the measurements, we discuss the allowable levels of the density inhomogeneities for typical density variations in this chapter. We also discuss the required precision in the hydrostatic weighing method in Section 4.2.

4.1 Allowable levels of density inhomogeneities

4.1.1 Introduction

We consider the quadrupole moments as they would dominantly contribute to the differential acceleration, as discussed in Section 3.6.1. For example, q_{20} is given as follows from Equation (3.9):

$$q_{20} = \int_v \rho(\mathbf{x}') r'^2 Y_{20}^*(\theta') d^3x' \tag{4.1}$$

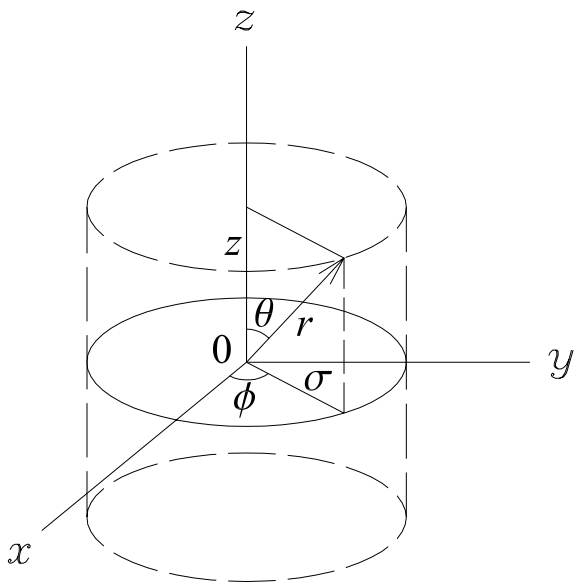

Figure 4.1: Coordinate systems

$$= \sqrt{\frac{5}{4\pi}} \int_v \rho(\mathbf{x}') r'^2 \left(\frac{3}{2} \cos^2 \theta' - \frac{1}{2} \right) d^3x', \tag{4.2}$$

where

$$r' = \sqrt{\sigma'^2 + z'^2} \tag{4.3}$$

$$\cos \theta' = \frac{z'}{\sqrt{\sigma'^2 + z'^2}} \tag{4.4}$$

Therefore, they become, in the cylindrical coordinates (see Figure 4.1):

$$q_{20} = \sqrt{\frac{5}{4\pi}} \int_v \rho(\mathbf{x}')(\sigma'^2 + z'^2) \left(\frac{3}{2} \cdot \frac{z'^2}{\sigma'^2 + z'^2} - \frac{1}{2} \right) \sigma' d\sigma' d\phi' dz' \tag{4.5}$$

$$= \frac{1}{4} \sqrt{\frac{5}{\pi}} \int_v \rho(\mathbf{x}')(2z'^2 - \sigma'^2) \sigma' d\sigma' d\phi' dz'. \tag{4.6}$$

We consider a cylinder as a test mass, instead of a belted cylinder, for simplicity[1]. The quadrupole moments of a cylinder are zero when it has an aspect ratio of $R/L =$

[1]Multipole moments of a belted cylinder can be obtained by adding and subtracting multipole moments of simple cylinders.

$2/\sqrt{3}$, where R and L are the radius and the half-length of the cylinder. We assume that the cylinder has this aspect ratio with $R = 50$mm ($L \simeq 43$mm), which is roughly the size of the belt of a STEP outer test mass[2] (Table 3.2).

Spherical harmonics used in the following calculations are quoted from [56] and listed in Appendix A.

Density distributions of cylindrical materials proportional to σ^2 [71] in the radial direction and proportional to z [68, 72] in the axial direction of the cylindrical coordinates, and a $\cos\theta$ angular density variation [72] have been reported:

Fitzgerald et al [71] reported that a stainless steel rod (approximately 100 mm in diameter and 1 m long) had density variation, proportional to σ^2 in the radial direction, of 250 ppm over the diameter, and no significant differences along the axial and angular directions. The uncertainty in the hydrostatic weighing measurements was approximately $\pm$ 30 ppm.

Davis and Quinn [68] reported that a Cu-2%Te rod (80 mm in diameter and 500 mm long) had 40 ppm linear density variation along the z-axis over 500 mm. The uncertainty in the hydrostatic weighing was a few ppm. Also, Quinn et al [72] reported that the density in Cu-0.7%Te rods varied linearly across the diameter (about 120 mm) by about 100 to 200 ppm and linearly along the axial direction by 100 ppm over roughly 120 mm.

We examine the density inhomogeneities that are likely to occur in each of the three

[2]The belt of an outer test mass has an aspect ratio of $R3/L2 \sim 1.4$ (Table 3.2), which is close to $2/\sqrt{3}$.

directions: the radial, axial and angular direction in the cylindrical coordinate system. We examine continuous functions of density variations and, in addition, a case of the existence of a void.

As for the radial direction, we examine the density variation proportional to σ^2 (Section 4.1.2). The term proportional to σ is not a continuous density variation across the diameter. As regards the axial direction, the term proportional to z and z^2 are considered (Section 4.1.3). The term proportional to z results in shifting the centre of mass of the test mass from the centre of figure. The multipole moments have to be integrated over the test mass with the origin at the centre of mass of the test mass; the centres of mass of the pair of the test masses are going to be adjusted to coincide as mentioned in Section 2.4.1. As regards the angular direction, the term of $\cos n\phi$ is considered, where n is an integer. As we will see in Section 4.1.4, the first term to contribute to the quadrupole moments is $\cos 2\phi$. We estimate the allowable density inhomogeneities for the $\cos 2\phi$. Higher terms may be more unlikely to occur in materials.

4.1.2 Radial density inhomogeneities

We consider the density variation $\rho(\sigma') = \rho_0(1 + A\sigma'^2)$, where ρ_0 is a standard density and A is a constant. From Equation (4.6), the quadrupole moments become as follows for this density variation:

$$q_{20} = \frac{2\pi}{4}\sqrt{\frac{5}{\pi}}\int_{-L}^{L}\int_{0}^{R}\rho_0(1 + A\sigma'^2)(2z'^2 - \sigma'^2)\sigma' d\sigma' dz' \tag{4.7}$$

$$= \frac{1}{48}\sqrt{\frac{5}{\pi}} A M_{TM} R^4 \frac{\rho_0}{\rho} \tag{4.8}$$

where M_{TM} is the mass of the test mass:

$$M_{TM} = 2\pi R^2 L \rho. \tag{4.9}$$

ρ is the average density of test mass[3]. From Equation (4.8),

$$\frac{q_{20}}{M_{TM}} = \frac{1}{48}\sqrt{\frac{5}{\pi}} A R^4 \frac{\rho_0}{\rho} \tag{4.10}$$

To satisfy the condition (3.48), the density variation over the radius of 50 mm ($R =$ 50mm) has to be:

$$\left| \frac{A R^2 \rho_0}{\rho} \right| < 48\sqrt{\frac{\pi}{5}} \frac{1}{R^2} \times 1 \times 10^{-8} \sim 2 \times 10^{-4}. \tag{4.11}$$

4.1.3 Axial density inhomogeneities

Density variation proportional to z'

We consider the density variation $\rho(z') = \rho_0(1 + B_1 z')$, where B_1 is a constant . The quadrupole moment, Equation (4.6), vanishes because of the odd functions of z' in the integral over z' from $-L$ to L. However, as mentioned previously, the integral must be calculated with the origin at the centre of mass of the test mass, instead of the centre of figure.

The position of the test mass shifts by l_z when its centre of mass is shifted from the centre of figure by l_z. Multipole moments of the shifted test mass can be obtained by using the formula by D' Urso and Adelberger, Equation (3.14).

[3] ρ_0/ρ is nominally one.

With this formula, the quadrupole moment is:

$$\widetilde{q_{20}} = 2\sqrt{\frac{5}{3}} q_{10} l_z, \tag{4.12}$$

where q_{10} is given as follows from Equation (3.9):

$$\begin{aligned} q_{10} &= \int_v \rho(\mathbf{x}') r' Y_{10}^* d^3x' && (4.13)\\ &= \sqrt{\frac{3}{4\pi}} \int_{-L}^{L} \int_0^{2\pi} \int_0^R \rho_0 (1 + B_1 z') z' \sigma' d\sigma' d\phi' dz' && (4.14)\\ &= \frac{4\sqrt{3\pi}}{9} \rho_0 B_1 L^5. && (4.15) \end{aligned}$$

l_z can be obtained as follows:

$$\begin{aligned} l_z &= \frac{\int_v \rho(z') \cdot z' d^3x'}{M_{TM}} && (4.16)\\ &= \frac{1}{3} B_1 L^2 \frac{\rho_0}{\rho}. && (4.17) \end{aligned}$$

With Equations (4.15) and (4.17) the quadrupole moment is as follows:

$$q_{20} = \frac{8\sqrt{5\pi}}{27} \frac{(\rho_0 B_1)^2}{\rho} L^7. \tag{4.18}$$

By dividing this by M_{TM} (Equation (4.9)),

$$\frac{q_{20}}{M_{TM}} = \frac{1}{9} \sqrt{\frac{5}{\pi}} \left(\frac{\rho_0 B_1}{\rho} \right)^2 L^4. \tag{4.19}$$

To satisfy the condition (3.48), the relative difference in density over the half-length L (= 43 mm) should satisfy the following condition:

$$\left| \frac{\rho_0 B_1 L}{\rho} \right| < \sqrt{\frac{1 \times 10^{-8}}{\frac{1}{9}\sqrt{\frac{5}{\pi}} L^2}} \sim 6 \times 10^{-3}. \tag{4.20}$$

By using Equations (4.17) and (4.20), the shift, l_z, should satisfy the following condition:

$$l_z < 2 \times 10^{-3} L. \tag{4.21}$$

Density variation proportional to z'^2

As for the density variation proportional to z'^2 ($\rho(z') = \rho_0(1 + B_2 z'^2)$), the quadrupole moment is given as follows from Equation (4.6):

$$\begin{aligned} q_{20} &= \frac{2\pi}{4}\sqrt{\frac{5}{\pi}}\int_{-L}^{L}\int_{0}^{R}\rho_0(1+B_2 z'^2)(2z'^2-\sigma'^2)\sigma' d\sigma' dz' && (4.22)\\ &= \frac{2}{45}\sqrt{\frac{5}{\pi}}B_2 M_{TM} L^4 \frac{\rho_0}{\rho}, && (4.23) \end{aligned}$$

where B_2 is a constant. Therefore,

$$\frac{q_{20}}{M_{TM}} = \frac{2}{45}\sqrt{\frac{5}{\pi}}B_2 \frac{\rho_0}{\rho} L^4 \tag{4.24}$$

To satisfy the condition (3.48), the relative difference in density over the half-length ($L = 0.43$ mm) has to satisfy the following condition:

$$\left|\frac{B_2 L^2 \rho_0}{\rho}\right| < \frac{45}{2}\sqrt{\frac{\pi}{5}}\frac{1}{L^2} \times 10^{-8} \sim 1 \times 10^{-4} \tag{4.25}$$

4.1.4 Angular density inhomogeneities

We consider the density variation $\rho(\phi') = \rho_0(1 + \sum_n C_n \cos n\phi')$, where C_n is a constant and n is an integer. For these density inhomogeneities the quadrupole moments to be considered are q_{21} and q_{22}. However, q_{21} is zero by calculating it from Equation (3.9) because of the integral of the odd function of z' from $-L$ to L.

q_{22} is as follows from Equation (3.9):

$$\begin{aligned} q_{22} &= \int \rho(\mathbf{x}') r'^2 Y_{22}^*(\theta', \phi') d^3x' && (4.26) \\ &= \frac{1}{4}\sqrt{\frac{15}{2\pi}} \int_{-L}^{L} \int_0^{2\pi} \int_0^R \rho_0 (1 + \sum_n C_n \cos n\phi') \sigma'^3 \\ &\quad (\cos 2\phi' - i \sin 2\phi') d\sigma' d\phi' dz' && (4.27) \\ &= \frac{3}{16}\sqrt{\frac{5\pi}{2}} C_2 \rho_0 R^5. && (4.28) \end{aligned}$$

Therefore,

$$\frac{q_{22}}{M_{TM}} = \frac{1}{8}\sqrt{\frac{15}{8\pi}} C_2 R^2 \frac{\rho_0}{\rho} \tag{4.29}$$

Using Equation (3.38),

$$\frac{q_{22}}{M_{TM}} < \frac{\sqrt{7}}{4\pi G} \frac{S_Z}{Q_{32}}. \tag{4.30}$$

From Equation (3.10) (see discussion on Q_{3m} in Section 3.6.1)[4]:

$$Q_{32} = \frac{1}{16}\sqrt{\frac{105}{\pi}} \frac{0.001[\mathrm{kg}]}{0.25^4[\mathrm{m}^4]} \sim 0.1[\mathrm{kg/m}^4] \tag{4.31}$$

for the source mass of 1-g helium bubble at 250 mm away from the test mass. Therefore, the required level for q_{22} is:

$$\left| \frac{q_{22}}{M_{TM}} \right| < 3 \times 10^{-8} [\mathrm{m}^2]. \tag{4.32}$$

With Equation (4.29), the allowable level of the density inhomogeneities over the radius of R (= 50 mm) is as follows:

$$\left| \frac{C_2 \rho_0}{\rho} \right| < 8\sqrt{\frac{8\pi}{15}} \frac{1}{R^2} \times 3 \times 10^{-8} \sim 1 \times 10^{-4}. \tag{4.33}$$

[4]When we consider only the $\cos\theta$ term, we obtain: $Q_{32} = \frac{1}{16}\sqrt{\frac{105}{2\pi}} \frac{0.001[\mathrm{kg}]}{0.25^4[\mathrm{m}^4]} \sim 0.1[\mathrm{kg/m}^4]$.

4.1.5 Void

We consider the presence of a void (radius r_{void}), which is inside of a test mass. The worst case would be when the void is at the end of the z-axis of the cylinder, namely at $(\sigma_{void}, z_{void}) = (0, L - r_{void})$. Then, the centre of mass of the test mass shifts from the centre of figure by l_{void}. The shifted quadrupole moments are given by Equation (4.12).

The shift is given as follows from Equation (4.16):

$$l_{void} = -\frac{m_{void} \cdot z_{void}}{M_{TM}}, \tag{4.34}$$

where m_{void} is the lacking mass due to the void. The void is assumed as a sphere. From Equations (4.13) and (4.34):

$$q_{10} = -\sqrt{\frac{3}{4\pi}} m_{void} z_{void} \tag{4.35}$$

$$= -\sqrt{\frac{3}{4\pi}} l_{void} M_{TM} \tag{4.36}$$

Therefore, we obtain:

$$q_{20} = \sqrt{\frac{5}{\pi}} M_{TM} l_{void}^2. \tag{4.37}$$

Therefore,

$$\frac{q_{20}}{M_{TM}} = \sqrt{\frac{5}{\pi}} l_{void}^2 [\mathrm{m}^2] \tag{4.38}$$

In order to satisfy the condition (3.48):

$$|l_{void}| < 90 \mu\mathrm{m} \tag{4.39}$$

Equation (4.34) can be written as follows by noting that $m_{void} = \frac{4}{3}\pi r_{void}^3 \rho$ and by using Equation (4.9):

$$\frac{l_{void}}{L} = \frac{1}{2}\nu^3(1-\nu) \tag{4.40}$$

where

$$\nu = \frac{r_{void}}{L}. \tag{4.41}$$

In order to satisfy the condition (4.39):

$$r_{void} < 0.17L. \tag{4.42}$$

where $\nu \ll 1$ was assumed. The relative density variation due to the void with the maximum allowed radius is:

$$\frac{\Delta\rho}{\rho} = \frac{V_{void}}{V_{TM}} < \frac{\frac{4}{3}\pi(0.17L)^3}{\frac{8}{3}\pi L^3} \sim 3 \times 10^{-3}, \tag{4.43}$$

where V_{void} and V_{TM} are the volume of the void and the test mass, respectively.

4.1.6 Summary

The results obtained from the above calculations are summarized in Table 4.1. The quadratic density variations (σ^2 and z^2) would cause more significant disturbances than the linear density variation (z). One of the most stringent requirements comes from the angular density distribution. However, among the others, this density variation would be the most unlikely to occur in materials.

Density variation	Maximum allowed density variation: $\frac{\Delta\rho}{\rho}$	Maximum allowed shift of the centre of mass: $\frac{l}{L}$
σ^2	2×10^{-4}	n.a.
z	6×10^{-3}	2×10^{-3}
z^2	1×10^{-4}	n.a.
$\cos 2\phi$	1×10^{-4}	n.a.
void	3×10^{-3}	2×10^{-3}

Table 4.1: Summary of the allowable levels of the density inhomogeneities for a simple cylinder with the aspect ratio of $R = 2L/\sqrt{3}$ (= 50 mm). The first column is the density variations considered in this chapter. The second and the third columns are the allowable levels of the density variations and the relative shifts of the centre of mass, respectively. (n.a. indicates not applicable.)

4.2 Required precision for the measurements of density inhomogeneities

We have reviewed the allowable levels of various density inhomogeneities in the previous sections. The most strict requirement of 100 ppm in the relative difference in density comes from the quadratic density variations and the angular density inhomogeneity (Table 4.1). The relative density differences that we measure using the hydrostatic weighing method may be smaller than the actual density variation in the samples because of the cancellation of the variation over the volume of the samples.

As we will describe in Section 5.2, the relative density difference between samples were determined by the measurements of the apparent weights of the samples in air and in a liquid. The uncertainty in the measurements is approximately proportional to $\sqrt{2}\delta m_L/\rho_L V$ (Equation (5.11)), where δm_L is the uncertainty in the measured apparent weight in the liquid. ρ_L and V are the density of the liquid and the volume of the

sample, respectively.

For a sample with volume of 25 cm^3, δm_L has to be less than approximately 880 μg with water as the liquid ($\rho_L \sim 1 g/cm^3$) to achieve the precision of 50 ppm.

The device, developed by Davis [68] at BIPM (Bureau International des Poids et Mesures), to measure density differences between samples by using the hydrostatic weighing method has sufficient precision (a few ppm or $\delta m \sim 50\mu$g, see Section 5.4). We have conducted measurements using the device at BIPM as we will discuss in Chapter 5.

4.3 Conclusions

We have estimated the allowable levels of the density inhomogeneities. The most stringent requirement comes from the quadratic density variations and the angular density variation. From this requirement, the precision better than 50 ppm in the relative difference in density is necessary for the measurements.

Chapter 5

Measurements of Density Inhomogeneities

In this chapter, we will describe the measurements of the density inhomogeneities of materials to be used for the STEP test masses using the hydrostatic weighing method.

First, we will view the dissection of our samples in Section 5.1. Then, we will describe the hydrostatic weighing method in Section 5.2 and the measurements in Section 5.3. The results are presented in Section 5.4. Discussion and conclusions follow.

5.1 Samples

5.1.1 Specifications

A HIPed (hot isostatically pressed) beryllium rod (approximately 140 mm long by a diameter of 90 mm) of grade I220-H was purchased from Brush Wellman Inc. A niobium rod (approximately 225 mm long by a diameter of 45 mm) of grade RRR was purchased from the Wah Chang Company. The respective companies recommended these grades as they were ones of the most uniform or chemically pure grades among

others[1].

5.1.2 Dissection

The samples have to be dissected in a way to give enough information to examine the typical density variations, which were discussed in Chapter 4. For this purpose, we have considered two aspects: the number of sampling points and the volume of the samples.

In Chapter 4, we have discussed the levels of allowable density variations for STEP test masses. We have seen that the axial density variation proportional to z and the existence of a void are not as critical as the others. To test the quadratic radial density distribution (σ^2 variation, see Section 4.1.2), at least three sampling points across the diameter are required. For the density variation proportional to z^2 (see Section 4.1.3), at least three sampling points along the z-axis are required. To test the $\cos 2\varphi$ variation (see Section 4.1.4), at least five sampling points are required in the angular direction; if it is four, the variation could cancel out.

In summary, we need to have at least three sampling points across the diameter and along the z-axis, and five sampling points around the axial direction.

As we saw in Section 4.2, the uncertainty in the measurement of density inhomogeneities in the hydrostatic weighing method depends on the volume of the samples. We made sure that the volume of samples were large enough to achieve the required sensitivity (Section 4.2).

[1]The STEP team at Stanford University discussed with the respective companies and chose those grades.

By considering these two aspects, we chose the dissection methods for the beryllium and the niobium as shown in Figures 5.1 and 5.2.

As shown in these figures, a prototype outer test mass and a prototype inner test mass were made from the beryllium rod and the niobium rod, respectively. The remaining pieces of the rods were used for the density measurements.

5.1.3 Numbering

Numbering was done on each sample, as shown in Figures 5.1 and 5.2. Though it is not shown in the figures, a line was drawn on the samples to indicate their original orientation. With the numbering and the line, we can trace the original location and orientation exactly. For the analysis of the density inhomogeneities, we do not need the information of the orientation of the samples. However, it may be useful in the future if we need to perform further analysis with the samples.

5.2 Hydrostatic Weighing Method

When a standard sample (density ρ_S, volume V_S) is weighed on a balance, the reading in air (density ρ_A) and in a liquid (density ρ_L) is given as follows, respectively:

$$V_S(\rho_S - \rho_A) = f m_{SA} \tag{5.1}$$

$$V_S(\rho_S - \rho_L) = f m_{SL} \tag{5.2}$$

where f is a constant which is related to the calibration of the balance, and m_{SA} and m_{SL} denote the balance reading (apparent weight) when the standard is weighed in

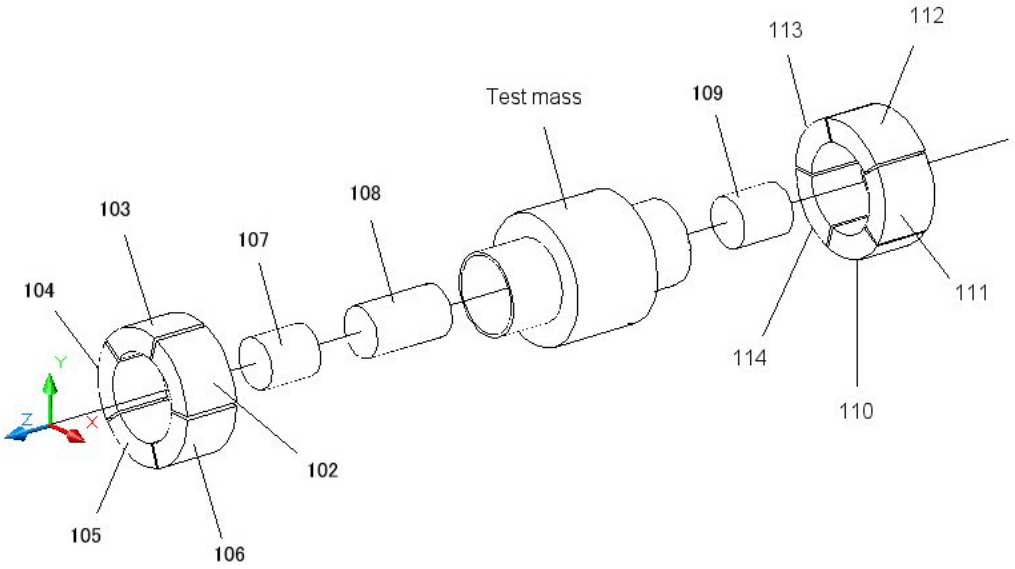

Figure 5.1: Dissection of the HIPed beryllium rod. A prototype outer test mass was made from the rod. The offcuts No. 102 through No. 114 were used for the homogeneity measurements.

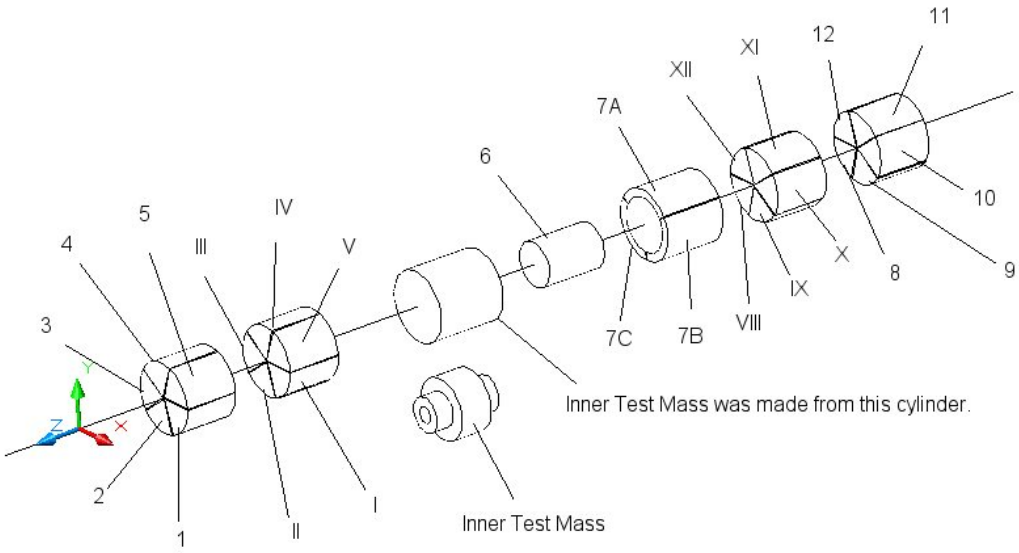

Figure 5.2: Dissection of the niobium rod. A prototype inner test mass was made from the rod. The pieces that are labelled with numbers were used for the homogeneity measurements.

air and in the liquid, respectively. Similarly, the following equations are obtained by weighing another sample (density ρ_X, volume V_X) in air and in the liquid with the same balance:

$$V_X(\rho_X - \rho_A) = f m_{XA} \tag{5.3}$$

$$V_X(\rho_X - \rho_L) = f m_{XL} \tag{5.4}$$

where m_{XA} and m_{XL} indicates the apparent weight of the sample in air and in the liquid, respectively.

By taking the ratios of Equation (5.1) and (5.2), and of Equations (5.3) and (5.4), we obtain the following equations:

$$\frac{\rho_S - \rho_A}{\rho_S - \rho_L} = \frac{m_{SA}}{m_{SL}} (\equiv R_S) \tag{5.5}$$

$$\frac{\rho_X - \rho_A}{\rho_X - \rho_L} = \frac{m_{XA}}{m_{XL}} (\equiv R_X). \tag{5.6}$$

Combining Equation (5.5) and (5.6), the relative density of a sample X to a sample S is given as follows [73]:

$$\frac{\rho_X}{\rho_S} = \frac{R_X}{R_S} \left(\frac{R_S - 1}{R_X - 1} \right) (1 + \delta) \tag{5.7}$$

where

$$\delta = \frac{\rho_A}{\rho_S (R_S - 1)} \left(1 - \frac{R_S}{R_X} \right). \tag{5.8}$$

Because δ is sufficiently small ($\delta < 10^{-6}$), Equation (5.7) becomes:

$$\frac{\rho_X}{\rho_S} = \frac{R_X}{R_S} \left(\frac{R_S - 1}{R_X - 1} \right). \tag{5.9}$$

Equation (5.9) can be written in a different way as follows [73]:

$$\frac{\rho_X}{\rho_S} = \left(1 - \frac{m_{SA} - m_{XA}}{m_{SA}}\right) \left\{ \frac{m_{SA} - m_{SL}}{m_{SA} - m_{SL} - (m_{SA} - m_{XA}) + (m_{SL} - m_{XL})} \right\}. \quad (5.10)$$

We used this formula to analyse data (see Section 5.3.2).

By propagating errors in the measurements, the uncertainty in the relative density is approximately given by[2]:

$$\delta\left(\frac{\rho_X}{\rho_S}\right) \simeq \sqrt{\left(\frac{\delta m_{XL}}{\rho_L V_X}\right)^2 + \left(\frac{\delta m_{SL}}{\rho_L V_S}\right)^2}, \quad (5.11)$$

where δm_{XL} and δm_{SL} is the uncertainty in the measurement of m_{XL} and m_{SL}, respectively. Here, it is assumed that $\rho_A \ll \rho_L$, $\rho_X \sim \rho_S$ and $\rho_L \ll \rho_X$. Also, it is assumed that the uncertainty in the measurement of the apparent weight in air is much less than the one in the liquid; this situation was observed in the measurements (Section 5.4.1).

5.3 Experiment

5.3.1 Overview of the device

The density measurements using the hydrostatic weighing method were carried out with a device which was developed by Davis at BIPM [68]. The device is mainly composed of a servo type balance (resolution 10μg, maximum capacity 205 g) and a liquid bath under the balance (Figure 5.3). The apparatus is capable of measuring up to four samples at the same time. To minimise force due to the surface tension on the

[2]Equation (5.11) is presented here to show the dominant terms in the uncertainty of the measurements. This equation was not used to analyse the data presented in this chapter.

suspension at the boundary of the air and the liquid, a liquid with small surface tension (nonane, density $0.72 g/cm^3$) and a suspension wire with small radius were chosen. The temperature of the liquid was not controlled. Measurements were done quickly in the small bath to minimize thermal effects in the liquid. The temperature ($22°C$) and the humidity (55%) in the laboratory was controlled continuously throughout the measurements.

5.3.2 Measurements

The samples were cleaned with an ultrasonic cleaner before the measurements. After the cleaning, they were wrapped in aluminium foil to keep them clean. The samples were weighed in air and then in the liquid. We measured the niobium samples first and then the beryllium samples.

When the samples were measured in the liquid, they were located on an aluminium disk (the diameter is 9 cm) fixed in the bath (the outside diameter and the depth are both roughly 15 cm). The disk has four small clearance holes (the diameter is 1.2 cm). Each sample was located over one of the holes in the disk. They were left in the liquid for more than one hour to allow them to thermalize, before the measurements were started.

A c-shaped device with a pan (the diameter is 0.8 cm) at the end was suspended from the bottom of the balance and immersed in the liquid. Because of the c-shape, the pan can get access through the holes from the bottom of the disk and it can lift a sample (Figure 5.4). The disk was manually controlled to locate the samples in the

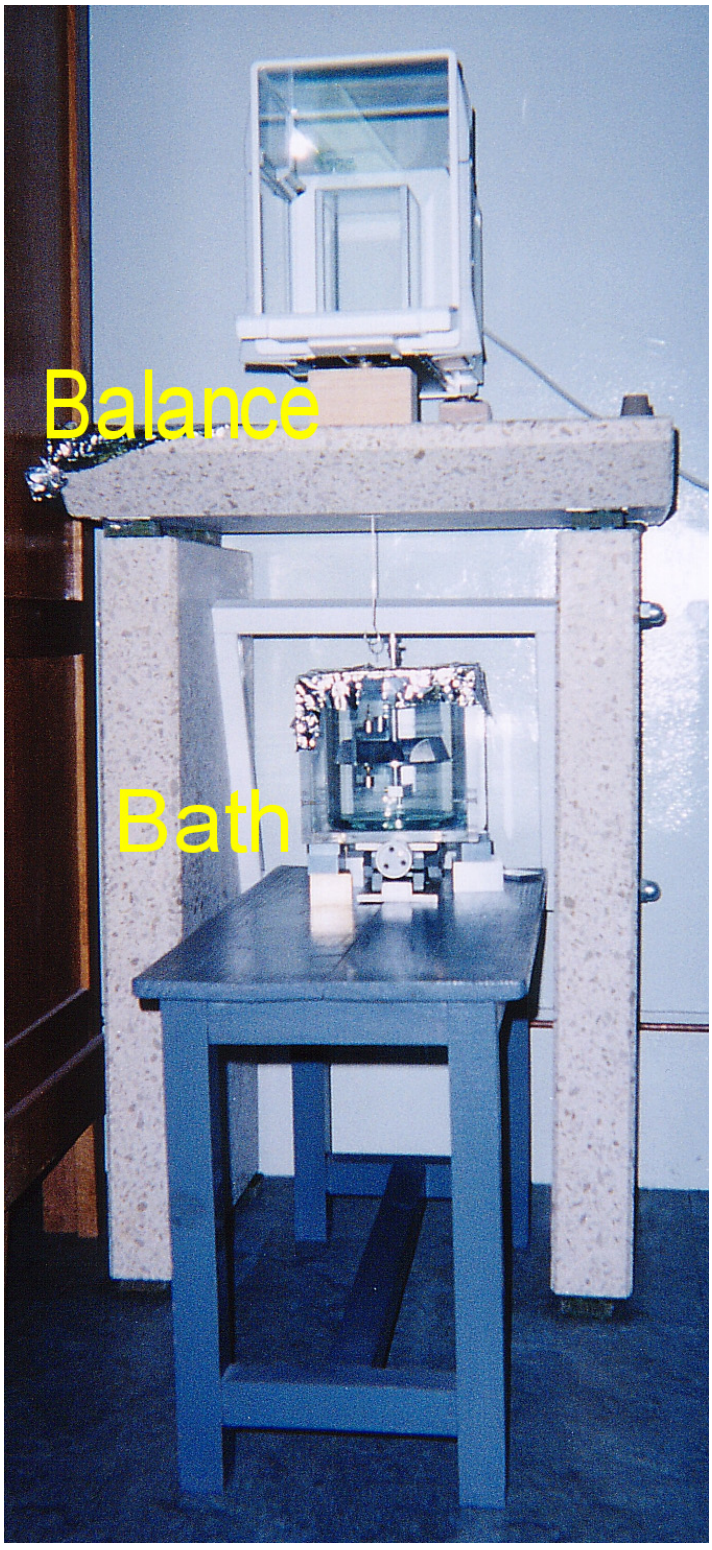

Figure 5.3: The device for the hydrostatic weighing at BIPM. The total height of the device is about 80 cm.

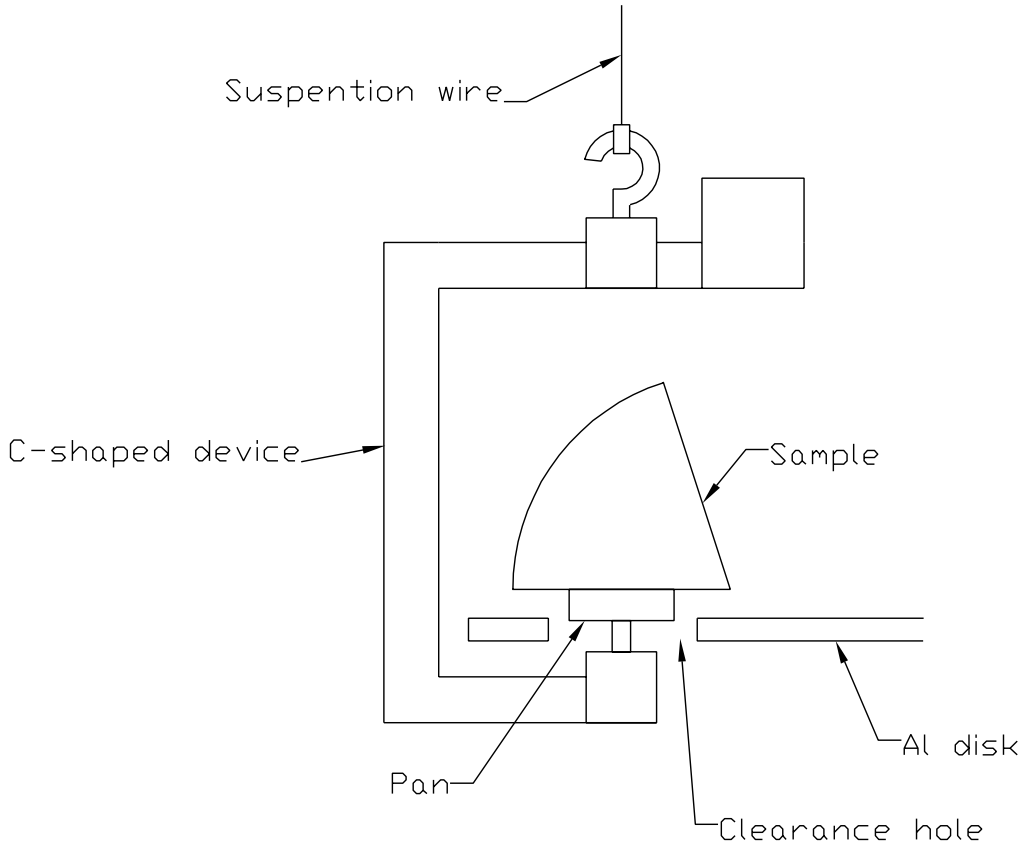

Figure 5.4: A schematic cross-section of the apparatus for hydrostatic weighing. A segmented sample is lifted by the pan in the liquid for measurement.

position to be lifted by the pan for the measurements. When one measurement was finished the disk was rotated to locate the next sample in the position to be lifted. The c-shaped device was not touched to avoid any fluctuation in the readings of the balance. The samples were weighed one by one in the order described below. The four samples were kept in the liquid until all of the measurements were completed.

Generally, one set of measurements was done with four samples. Two of them were used as standards. We used the same standards for all sets of measurements[3]. Samples with cylindrical shapes, such as the beryllium samples 107-109, and the niobium sample 6, were too large and did not fit on the disk to be measured in the liquid. Therefore, spoon-shaped tools were made to deal with them in the liquid (Figure 5.5). Because of the limited space in the bath, only one standard was used in the measurements for the beryllium sample 108.

We have measured their apparent weights in a symmetric order. For example, two standards (S1 and S2) and two samples (X1 and X2) were measured in the following order: S1, X1, S2, X2, S1, X2, S2, X1 and S1. This symmetrical measurement order helps to eliminate the drift, which is typically liner with time (see Section 5.4.1).

5.3.3 Measurement verification

The following checks were carried out to confirm the measurements. The first measurements were repeated after a series of measurements. Some of these measurements were repeated several days later. Some samples with greater density differences than

[3]Two niobium standards were used for the measurements of the niobium samples and two beryllium standards for the measurements of the beryllium samples.

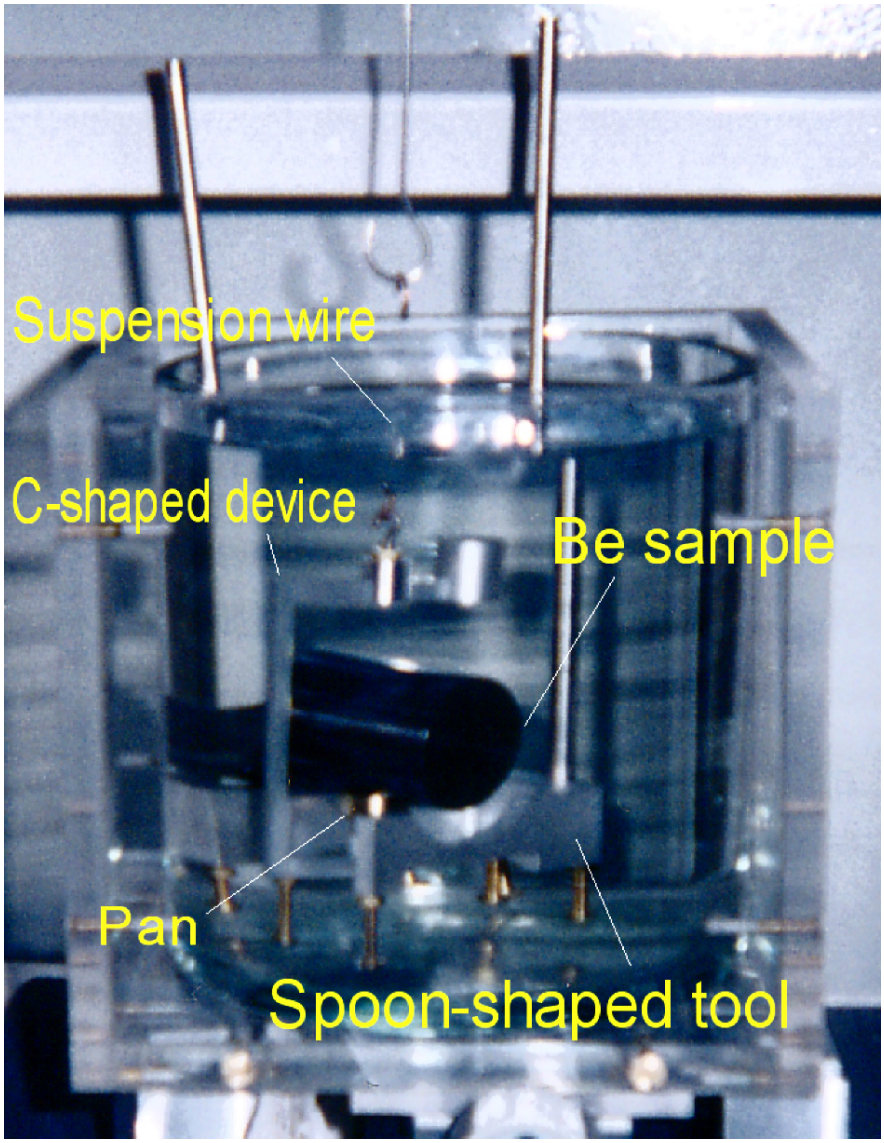

Figure 5.5: Sample 108 is weighed on the pan in the bath for the measurement. Spoon shaped tools were used to deal with the big sample.

others were measured twice. In all cases the measurements were reproducible within the range of uncertainties.

The difference in shape of the samples could give different results because of different convective flows when they are suspended in the liquid. The worst case would have occurred in the curved samples (niobium samples 7A-7C in Figure 5.2). We checked the difference between the measurements with both convex and concave samples. The results agreed with each other within the range of uncertainties.

The native oxide, upon exposure to air, of the beryllium and niobium samples may affect the analysis of the density inhomogeneities [74][4]. As we will discuss below, the largest effect would be at the level of a few parts in 10^7 for the difference in relative density.

The difference in surface area between niobium sample 1 and niobium sample 7A is about 9 cm^2. For a native oxide of 4 nm thickness, the volume difference is 3.6×10^{-6} cm^3. Since the native oxide has a density around 4.47 g/cm^3 (versus 8.57 g/cm^3) for niobium, there is a difference in the mass of this oxide of approximately 16 μg. The mass of sample 1 and sample 7A are both approximately 90 g. Therefore, the density difference due to the niobium oxide is approximately 16 μg/90 g $\sim$ 0.2 ppm. This is too small to be resolved by the experiment.

The effect of beryllium oxide is the same level as that of niobium. The maximum surface difference in the beryllium samples, which appears between samples 108 and

[4]The effects of native oxides were pointed out by Gill and the analysis presented here was originally done by Gill [74].

107/109, is approximately 22 cm^2. Therefore, the difference in mass of the native oxide (BeO with density of 3.01 g/cm^3 and thickness of 4 nm) is roughly 27 μg. The mass of sample 108 is roughly 95 g. Thus, the density difference is about 0.3 ppm.

5.4 Experimental Results

5.4.1 Measured apparent weights

Typical raw data of measured apparent weight in air and in the liquid is given in Tables 5.1 and 5.2, respectively. In these tables, the data are listed in the order of the measurements. Note that the measurement orders are symmetrical as described in Section 5.3.2. From these tables, one can see that the apparent weight measured in the liquid increased with time, while one in air did not show significant differences between the first and the last measurements.

The differences in the apparent weights, measured in the liquid, between the first and the last measurements are plotted in Figure 5.6, using the data in Table 5.2. For sample 102, the difference in the apparent weights between the first and the second measurements (marked as 102') and one between the second and the last measurements (marked as 102") are also plotted in the figure. As one can see in Table 5.2, the time interval between the first and the last measurements was the shortest in the following order: 104, 111, 103 and 102. The time intervals for the values of 102' and 102" are expected to be roughly the same as one of 111. Therefore, the plot indicates that the drift increased with time.

The drift seems mainly due to the change in the thermal expansion of the liquid ($\sim$

Sample	Apparent weight (g)
102	47.40982
111	48.20430
105	48.45437
105	48.45435
111	48.20431
102	47.40982

Table 5.1: Typical measured apparent weights of beryllium samples in air, listed in the order of measurements. Samples 102 and 111 were used as the standards.

Sample	Apparent weight (g)
102	29.14899
103	29.78991
111	29.63966
104	30.20586
102	29.14944
104	30.20636
111	29.64053
103	29.79113
102	29.15050

Table 5.2: Typical measured apparent weights of beryllium samples in the liquid, listed in the order of measurements. Sample 102 and 111 were used as the standards.

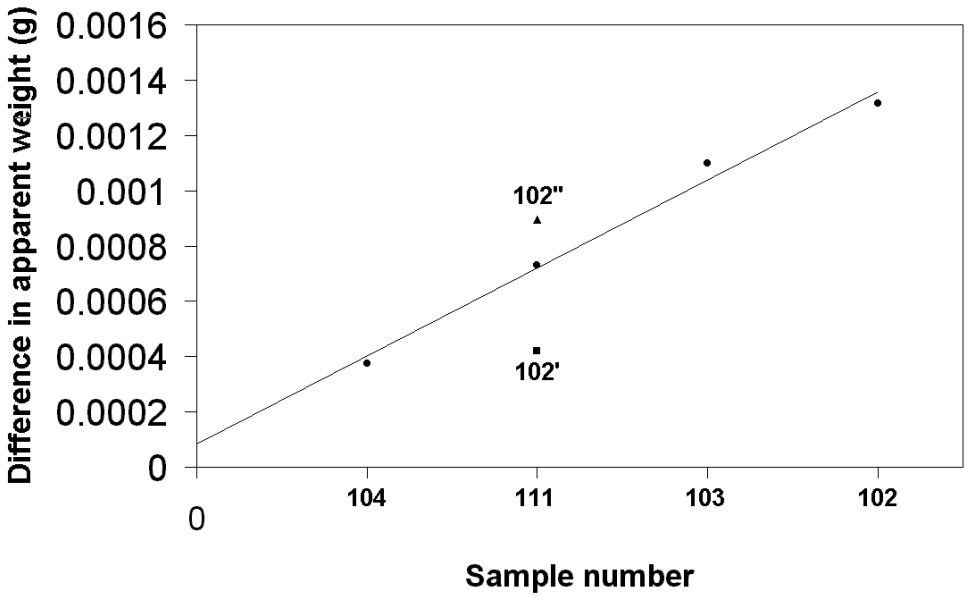

Figure 5.6: Drift of the apparent weights measured in the liquid. The x-axis corresponds to the time interval between the measurements (see text).

$10^{-3}/°C$); the temperature of the liquid seemed to increase during the measurements. This is probably because of the convective currents which arise in the liquid when the disk was moved to set the samples for the measurements. The maximum difference in the measured apparent weight of approximately 0.0014 g (Figure 5.6) can be due to a temperature change of roughly 0.04 $°C$.

5.4.2 Density variations

The relative densities were estimated from Equation (5.10). The drift can be eliminated by taking averages; for example, we took the average of the measured weights of the first and the last measurements of a standard in the liquid. The average value was used as m_{SL} in Equation (5.10). The change in the average value of m_{SA} between the sets of measurements was relatively small compared to one of m_{SL}. Therefore, we took the

average of m_{SA} over the sets of measurements and used it as the representative value for m_{SA}. The differences in apparent weight between a standard and a sample, such as $m_{SA} - m_{XA}$ and $m_{SL} - m_{XL}$ in Equation (5.10), were estimated by taking the average of the first and the last measurements of the sample and subtracting it from m_{SA} or m_{SL}, accordingly. The relative density between two standards was used to check the consistency between the sets of measurements.

Residual drift contributes to the uncertainty in the measurement of an apparent weight in the liquid, δm_{XL} and δm_{SL}, in Equation (5.11).

The results of the beryllium and the niobium samples are shown in Tables 5.3 and 5.4, respectively. The uncertainty in the measurements is 3 ppm for the beryllium and 5 ppm for the niobium samples. The maximum difference in the relative density between samples was approximately 240 ppm and 60 ppm for the beryllium and the niobium, respectively.

Several patterns may be observed in the density distributions. It was found that the beryllium rod had approximately a linear density distribution across the diameter (Figure 5.7). Also, it appeared that the niobium had a radial density gradient; samples 7A, 7B and 7C were of lower density than sample 6.

5.4.3 Fitting the results of the measurements

We attempted to fit the sampled data, using the least squares method, to various continuous spatial functions of density.

There were two data inputs: the positions of samples and the measured relative

Sample No.	$\Delta\rho/\rho_0 \pm 3ppm$ [ppm]
102	-21
103	-99
104	-25
105	90
106	74
107	-4
108	-35
109	-2
110	140
111	81
112	-37
113	-93
114	76

Table 5.3: Difference in density of the beryllium samples.

Sample No.	$\Delta\rho/\rho_0 \pm 5ppm$ [ppm]	Sample No.	$\Delta\rho/\rho_0 \pm 5ppm$ [ppm]
1	6	I	7
2	-7	II	11
3	3	III	2
4	17	IV	11
5	3	V	3
6	23		
7A	-36		
7B	-23		
7C	-39		
8	0	VIII	4
9	6	IX	14
10	4	X	14
11	7	XI	2
12	-1	XII	-3

Table 5.4: Difference in density of the niobium samples.

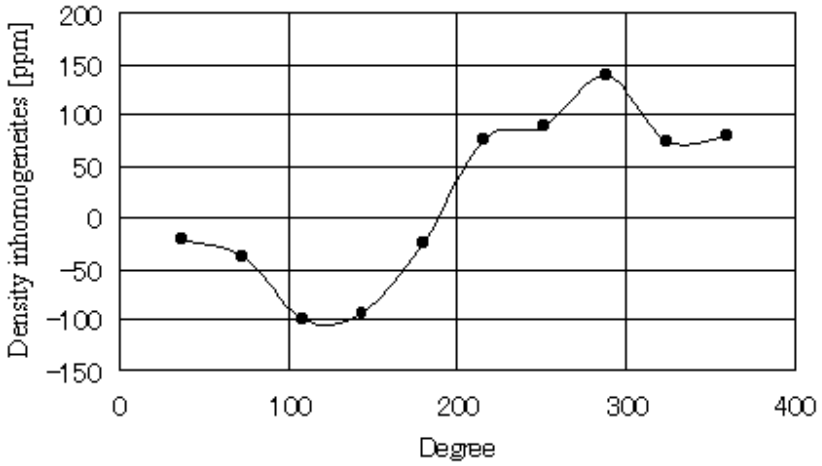

Figure 5.7: Angular density distribution in the beryllium samples. An approximate linear density variation across the diameter was observed.

densities. As for the former, the centres of mass of the samples were used.

The following functions fit best the beryllium and niobium data, respectively:

$$\begin{aligned}\rho_{Be}(x,y,z) &= \rho_{Be0}(1 + a_1x + a_2y + a_3z + a_4x^2 + a_5y^2 + a_6z^2 \\ &\quad + a_7xy + a_8yz + a_9zx + a_{10}xyz) \qquad (5.12)\end{aligned}$$

$$\rho_{Nb}(x,y,z) = \rho_{Nb0}(1 + b_1x + b_2x^2 + b_3y^2 + b_4xy + b_5yz + b_6zx) \qquad (5.13)$$

where ρ_{Be0} and ρ_{Nb0} are the density of a beryllium and niobium standard sample, respectively. The values for the fitted coefficients and their uncertainties are given in Tables 5.5 and 5.6. χ was 4.3 and 1.6 for the beryllium and the niobium, respectively[5].

These fitting functions are long and some of the coefficients are smaller than others. We attempted to simplify these functions. However, for instance in the case of the beryllium, a simplified function gave larger errors in the estimation of the disturbances

[5] χ is a square root of normalized chi-squared.

a_1	$(1.1 \pm 0.2) \times 10^{-6}$	mm^{-1}
a_2	$(-2.9 \pm 0.2) \times 10^{-6}$	mm^{-1}
a_3	$(-2.5 \pm 0.7) \times 10^{-7}$	mm^{-1}
a_4	$(1.5 \pm 0.9) \times 10^{-8}$	mm^{-2}
a_5	$(1.8 \pm 0.9) \times 10^{-8}$	mm^{-2}
a_6	$(1.4 \pm 0.7) \times 10^{-8}$	mm^{-2}
a_7	$(2.8 \pm 1.1 \times 10^{-8})$	mm^{-2}
a_8	$(3.6 \pm 3.2 \times 10^{-9})$	mm^{-2}
a_9	$(-6.4 \pm 3.2 \times 10^{-9})$	mm^{-2}
a_{10}	$(-2.6 \pm 2.1 \times 10^{-10})$	mm^{-3}

Table 5.5: Coefficients in function (5.12), which fits the beryllium results in Table 5.3.

b_1	$(2.4 \pm 1.6) \times 10^{-7}$	mm^{-1}
b_2	$(-2.4 \pm 0.3) \times 10^{-7}$	mm^{-2}
b_3	$(-2.2 \pm 0.3) \times 10^{-7}$	mm^{-2}
b_4	$(-1.3 \pm 1.2) \times 10^{-8}$	mm^{-2}
b_5	$(1.6 \pm 1.0) \times 10^{-9}$	mm^{-2}
b_6	$(-1.1 \pm 1.0) \times 10^{-9}$	mm^{-2}

Table 5.6: Coefficients in function (5.13), which fits the niobium results in Table 5.4.

in STEP signals by roughly 25 %. The analysis with simplified functions was presented in [57][6] and is represented in Appendix B.

5.4.4 Estimation of disturbances due to the density inhomogeneities

By substituting the fitting functions (Equations (5.12) and (5.13)) into Equation (3.9), we have estimated quadrupole moments of the STEP test masses. As discussed in Section 3.6.1, quadrupole moments would be the dominant terms, among multipole moments, to contribute the spurious differential acceleration of test masses with density inhomogeneities.

The integrals over the volume of STEP test masses have been calculated with Mathcad 8. The integrals were done over the volume of an outer test mass for the beryllium and an inner test mass for the niobium, respectively. The dimensions of these test masses are given in Table 3.2. The origins of the coordinate system was taken to be at the centre of mass of the test mass on the z-axis.

The internal machined edges and external chamfers on the test masses were not taken into consideration in this calculation for simplicity. However, it was checked that the effect of small change of the dimensions of test masses was not significant for the estimation of the difference in the quadrupole moments between a homogeneous and inhomogeneous test mass.

As a result, the dominant contribution to the differential acceleration was from q_{20}

[6]The results presented in the paper were found to be wrong following computational error; the disturbance should be roughly half and twice of the value presented for the beryllium and the niobium, respectively. The correction is given in Appendix B.

for both of the beryllium and niobium[7]. The extra quadrupole moments due to the density inhomogeneities (q_{20}/I_Z, see Section 3.4.1 for the definition) were found to be $(4.1 \pm 3.0) \times 10^{-6}$ and $(7.7 \pm 0.7) \times 10^{-6}$ for an outer test mass made from the beryllium rod and an inner test mass made from the niobium rod, respectively. Using Equation (3.16) (or (3.17)), we estimated that these quadrupole moments would produce a spurious acceleration of $\Delta a = (3.9 \pm 2.8) \times 10^{-19}\mathrm{m/s^2}$ and $(1.0 \pm 0.1) \times 10^{-19}\mathrm{m/s^2}$ for the beryllium outer test mass and the niobium inner test mass, respectively. We note that these spurious accelerations are equivalent to the gravitational susceptibilities of $\chi_a = (0.36 \pm 0.26)$ ppm and (0.10 ± 0.01) ppm for the beryllium and the niobium, respectively (see Sections 3.4.2 and 3.7 for the definition of χ_a).

As discussed in Section 3.7, we have followed the conservative STEP convention and assumed a 1-g point mass (helium bubble) at 250 mm from the centre of the test mass as a source mass to estimate the spurious acceleration.

5.5 Discussion

We found that the density inhomogeneities in our samples of HIPed beryllium and niobium would not significantly disturb the STEP experiment as STEP's target sensitivity is roughly $10^{-17}\mathrm{m/s^2}$ [38] and the target noise level, due to the gravitational multipole moments of test masses, is about $10^{-18}\mathrm{m/s^2}$. However, they could be significant in the following cases:

[7]Contributions from q_{21} and q_{22} were smaller than one from q_{20} by more than two orders of magnitude for both of the beryllium and niobium.

The dominant density variation observed in the beryllium samples did not contribute to the quadrupole moments directly because it was linear across the diameter; as discussed in Section 4.1, the quadratic density variations contribute more to the quadrupole moments than the linear density variations do. The maximum difference in the relative density of 240 ppm exceeds the allowable inhomogeneous level of 100 ppm for quadratic density variations, which we estimated in Section 4.1 (see Table 4.1).

We have investigated the niobium rod for an inner test mass. The density inhomogeneities in the niobium could be significant if they occur in a niobium rod used for an outer test mass. We have estimated the disturbance for an outer test mass by assuming that the niobium density variation we measured occurred in a rod used for the outer test mass. The result shows that the differential acceleration, due to the density inhomogeneities, would be $(2.4 \pm 0.2) \times 10^{-18}$ m/s^2 for the outer test mass.

To find a more homogeneous material, another HIPed beryllium rod (grade O30-H) was purchased from Brush Wellman Inc. This grade is a new product. Its chemical purity is the best of all their products and it is made using a specially produced spherical powder [92]. We are planning to prepare samples from it for measurements of density inhomogeneities, using the same hydrostatic weighing method at BIPM. In addition, we are planning to collaborate with Brush Wellman Inc. to find a way to fabricate more homogeneous HIPed beryllium.

Also, a larger niobium rod, from which an outer test mass can be made, was purchased from Wah Chang Company. The samples will be prepared from the larger rod

for density inhomogeneities measurements.

Engineer drawings of the dissection plan for the new rods are presented in Appendix C. We plan to use the same dissection scheme for beryllium and niobium. We plan to take more samples than the dissection presented in this chapter to increase the sampling points; the estimation of the disturbance is not limited by the uncertainty in measurements. Also, we plan to take cubic samples for the measurements of anisotropy of thermal expansion (see Section 7.8). We also plan to improve the capacity of the hydrostatic weighing device at BIPM by employing a larger bath [75].

5.6 Conclusions

The inhomogeneities of density in materials for the prototype STEP test masses, HIPed beryllium and niobium, have been determined by using the hydrostatic weighing method. Our analysis showed that the measured density inhomogeneities in those samples would be insignificant for the STEP experiment. However, the observed density inhomogeneities in HIPed beryllium could be significant if the same level of density inhomogeneities occurred as a quadratic variation. In addition, the density inhomogeneities observed in niobium could be significant for an outer test mass. Further studies to obtain more statistics and to find more homogeneous materials are planned.

Chapter 6

Thermal expansion and thermal distortion of materials for STEP test masses and the housing

In this chapter, we mainly discuss thermal distortion of HIPed beryllium. Firstly, we review thermal expansion of the materials to be used as the STEP test masses (niobium, HIPed beryllium and Pt/Ir alloy) and the housing in Section 6.1. We discuss the required level of uniformity of thermal expansion for the STEP test masses in Section 6.2. Then, we review thermal distortion of HIPed beryllium, which potentially has anisotropic thermal expansion, from existing literature. We view the origin of thermal distortion in HIPed beryllium in Section 6.3.1. We review the development and performance of specific grades of HIPed beryllium, which are considered to be used as STEP test masses, in Section 6.3.2. We describe the performance of the grade of our samples, I220-H, in Section 6.3.4, and discuss appropriate ways to prepare HIPed beryllium test masses for STEP in Section 6.3.5.

6.1 Summary of thermal expansion

Thermal expansions of materials to be used for the STEP test masses and the housing are necessary to decide on their machining dimensions. The required accuracy for this purpose is about 10%. Data of sufficient accuracy can be found in existing literature [76, 77] for all materials to be used except HIPed beryllium and Pt/Ir alloy. There is only one published value for HIPed beryllium (instrument grade O-50) at cryogenic temperature [78]. Thermal expansion of the specific HIPed beryllium to be used has to be studied for STEP. Thermal expansion data for Pt/Ir alloy at low temperature (lower than room temperature) was not found in literature.

Table 6.1 summarises thermal expansion data for various materials (HIPed beryllium, niobium, fused quartz and sapphire), which are to be used for the STEP test masses and the housing. In the table, thermal expansion is defined as follows:

$$\frac{\triangle L}{L} = \frac{L_{1.8} - L_{293}}{L_{293}} \tag{6.1}$$

where L_{293} and $L_{1.8}$ indicate the length of a specimen at temperatures 293 K and 1.8 K, respectively.

The materials listed in Table 6.1 can be classified into two groups: materials for STEP test masses and for the housing. The source of data in Table 6.1 and some notes for each material are described below.

Material (Specification)	Thermal expansion $\times 10^2$	Uncertainty (%)	To be used as
HIPed beryllium (O-50)	-0.1298	$\pm$ 1.5	OT, IT
Niobium	-0.147 (Recommended value)	$\pm < 3$	IT, Coating
90Pt-10Ir weight %	n.a.	n.a.	IT
Fused quartz (SRM739- vitreous silica)	0.0047 (Certificated value of NIST)	$\pm$ 1.2	Housing
Sapphire (Alumina, $\alpha - Al_2O_3$ single crystal)	-0.0635 (Recommended value)	$\pm < 1.9$	Housing

Table 6.1: Integrated thermal expansions (Equation (6.1)) of materials for STEP test masses and the housing. OT and IT stand for outer test mass and inner test mass, respectively. n.a. stands for not available.

6.1.1 STEP test-mass materials

As described in Section 2.4.1, HIPed beryllium, niobium and Pt/Ir alloy are the strongest candidate for STEP test masses. Especially, beryllium is expected to be a key element for a better sensitivity (Section 2.4.1).

HIPed beryllium

As mentioned previously, there is only one published value of thermal expansion of HIPed beryllium at cryogenic temperature[1]. Swenson [78] measured thermal expansion of HIPed beryllium (instrument grade O-50) purchased from Brush Wellman Inc. to 4

[1]There are some unpublished data. Swenson [78] mentions unpublished measurements of S-220F HIPed beryllium (1.06 % BeO), which shows systematic orientation difference below 150 K. Paquin [80] shows preliminary results of I70 HIPed beryllium, which we review in Section 6.3.2.

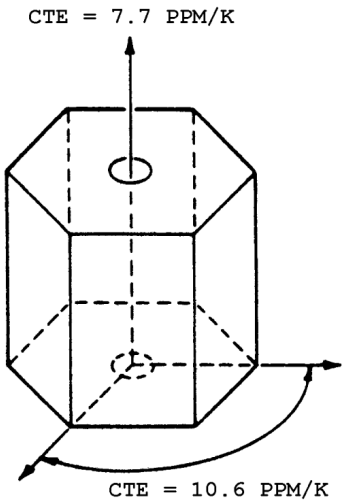

Figure 6.1: The coefficient of thermal expansion of single beryllium crystal is higher by roughly 35 % in the basal plane than the axial direction, at all temperatures. (This figure was quoted from [80])

K. His value is quoted in Table 6.1.

Single crystal beryllium is anisotropic because of its hexagonal close-packed structure. The coefficient of thermal expansion in the basal plane is roughly 35 % higher than it is in the axial direction, normal to the basal plane at all temperatures [76] (see Figure 6.1).

HIPed beryllium is supposed to have isotropic thermal expansion as it is made by packing beryllium powder. This is the reason why we chose HIPed beryllium. However, anisotropy and inhomogeneities of thermal expansion of HIPed beryllium have been reported (e.g. [79, 80]). We discuss this in detail in later sections of this chapter.

Niobium

There is a lot of literature on thermal expansion of niobium over a wide range of temperature. The value in Table 6.1 is taken from the recommended value in [76].

90Pt-10Ir alloy (weight percent)

Its thermal expansion is not well studied. Thermal expansion data at low temperature (lower than room temperature) was not found in literature.

Thermal expansion of a composite in which the thermal stresses are small (when it can be assumed that only uniform hydrostatic stresses exist in the phases) is given by Turner's formula [81]:

$$\alpha_c = \frac{\alpha_1 x_1 K_1 + \alpha_2 x_2 K_2 + \alpha_3 x_3 K_3 \cdots}{x_1 K_1 + x_2 K_2 + x_3 K_3 \cdots}, \tag{6.2}$$

where $\alpha_1, \alpha_2, \alpha_3 \cdots$, $x_1, x_2, x_3 \cdots$ and $K_1, K_2, K_3 \cdots$ are the thermal expansion coefficients, the volume fractions and bulk modulus of the composite materials of phases $1, 2, 3 \cdots$. By using this formula, the coefficient of thermal expansion of 90Pt-10Ir alloy is given as 8.5×10^{-6}/K at room temperature. This is in good agreement with the experimental data value of 8.7×10^{-6}/K [82].

However, we do not discuss Pt/Ir alloy in detail in this thesis as it is unclear if it would be used as a STEP test mass and it is not accessible at the moment as it is very expensive.

6.1.2 Materials for the STEP test-mass housing

Fused Quartz (Silica)

Vitreous silica [83] is used widely as a reference material because of the small thermal expansivity. The value in Table 6.1 is the certificated value of NIST (National Institute of Standards & Technology) for SRM 739 and taken from [83]. The thermal

expansion is isotropic, though crystalline quartz has hexagonal close-packed crystal structure and anisotropic thermal expansion. The thermal expansion of fused quartz varies with methods of preparation, particularly heat treatment.

Sapphire

Sapphire is available as a polycrystalline ceramic or in single crystal form [83]. The crystal structure is hexagonal close-packed and, therefore, it has anisotropic thermal expansion (like beryllium crystal and quartz). The values in Table 6.1 are the average thermal expansion of the crystal form and quoted from the recommended value in [84].

6.1.3 Summary and conclusions

We have discussed thermal expansions of materials for the STEP test masses and the housing. There is a certificated/a recommended value for all the materials except HIPed beryllium and Pt/Ir alloy. Thermal expansions of HIPed beryllium and Pt/Ir alloy have to be studied for STEP because of the lack of published data. In addition, HIPed beryllium potentially has anisotropic thermal expansion because of the crystal structure and it has been experimentally verified as we describe later. The presence of anisotropy and inhomogeneities of thermal expansion could induce thermal distortion. We discuss thermal distortion of HIPed beryllium in the later sections of this chapter.

6.2 Required level of uniformity of thermal expansion for the STEP test masses

The worst shape which can be imagined for the STEP test mass would be when the aspect ratio of the cylinder changes; this type of deformation directly affects the value of the quadrupole moments.

We consider a simple cylinder as a test mass for simplicity in the following argument[2]. For a simple cylinder (with radius of R and half-length of L), the quadrupole moments vanish when the aspect ratio is $R/L = 2/\sqrt{3}$ (see Section 4.1.1).

When the radius changes to $R + \delta$, the cylinder obtains quadrupole moments:

$$\left|\frac{\Delta q_{20}}{I_Z}\right| = \frac{1}{4}\sqrt{\frac{5}{\pi}}\frac{\delta}{R^4}(2R^3 + 5R^2\delta + 4R\delta^2 + \delta^3), \tag{6.3}$$

where I_Z is the moment of inertia (Equation (3.32)) of the cylinder with the aspect ratio (R/L). In order to make this less than 10^{-5} ($R = 50$mm, see Section 3.7 for the requirements on gravitational quadrupole moments):

$$\frac{\delta}{R} < 1.6 \times 10^{-5}. \tag{6.4}$$

For a test mass with a radius[3] of 50 mm, δ should be less than 0.8 μm. This requirement is consistent with the requirement on machining tolerance (< 1 μm) for STEP test masses (belted cylinders), which was derived by Lockerbie (Section 3.5).

The difference in thermal expansion in different direction, ΔTE, should be less than δ/R. The relative difference in thermal expansion, $\Delta TE/TE$, has to be less than

[2]Real STEP test masses are belted cylinders as described in Sections 2.4.1 and 3.5.
[3]This is roughly the radius of the outer STEP test masses (Section 3.5).

1.2 % for beryllium whose thermal expansion is -1.3×10^{-3} and 1.1% for the niobium whose thermal expansion is -1.5×10^{-3}, from room temperature to 1.8 K.

In general, this requirement may not be difficult to achieve. Data of thermal expansion have uncertainties less than ± 3 % (Table 6.1) in the absolute values. However, recommended values of thermal expansion were determined by considering data of different samples by various experiments by different people [76, 77, 83, 84].

Thermal expansion of niobium is supposed to be isotropic. Published results show no systematic difference in the thermal expansion (e.g. [76]). According to Valder [85] at Wah Chang Company, from which our niobium samples were purchased, thermal expansion of the niobium produced by the company should agree at least within 1% of the accepted value. However, as mentioned in Section 6.1, HIPed beryllium may have anisotropic thermal expansion because of the crystal structure of beryllium crystal. In fact, anisotropic properties of HIPed beryllium were reported (e.g. [79, 80, 86]), as mentioned before. Therefore, we focus on thermal distortion of HIPed beryllium.

6.3 Thermal distortion of HIPed beryllium

6.3.1 Origin of the thermal distortion

Beryllium products manufactured by consolidation of beryllium powder, such as HIPed beryllium and VHPed (vacuum hot-pressed) beryllium, could have anisotropic and/or inhomogeneous thermal expansion if the beryllium powder has anisotropy and it is not packed randomly. In other words, there would be no anisotropic nor inhomogeneous thermal expansion in those products if the particles are packed randomly. Here

inhomogeneities refer to spacial variations in anisotropy.

Beryllium powder made by milling is mainly cleaved along the basal plane (e.g. [79, 86, 87]). The particles tend to be flat and the faces correspond to the basal plane. If there are alignments of the basal plane in the product, it results in anisotropic thermal expansion.

Two causes for alignment of the basal plane are known [79, 80, 86]: (1) vibration of the consolidation bed; when the beryllium powder is put on the consolidation bed, it tends to align because of the vibration, (2) reorientation of the basal plane normal to the direction of the applied stress of compressing beryllium powder.

The anisotropy and inhomogeneity in thermal expansion result in thermal distortion. Mechanical anisotropy and thermal anisotropy, inhomogeneity and distortion were observed in beryllium products (e.g. [79, 80, 86]). As we will describe below, more thermal dimensionally stable (more thermally isotropic and homogeneous) beryllium products can be obtained by improving the powder morphology and consolidation conditions.

6.3.2 Development of beryllium products

Intensive studies have been done on thermal dimensional stability of HIPed beryllium mainly by those who have developed optical mirrors, as we will see below. Their results show that sufficiently thermally stable HIPed beryllium is feasible. We will discuss the development of the products and their performance in this section.

Studies in 1970 and 1980s

In 1970, Goggin and Moberly [79] showed that the anisotropy and inhomogeneities in crystal orientation in the products cause corresponding levels of thermal distortion. The crystalline anisotropy and inhomogeneities were measured by x-ray diffractometry. Here, anisotropy is defined as the amount of preferred orientation of the crystal planes, or departure from complete randomness and inhomogeneities refers to spacial variations in crystalline anisotropy [80]. They compared the measured intensity of peaks due to the crystalline planes in the scanned image with theoretical predictions for the isotropic case. Thermal distortion was measured interferometrically with samples polished to mirror finish.

Anisotropy in the thermal expansion coefficient can be estimated from measured x-ray diffraction intensities of the basal plane. In the mid-1980's, Paquin [80] investigated HIPed beryllium made by a new type of beryllium powder called impact ground powder. The amount of basal plane cleavage in the new powder was greatly reduced. He measured the basal plane preferred orientation in samples, prepared from various positions of a 9.5-inch mirror, by the x-ray diffraction method. Then, he calculated anisotropy in the thermal expansion coefficient by using the relationship between anisotropy in the thermal expansion coefficient and basal plane texture. He experimentally obtained the relationship by investigating many samples, using the x-ray diffraction method and measurements of difference in thermal expansion. The results show that the HIPed beryllium made from a impact ground powder of I-70 A was the most isotropic prod-

uct. The estimated anisotropy and inhomogeneities in the thermal expansion coefficient were 0.03 ppm/K and 0.02 ppm/K, respectively. This corresponds to roughly 0.2 % of the relative difference in thermal expansion coefficient at room temperature. For a 10 cm-long sample made from this HIPed beryllium, the difference in contraction from room temperature to 1.8 K would be roughly less than 0.2 μm. This is less than the requirement of 0.8 μm, we obtained in the previous section.

The consolidation of beryllium powders may depend on the geometry of the products. Also, the limited number of samples may not be representative. Paquin prepared HIPed beryllium billets, made by the same powder (I-70), with different geometries (see Table 6.2) for the x-ray diffraction measurements and thermal expansion measurements [80]. The results of the differences in thermal expansion from room temperature to 60 K showed little anisotropy[4]. Figure 6.3.2 shows one of the results[5](quoted from [80]).

According to the results of Paquin et al. [88], the most homogeneous and isotropic billets have an aspect ratio of 1 : 1. In billets with high aspect ratio, such as long cylinders, shrinkage during the HIPing process is dominant in the radial direction and, therefore, the basal planes tend to align parallel to the circumferential surface. For billets with a low aspect ratio, such as disks, the shrinkage is dominant in the axial direction, therefore, the basal planes tend to be parallel to the plane of the circular top

[4]Full results are not published.

[5]This is a preliminary result presented in [80]. In [89], it is described that the full results of measurement of differences in thermal expansion were presented at the annual meeting of the Optical Society of America in 1986, but data is not presented in the reference.

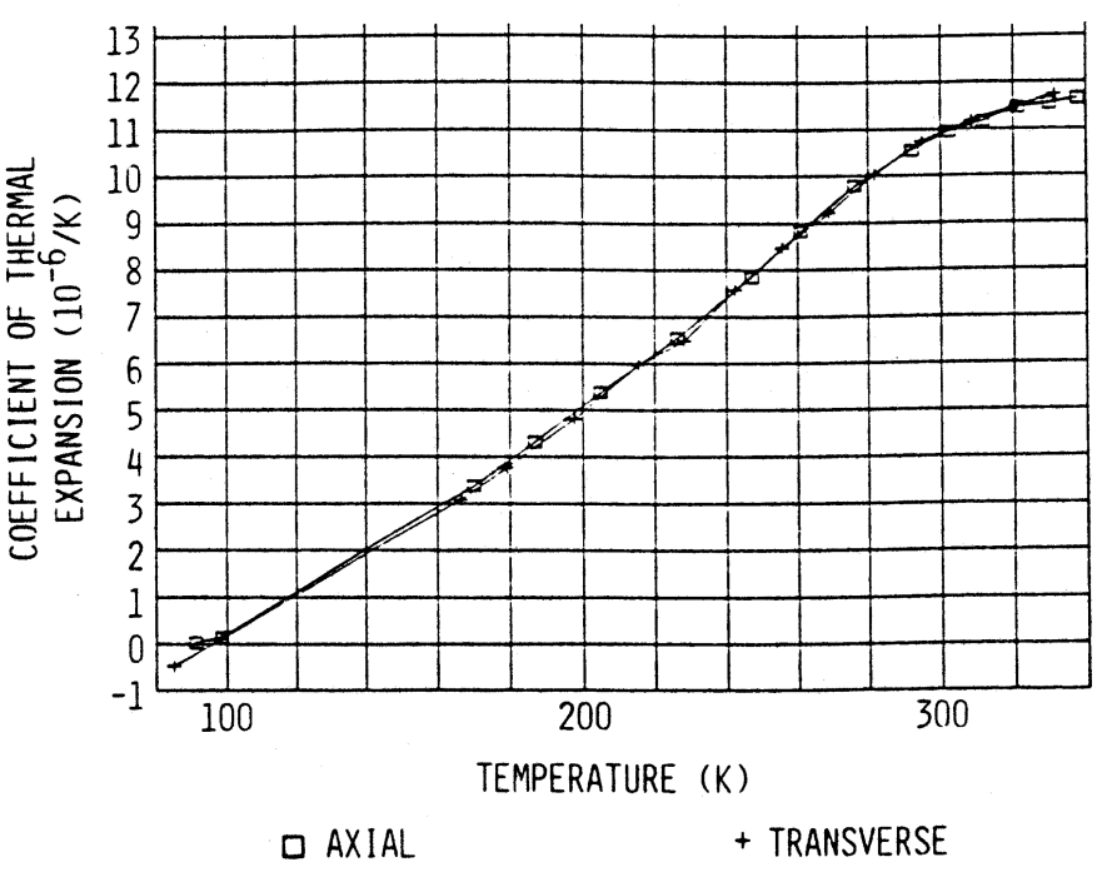

Figure 6.2: Directional difference in thermal expansion of HIPed beryllium. A result of measurements by Paquin et al. [80] showed little difference in thermal expansion along the transverse and axial direction of HIPed beryllium (I-70) billets.

Shape	Diameter/Length [inches]
Rod	1/8
Plate	8/1
Cylinder	5/5
Disk	6/1 (rigid Mandrel)
Disk	6/1 (Soft Can)

Table 6.2: Geometries of HIPed beryllium billets prepared for the x-ray diffraction measurement and differential thermal expansion measurement by Paquin et al. [80]. The cylinder has roughly the same size as the billet for STEP outer test masses.

and bottom surfaces.

Recent studies

More recently, the fabrication methods of beryllium products have been improved further. Paquin et al. [90] successfully produced large mirrors that are some of the most thermally and dimensionally stable, regardless of materials, by developing the novel fabrication method. They achieved a thermal distortion, from room temperature to 4 k, of 0.63 μm peak-to-valley for a HIPed beryllium mirror, made of I70 powder, with an outer diameter of 50 cm, an inner diameter of 10 cm and a thickness of 8.5 cm. This may be converted into differential thermal expansion by taking the ratio of 0.63 μm/8.5 cm, 0.42 ppm. The relative difference in thermal expansion is therefore 0.03 %. The fabrication method is summarized in the next section.

Also, Swenson reported that the data of thermal expansion coefficient of six samples, from one billet of HIPed beryllium (O-50) (no record of orientation of the samples), were consistent to within $\pm$ 0.3 % from 100 to 300 K and $\pm$1.5% below 80 K [78].

The HIPed beryllium of the instrument grade of I220, which was also investigated

for the application to large mirrors [90], is expected to be more homogeneous than I70-H (H stands for HIPed products) [88]. I220-H is our samples' grade. We discuss this grade in Section 6.3.4.

The best beryllium products available most recently are made from spherical powder [87, 91, 92]. Measurements of the coefficient of thermal expansion of a grade O30-H made of a spherical powder by HIPing showed no difference between three orthogonal directions over the temperature range from 5 to 65 $^{\circ}C$. The precision of the measurement was $\pm$ 0.1 ppm/K [91].

In summary, anisotropy and inhomogeneities of thermal expansion is well studied mainly for optical mirrors. Sufficiently isotropic and homogeneous HIPed beryllium products for STEP are available.

6.3.3 Fabrication of thermally stable HIPed beryllium

Paquin et al. conclude that the fabrication process to yield high quality beryllium products, with isotropic and homogeneous properties, made of impact ground powders is as follows [90]:

- Start with clean, fine grained, moderate to low oxide, impact ground beryllium powder,
- Consolidate by HIP,
- Use progressive machining for all steps,
- Acid etch after every machining and every rough grinding step,

- Anneal at 785 $^{\circ}C$ after HIP and every rough machining step and
- Thermally cycle after the last machining step and after every grind and polish step.

Brush Wellman Inc. uses this fabrication method for this type of beryllium products [93]. According to Parsonage at Brush Wellman Inc., the billet of I220-H from which our samples were prepared should have been fabricated with this method by considering the details and the fabrication date [93].

Large mirrors have complicated shapes like a honeycomb; it would be easier to fabricate thermally stable products of simpler shapes, such as cylinders, from which STEP test masses are to be machined.

6.3.4 Performance of our samples, I220-H

The samples used for the measurements of the density inhomogeneities (Chapter 5) were the grade of I220-H purchased from Brush Wellman Inc. This grade was investigated for the application of large optical mirrors. The stable performance was observed for a large mirror (outer diameter 1.12 m, inner diameter 4.6 cm and thickness 13 cm) of I220 fabricated by the same process described in Section 6.3.3. As mentioned before, Brush Wellman Inc. followed the same fabrication for the grade of I220-H [93], therefore, this grade should be highly isotropic and homogeneous. Paquin said that it was expected to be more homogeneous than I70-H and similar in anisotropy because of the finer particle size of the I220 powder [88].

Therefore, there should be no problem with thermal distortion of STEP test masses made by I220-H, if the post machining processes described in Section 6.3.3 are followed.

The samples used for the measurements of density inhomogeneities (see Chapter 5) were dissected by Speedring (AXSYS Technologies). There are no records of whether they were stress relieved after the machining [94].

The rod, from which the samples were made, was obtained from a stock at Speedring. There is no record of the original HIPed size of the rod.

6.3.5 Preparation of STEP test masses

By considering these aspects described above, the best way to fabricate HIPed beryllium STEP test masses with sufficient thermal dimensional stability may be as follows:

1. Purchase a HIPed beryllium cylinder made of a impact ground powder such as I70 and I220 (preferably, the aspect ratio of the cylinder is 1 : 1),

2. Machine the cylinder to the STEP test mass shape by following the post machining process described in Section 6.3.3.

Test masses prepared in this way would have sufficient thermal dimensional stability for the application.

Even if test masses are prepared in this way, it is still important to check their thermal dimensional stability. As described in Section 6.3, several methods have been used to check thermal dimensional stability of beryllium. Anisotropy and inhomogeneity in the thermal expansion have been checked by measuring differences in the

thermal expansion and by measuring the preferred orientation of basal plane using x-ray diffraction methods. Also, the thermal distortions have been measured by using the cryogenic holographic methods [95].

For STEP test masses, the most concerned thermal dimensional instability is the change of the aspect ratio (Section 6.2). This change can directly be checked by measuring anisotropy in thermal expansion. We have developed a device to measure differential thermal expansion using a capacitive sensing method. Capacitive sensing is one of the most sensitive methods to measure thermal expansion. Also, unlike optical methods, capacitive sensing methods can easily be applied to cryogenic measurements and do not require special surface preparation. The x-ray diffraction methods can also be used to check anisotropy in thermal expansion. However, the x-ray diffraction methods can only examine the surface of samples (the x-ray penetration depth (Cu K_α) is about 2.5 mm for beryllium) and may not be applicable for denser test masses (such as Pt/Ir alloy and niobium).

The device that we have developed was particulary designed to measure differences in thermal expansion between available HIPed beryllium samples, which were used for the density inhomogeneity measurements. We have developed a mounting system that allows to fix samples without machining them. This device and mounting system could be developed for the measurements of anisotropic thermal expansion of STEP test masses in their final shapes. We will describe the device and preliminary results in Chapter 7.

The usage of the products made from spherical powder, such as O30-H, may be another option, though it will not be necessary as the thermal dimensional stability of products of impact ground powder is sufficient. The stress involved during the machining may not be significant for the products made from spherical powder; the fabrication process may be simpler than the one for the products made from impact ground powder.

Choice of grades of HIPed beryllium for the STEP test masses has to be done by considering both properties of density homogeneity and thermal dimensional stability.

6.4 Conclusions

We have summarised thermal expansion of materials to be used for the STEP test masses and the housing. Recommended values or certificated values were found in literature for all of the materials, except HIPed beryllium and Pt/Ir alloy, which are the strongest candidates as STEP test masses.

We have discussed the thermal dimensional stability of HIPed beryllium, which potentially has anisotropic thermal expansion. The achievable stability of HIPed beryllium is much higher than the required level of thermal distortion for STEP. HIPed beryllium made of impact ground powder would be sufficient for STEP test masses as regards the thermal dimensional stability. We have discussed ways to prepare HIPed beryllium test masses for STEP.

However, it is still important to experimentally check the thermal dimensional sta-

bility of specific materials prepared for STEP test masses. For example, residual stress in the particular materials may be significant. The most concerned thermal dimensional instability in STEP test masses is the change of the aspect ratio. This change can be checked by measuring the differences in thermal expansion between their axial and radial directions. We have developed a device to measure differential thermal expansion, which can be developed for this purpose. We will describe this device in the next chapter.

Chapter 7

Measurements of differential thermal expansion

7.1 Introduction

As discussed in Section 6.2, thermal distortion of STEP test masses could produce extra gravitational multipole moments and disturb the STEP experiment. Among the materials suggested for the STEP test masses, HIPed beryllium is probably most likely to have a significant level of thermal distortion because of the hexagonal crystal structure. As we reviewed in Section 6.3, the studies of thermal dimensional stability of HIPed beryllium showed that nominal thermal distortions of the specific grades, which are intended to be used as the STEP test masses, would be small enough. However, it is still important to check the thermal dimensional stability of the specific materials prepared for STEP. For example, residual stress in the particular materials may be significant. The most concerned thermal dimensional instability in STEP test masses is the change of the aspect ratio. This change can be checked by measuring the differences in thermal expansion between their axial and radial directions. We have

developed a device to measure differential thermal expansion, which can be developed for this purpose.

The device is designed to measure differences in thermal expansion between samples by using the three-terminal parallel-plate capacitor method. A mounting system has been developed to mount samples stably without machining the samples. The device is designed particularly for the HIPed beryllium samples used for the density inhomogeneities measurements (Chapter 5).

The experiment has been cooled down to near the liquid nitrogen temperature (approximately 77 K). It is ideal to measure the differential thermal expansion by cooling down to liquid helium temperature as STEP test masses are to be operated at 1.8 K. However, the coefficient of thermal expansion is very small at the cryogenic temperatures, therefore, the change of the results of differential thermal expansion under the liquid nitrogen temperature would be insignificant. Augason et al. reported that virtually no change was observed between the 77.5 K and the 4.4 K measurements of thermal distortion of a HIPed beryllium (I-70) mirror [96].

We will describe the formulae to calculate differential thermal expansions from measured capacitances in Section 7.3, and review the device in Section 7.4, the mounting system in Section 7.5 and the experimental results in Section 7.7.

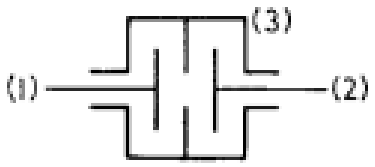

Figure 7.1: A schematic view of three-terminal capacitance (quoted from [97]). Terminals (1) and (2) are electrodes to form a capacitor and terminal 3 is the ground shield of the capacitor.

7.2 Three-terminal parallel-plate capacitor method

The three-terminal parallel-plate capacitor method is one of the most sensitive ways to measure thermal expansion. This method was originally applied for thermal expansion measurements by White [97].

Experiments of thermal expansion, which use this method, are usually designed so that the changes of the length of a sample relative to a reference change the gap between two electrodes (terminals (1) and (2) in Figure 7.1) (see for example [97]). The change of the gap, which is roughly proportional to $1/C$ (C is the capacitance formed by the two electrodes), is measured by a capacitance bridge.

In the design of this type of experiment, it is important to make the change of the capacitance insensitive to stray capacitances in the surroundings. A terminal (terminal (3) in Figure 7.1) connected to the bridge ground surrounds the capacitance to shield it from stray capacitances.

A diagram of an equivalent circuit for a three-terminal capacitance bridge, with

an ideal transformer, is shown in Figure 7.2[1]. The stray capacitances (C_{s1} and C_{s2}) are connected to the bridge ground. Current flow from Lo to the bridge ground is detected. If the transformer is ideal and the impedance of the transformer is zero, the voltages applied to the capacitances (C_X and C_{Ref}) are independent of stray capacitances. Therefore, the voltages applied to the capacitances (C_X and C_{Ref}) are identical to the voltages induced in the transformer winding, as drawn in Figure 7.2. The balance condition of the capacitance bridge is:

$$\frac{C_X}{C_{Ref}} = \frac{V_{Ref}}{V_X} \tag{7.1}$$

The detector is insensitive to the stray capacitances.

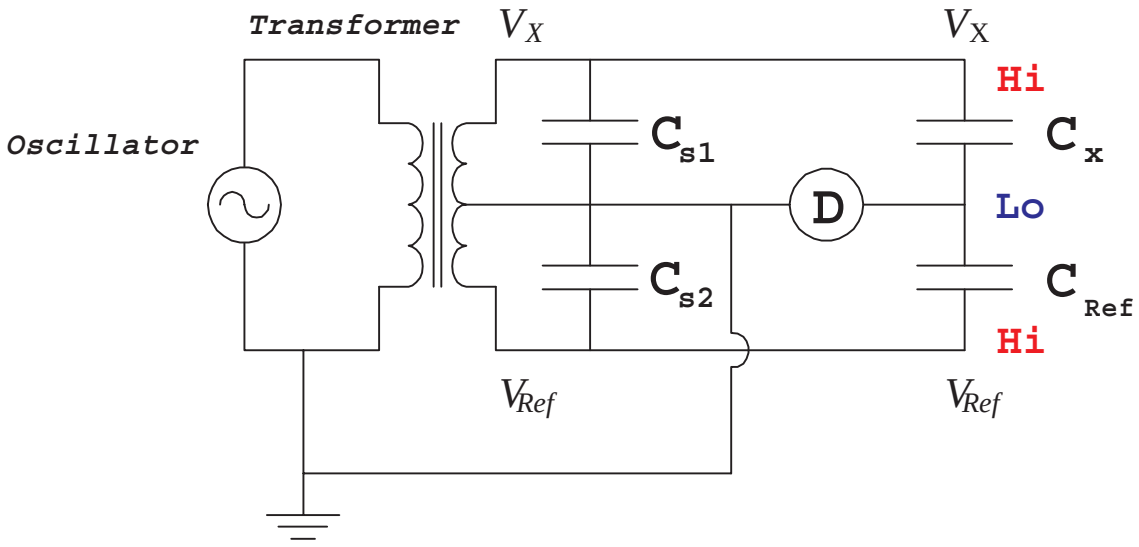

Figure 7.2: An equivalent circuit for a three-terminal capacitance bridge. It is assumed that the transformer is ideal (see text). The electrodes of low voltage and high voltage are indicated as Lo and Hi, respectively. Ⓓ indicates the detector.

The error in the reference capacitor (C_{Ref}) is given by $\omega_V^2 l_T C_T$, where $\omega_V = 2\pi f_V$.

[1]Figure 7.2 was provided by Chang [98] and was slightly modified by the author.

f_V and l_T are the frequency of the supplied voltage and the transformer leakage inductance, respectively [99]. $C_T = C_{Ref} + C_{GT} + C_{GN}$, where C_{GT} and C_{GN} are the transformer winding capacitance and stray capacitance, respectively. For our measurements with a capacitance bridge (General Radio Company, Type 1615-A), the error in the reference capacitance is 2.4 ppm ($\omega_V \sim 2\pi \times 5kHz$[rad/s], $l_T \sim 4\mu H$ [99], $C_{Ref} \sim 0.5pF$, $C_{GT} \sim 500pF$ [99] and $C_{GN} \sim 100pF$). This error is negligible as it corresponds to approximately 1.2 aF and the resolution of the capacitance bridge is 10 aF. In addition, the error in the absolute value of the capacitances is not important for the measurement of differential thermal expansion (see Sections 7.3.4 and 7.7.3).

A schematic view of the three-terminal configuration of our capacitance cell (see Section 7.4 for further details) for the measurements of differential thermal expansion is shown in Figure 7.3. All the conductors of the capacitance cell, except the electrodes (Hi) and samples (Lo), are connected to the bridge ground.

7.3 Calculations of differential thermal expansion

7.3.1 Thermal expansion

Assume a capacitance whose gap at a temperature T is given by the difference in the length of a reference, L_R, and a sample, L_S:

$$d = L_R - L_S. \tag{7.2}$$

The gap at another temperature T' can be given as follows:

$$d' = L_R(1 + TE_R) - L_S(1 + TE_S) \tag{7.3}$$

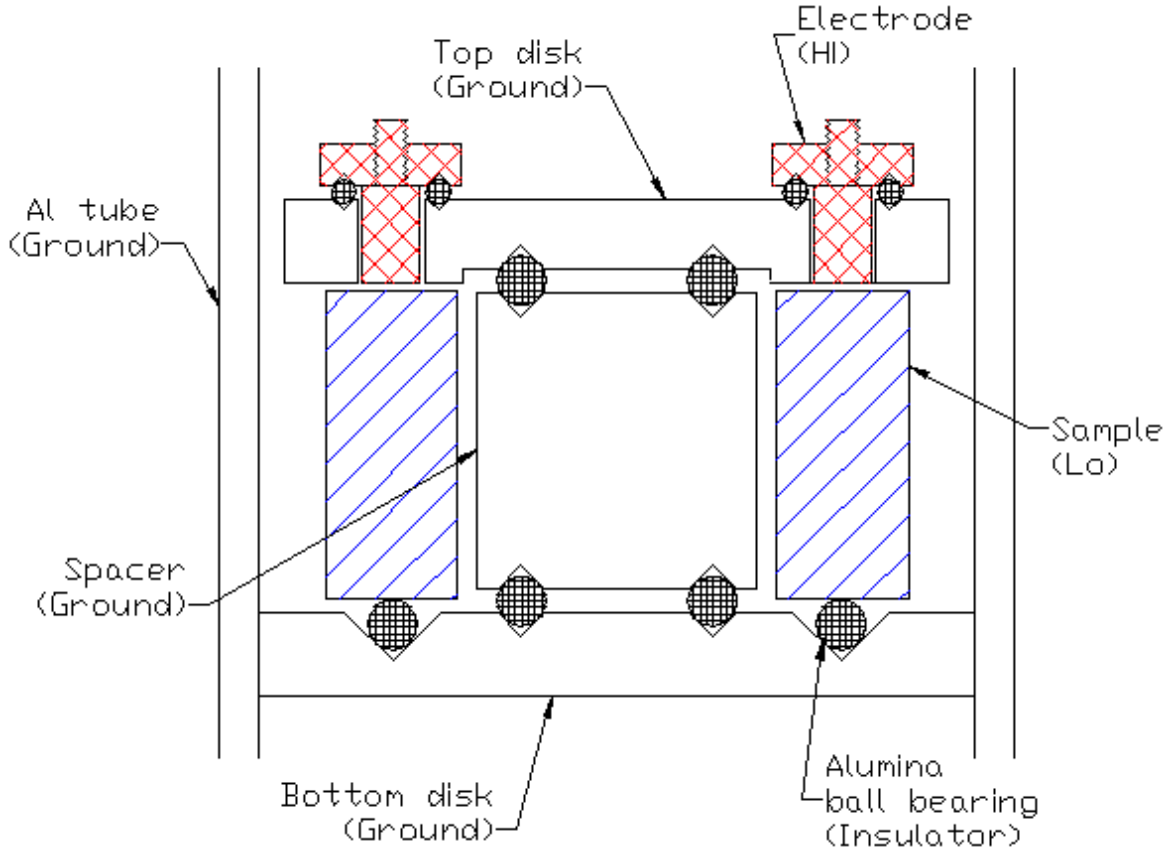

Figure 7.3: A schematic cross section of our capacitance cell, showing its three-terminal configuration. The high and low voltages were supplied to the electrodes (meshed area) and the samples (slashed area), respectively. Insulators were filled with grid lines. The other parts (the top and bottom disks, the spacer and the aluminium tube) were connected to the bridge ground.

where TE_R and TE_S are the integrated thermal expansion of the reference and the sample over the temperature change, respectively.

The change in the gap from the temperature T to T' can be written as follows:

$$\Delta d = d' - d \tag{7.4}$$

$$= L_R TE_R - L_S TE_S. \tag{7.5}$$

From this equation, the thermal expansion of the sample is given as follows:

$$TE_S = \frac{L_R TE_R - \Delta d}{L_S}. \tag{7.6}$$

The value of TE_R can be obtained from literature. The values of L_R and L_S can be obtained by measurements using a micrometer. The value of Δd is obtained from the capacitance measurements as we will discuss in Section 7.3.4.

7.3.2 Differential thermal expansion

By employing two capacitances such as those described in the previous section, the difference in thermal expansion between two samples can be obtained as follows by using Equation (7.6). Here, we assume that the same reference is used for both of the samples as a common reference:

$$\Delta TE_{2,1} = TE_{S2} - TE_{S1} \tag{7.7}$$

$$= \frac{1}{L_{S2}}(L_R TE_R - \Delta d_2) - \frac{1}{L_{S1}}(L_R TE_R - \Delta d_1) \tag{7.8}$$

$$\simeq \frac{\Delta d_1 - \Delta d_2}{L_S}, \tag{7.9}$$

where TE_{S1} and TE_{S2} are the thermal expansions of sample 1 and sample 2, respectively. L_{S1} and L_{S2} are the lengths of sample 1 and sample 2, respectively. It is assumed that $L_{S1} \simeq L_{S2} = L_S$ in Equation (7.9). This assumption is acceptable for our measurements; the difference in the length of our samples is within 8 μm and its contribution to the differential thermal expansion should be less than 0.02 % of thermal expansion of beryllium. This is negligible as we want to measure the differential thermal expansion of about 1.2 % (Section 6.2).

7.3.3 Capacitance

A capacitor usually has a guard ring around an electrode to reduce the effects of electrical field distortion at the edges of the electrodes (Figure 7.4). Maxwell derived a formula to calculate a capacitance of circular electrodes (of radius R_{Ele}) with a guard ring [100]:

$$C = \frac{\epsilon \pi R_{Ele}^2}{d} + \frac{\epsilon \pi R_{Ele} \omega}{d + 0.22\omega} \left(1 + \frac{\omega}{2R_{Ele}}\right), \tag{7.10}$$

where ϵ is the permittivity and ω is the width of the gap between the electrode and the guard-ring (see Figure 7.4). The electrodes and the guard-ring are assumed to be thick compared with ω. The first term of the right-hand side of Equation (7.10) is an ideal parallel-plate capacitance and the higher terms are the correction for the edge effect.

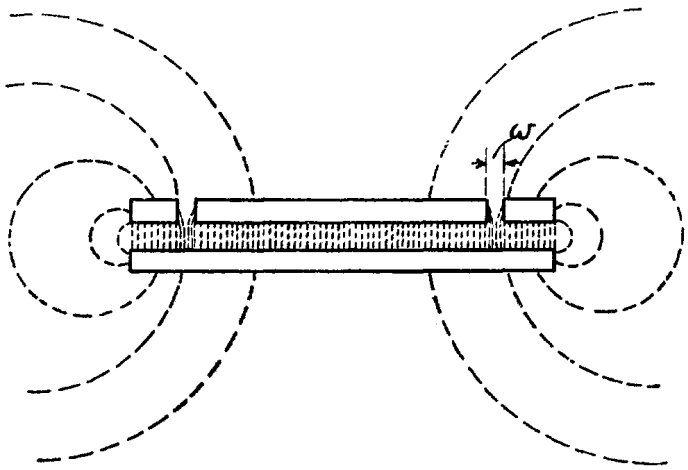

Figure 7.4: A schematic section of circular electrodes with a guard-ring (quoted from [100]). The dashed lines show the electric field. ω is the gap between the electrode and the guard ring.

7.3.4 Change in the gap

The gap is obtained by solving Equation (7.10) with d. From Equation (7.10),

$$d \cong \frac{\epsilon\pi R_{Ele}^2}{C}\left\{1+\frac{\omega}{R_{Ele}}\left(1+\frac{\omega}{2R_{Ele}}\right)\left(1-\frac{0.22\omega}{d}\right)\right\} \tag{7.11}$$

$$= \frac{\epsilon\pi R_{Ele}^2}{C}\left\{1+\frac{\omega}{R_{Ele}}+\frac{1}{2}\left(\frac{\omega}{R_{Ele}}\right)^2\right\}-\delta_d \tag{7.12}$$

where

$$\delta_d = \frac{\epsilon\pi R_{Ele}^2}{C}\cdot\frac{\omega}{R_{Ele}}\left(1+\frac{\omega}{2R_{Ele}}\right)\cdot\frac{0.22\omega}{d} \tag{7.13}$$

The uncertainty in the absolute value of the gap (d) is not crucial for the estimation of differential thermal expansion[2]. For our experiment, δ_d/d is as small as 1.3×10^{-3} (ω = 0.15 mm and R_{Ele} = 3.9 mm). This would contribute to the uncertainty of differential thermal expansion by roughly 0.1 % of the differential thermal expansion,

[2]The uncertainty of the gap, δd, contributes to the uncertainty of differential thermal expansion as $\sim(\Delta TE/TE)(\delta d/d)$.

$\Delta TE/TE$. Therefore, the effect of δ_d is negligible for the estimation of differential thermal expansion.

The difference in the change of the gap between samples in Equation (7.9) becomes:

$$\begin{aligned}\Delta d_1 - \Delta d_2 &= \left\{\frac{\epsilon\pi R'^2_{Ele1}}{C'_1}(1+o'_1) - \frac{\epsilon\pi R^2_{Ele1}}{C_1}(1+o_1)\right\} \\ &\quad - \left\{\frac{\epsilon\pi R'^2_{Ele2}}{C'_2}(1+o'_2) - \frac{\epsilon\pi R^2_{Ele2}}{C_2}(1+o_2)\right\} \qquad (7.14) \\ &\simeq \epsilon\pi R^2_{Ele}\left[\left\{\frac{(1+TE_{R_{Ele}})^2}{C'_1} - \frac{1}{C_1}\right\}\right. \\ &\quad \left. - \left\{\frac{(1+TE_{R_{Ele}})^2}{C'_2} - \frac{1}{C_2}\right\}\right](1+o), \qquad (7.15)\end{aligned}$$

where

$$o = \frac{\omega}{R_{Ele}} + \frac{1}{2}\left(\frac{\omega}{R_{Ele}}\right)^2 \qquad (7.16)$$

Where $TE_{R_{Ele}}$ is the thermal expansion of the electrodes. In the above equations, a dash ($'$) was used for the quantities at temperature T', and the subscripts 1 and 2 indicate sample 1 and 2 respectively. For our experiment, o is approximately 0.04 and can be ignored. From this equation and Equation (7.9),

$$\Delta TE_{2,1} = \frac{\epsilon\pi R^2_{Ele}}{L_S}\left[\left\{\frac{(1+TE_{R_{Ele}})^2}{C'_1} - \frac{1}{C_1}\right\} - \left\{\frac{(1+TE_{R_{Ele}})^2}{C'_2} - \frac{1}{C_2}\right\}\right] \qquad (7.17)$$

This equation was used to obtain the results presented in Section 7.7.4.

In the above discussion, we have assumed that the apparatus is identical for both of the samples. However, in reality, they are deferent. The maximum gap difference of roughly 0.1 mm (about 10 % of the gap) was observed between different positions in our device. The possible origins of the difference are, for example, the difference

in the depth of the tetrahedron-shaped blind holes, the length of the electrodes and the height of the alumina balls, and tilts of the top disk (see Section 7.4 for a detailed description of the device). In the worst case (when the difference is due to a titanium part, whose thermal expansion is the largest among other parts), 10 % of gap difference can produce a spurious signal of about 0.25 % in $\Delta TE/TE$. This systematic error was taken into account in the final results presented in Section 7.7.4. We have rotated the samples and compared the result with one before the rotation. We observed no significant differences between them (Section 7.7.4).

7.4 Experimental set-up

7.4.1 Overview

As described in Section 7.2, the three-terminal parallel-plate capacitance method was used to measure the differential thermal expansions. The device is able to measure differential thermal expansion of three samples. The device mainly comprises of three parts: the capacitance cell (Figure 7.5), glass dewars and a capacitance bridge (Figure 7.6).

The capacitance cell mainly comprises of an aluminium tube, two titanium disks (the diameter and the thickness are approximately 80 mm and 10 mm, respectively.), three circular electrodes (of diameter 7.8 mm) made of titanium, one titanium spacer, three samples and a mounting system for each sample. One of the disks (bottom disk) is attached to the aluminium tube (Figure 7.5). The spacer is kinematically mounted at the middle of the bottom disk and three samples are mounted on the bottom disk

around the spacer (Figure 7.7) by using the mounting system described in Section 7.5.3. The other disk (top disk) is kinematically mounted on the spacer and three electrodes are kinematically mounted on the top disk (Figures 7.8 and 7.13). The height of the samples is shorter than that of the spacer to form a gap of approximately 1 mm between the top disk and the samples. Therefore, the spacer acts as the common reference for the three samples. Each electrode is aligned to one sample to form a capacitor (Figure 7.5).

As described in Section 7.2, high voltage (100 V, peak to peak) was supplied to the electrodes and the low voltage was supplied to the samples with coaxial cables and wires (see Section 7.4.2). All the other conductors in the capacitance cell, such as the aluminium tube, the top and bottom disks and the spacer, were connected to the ground of the capacitance bridge to achieve the three-terminal set-up. They were electrically isolated from the high and low voltage electrodes by insulators of alumina and macor (see Section 7.5.3 for details). The capacitance cell was wrapped by an aluminium sheet to shield it from external electrical fields and connected to the bridge ground (Figure 7.9).

The capacitance cell was attached to a cryostat insert (Figure 7.9) and placed in the inner glass dewar (Figure 7.6). Before the measurements, the air in the inner dewar was pumped out by a vacuum pump and replaced by helium gas. Liquid nitrogen was supplied in the outer dewar to cool the capacitance cell. The capacitances were manually measured at temperatures of approximately 20 $^{\circ}C$ (293 K) and 77 K by

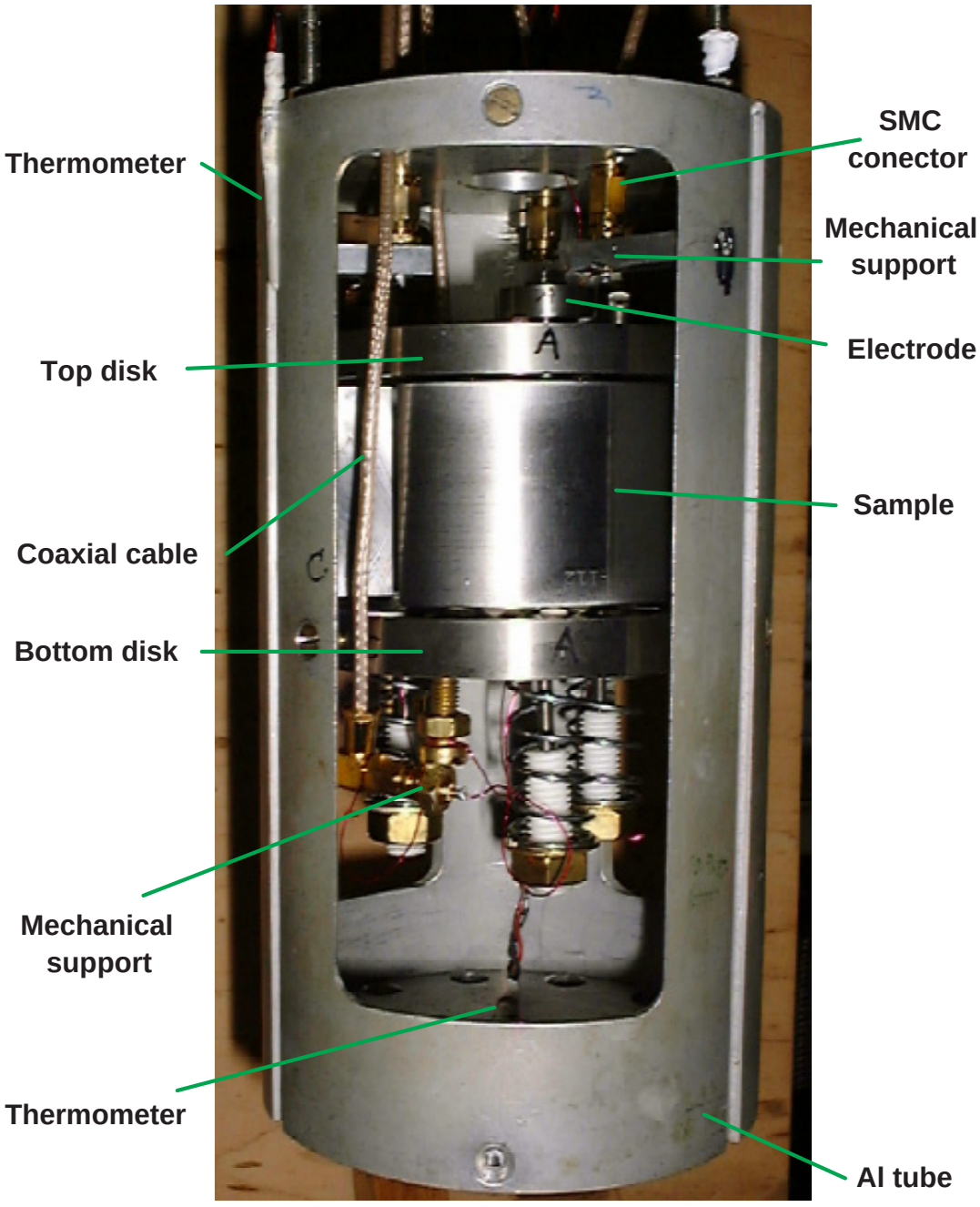

Figure 7.5: A photograph of the capacitance cell.

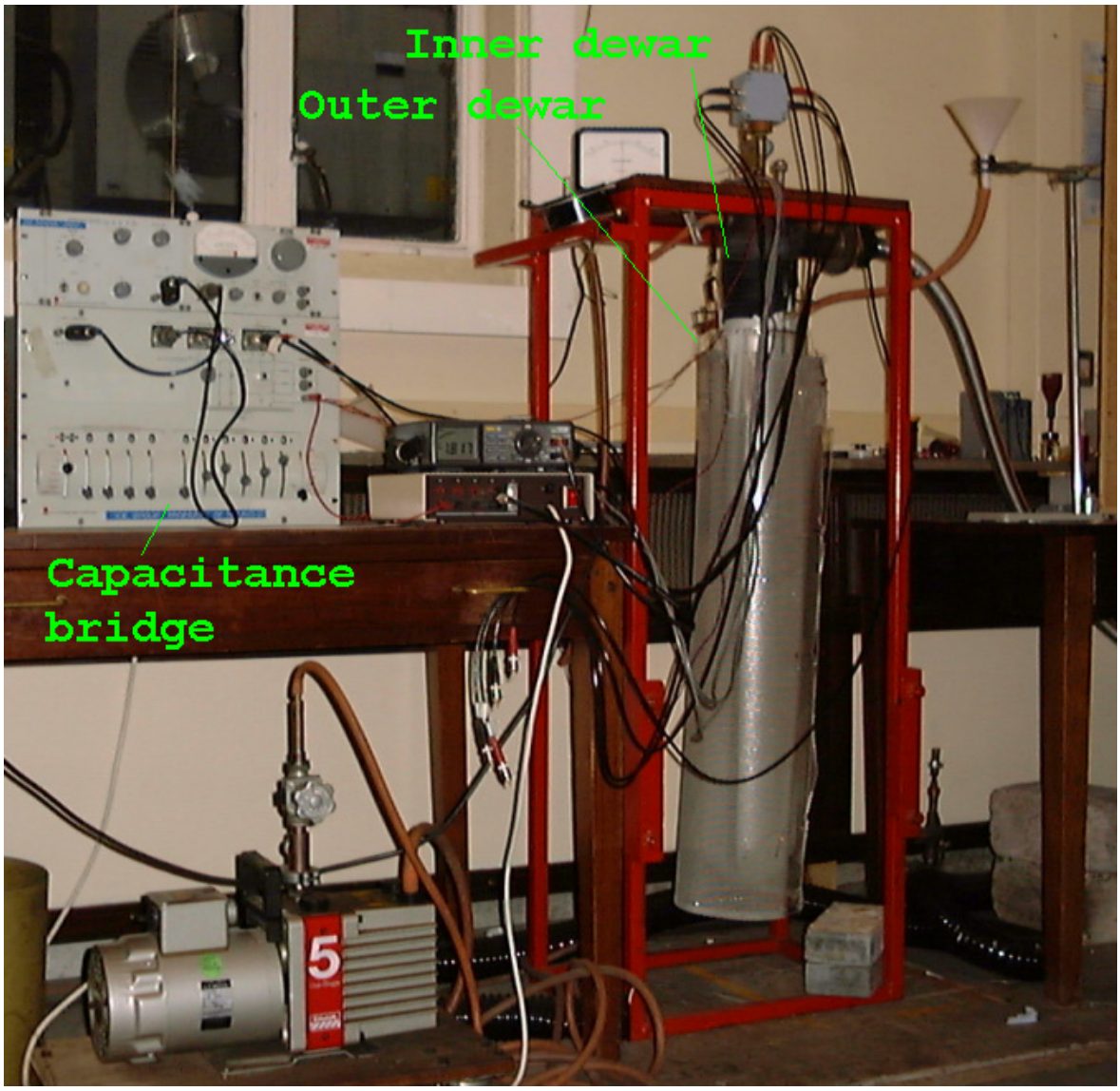

Figure 7.6: A photograph of the dewars and the capacitance bridge

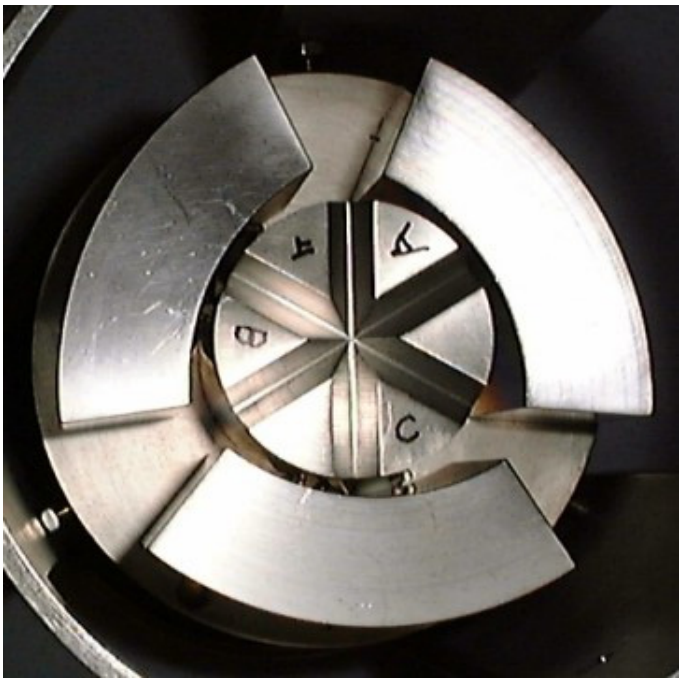

Figure 7.7: The titanium spacer (in the middle) and three samples are mounted on the bottom disk.

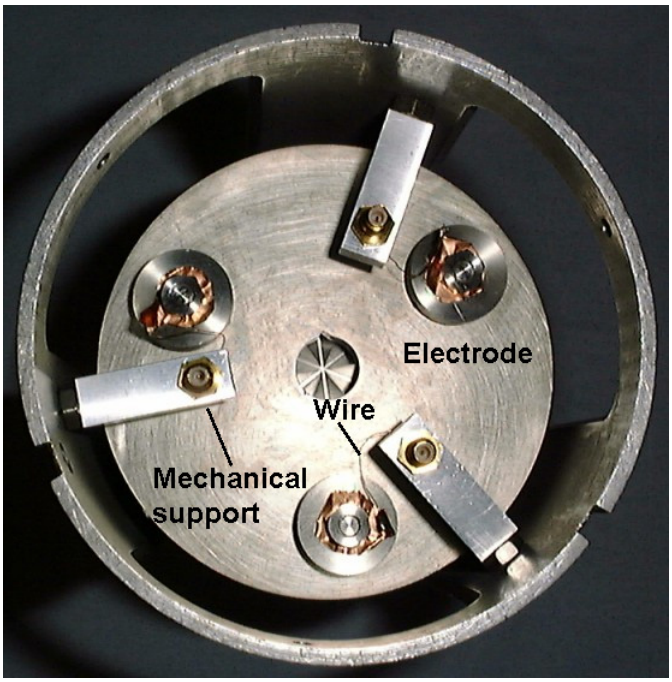

Figure 7.8: A photograph of the top disk of the capacitance cell set in the aluminium tube, taken from top. Three electrodes are kinematically mounted on the top disk. Three mechanical supports for the SMC connectors are firmly fixed on the aluminium tube so that the top disk is insensitive to the movement of the coaxial cables during the cooling down (see Section 7.4.2).

using the capacitance bridge (General Radio 1615-A, resolution 10 aF or 10^{-17} F). The cooling took approximately 5 hours.

Temperatures were measured by two platinum resistance thermometers (Farnell 541-102, temperature range -200 $^{\circ}C$ to 800 $^{\circ}C$ [101]) fixed at two positions on the aluminium tube as shown in Figure 7.5.

7.4.2 Technical details

Fixing cables

Coaxial cables (diameter 2.5 mm, RG179) and SMC connectors were used to apply voltage on the capacitors. As shown in Figure 7.8, the connectors were mechanically attached to the aluminium tube so that the movements of the coaxial cables would not disturb the measurements. The coaxial cables can move because of the thermal contraction/expansion during cooling down/warming up. One end of copper wires/gold wires (of diameter 20 microns) were soldered to copper washers fixed at the top parts of the electrodes and the other ends were soldered to the SMC connectors. Similar mechanical supports were used for the supply of the low voltages (Figure 7.5). It is essential to use fine wires; if they are too stiff, the movement of the wires during cooling down could push the electrodes and/or the top disk and disturb the experiment by changing the gap.

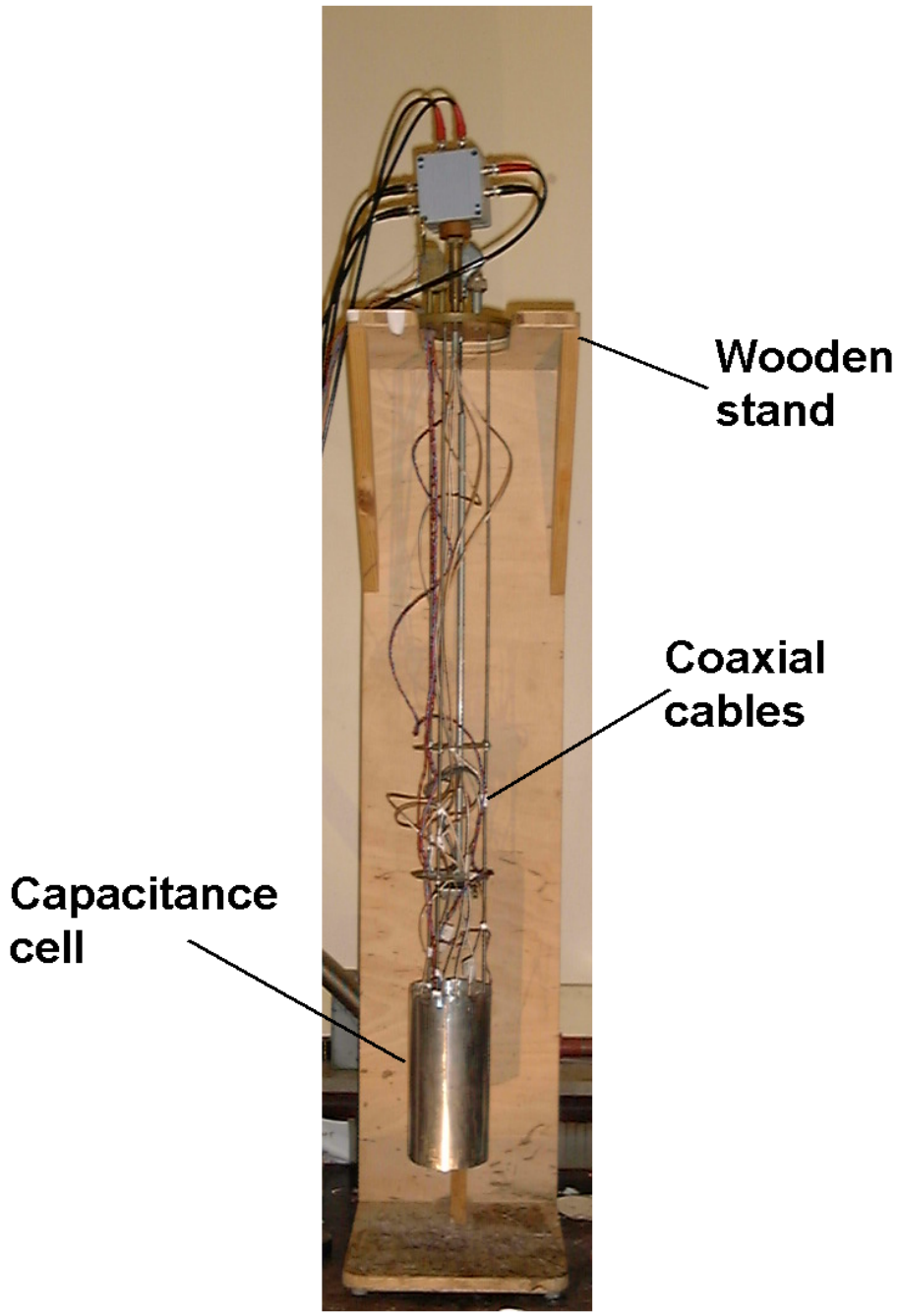

Figure 7.9: A photograph of the cryostat insert suspended on a wooden stand. The capacitance cell is wrapped by an aluminium sheet.

7.5 Mounting system

The measurements of differential thermal expansion are directly affected by the change in the height of the samples to be measured. Therefore, stable mounting of the samples is essential for the experimental design. Sufficiently stable mounting is achievable by employing kinematic mounts (see Section 7.5.1 for details). Every time it is mounted, proper kinematic mounts allow a sample to be located at an unique position within 0.1 μm [102]. As we will see in Section 7.5.1, kinematic mounts normally involve machining of samples.

A special facility is necessary to machine the beryllium samples because of the hazard; inhalation of beryllium powder can cause death [103]. We do not have any access to a facility that can machine beryllium. Therefore, we developed a mounting system that can fix samples stably without machining the samples.

7.5.1 Typical kinematic mounts

To fix a sample at an unique position, it is necessary to constrain six degrees of freedom of the sample: x, y, z, α, β and γ (see Figure 7.10). The restriction of the six degrees of freedom can be achieved by having the sample touched by six points.

A typical kinematic mount[3], which is generally used for various experiments to mount a sample, is shown in Figure 7.11 [104]. For instance, a cylindrical sample with three balls, each of which fits in a v-groove on the disk, firmly attached to it can be mounted at a unique position on the disk. Usually, three cones are machined on the

[3]See, for example, [104] for other typical kinematic mounts.

sample to fix the three balls (as we will see in Section 7.5.3, we used tetrahedron-shaped blind holes instead of the cones to prevent instability caused by imperfect machining of the cones). The six degrees of freedom of the sample are constrained as the balls touch at the six points drawn in Figure 7.11.

Kinematic mounts generally satisfy the following requirements:

- a sample can be located at one unique position,
- good tolerances are not required in the design of the kinematic mounts.

It is clear that high precisions are not crucial for the typical kinematic mount of Figure 7.11; the separation of the v-grooves does not have to be exactly 120 degrees; the positions of the three ball bearings can be anywhere within the allowed length of the v-grooves as, in general, any three points that define a plane can find one unique position in three v-grooves.

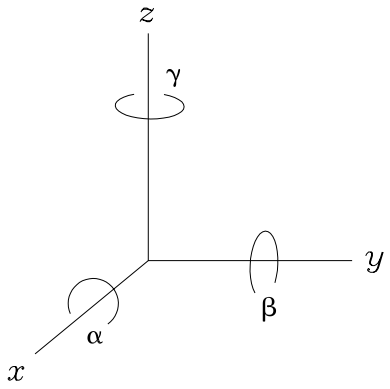

Figure 7.10: Six degrees of freedom

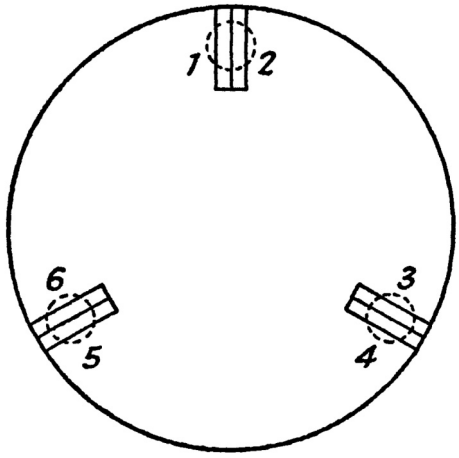

Figure 7.11: A schematic view of a typical kinematic mount (quoted from [104]). Three balls (circles of dashed lines), fixed on the sample to be mounted, sit in the v-grooves and touch at the six points.

The kinematic mounts used for the spacer, the top disk, and the electrodes are slightly different from the one we described above. In the kinematic mounts used for these parts, both the piece to be mounted and the mounting piece have v-grooves (see Figures 7.7, 7.12 and 7.13 for the v-grooves). Therefore, the ball bearings can move along the v-grooves, and every time the pieces are assembled, they sit at a different position. The magnitude of this difference depends on the machining tolerance of the v-grooves. However, this mounting is stable unless the ball bearings move. In our experiment, all the components (except the ball bearings) are made by the same material (titanium) to avoid the movements of the ball bearings by the differential thermal expansion. We used this mounting because we believed that this method requires less machining tolerances than having cones to mount ball bearings; the cones

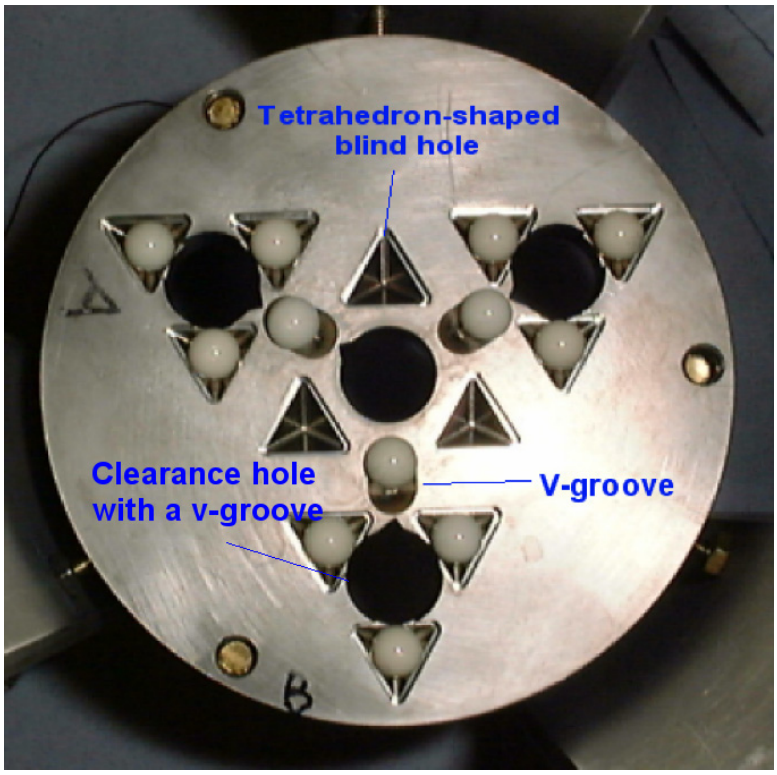

Figure 7.12: A photograph of the bottom disk with alumina balls. Three v-grooves at the central part of the disk is to mount the spacer.

should not be elliptic to a high precision, otherwise, the ball bearings cannot sit on them stably.

However, we cannot use these typical kinematic mounts described above for the beryllium samples as we cannot fix balls on the sample nor machine v-grooves on it. We will describe the conditions required for the mounting system for our experiment in the next section.

7.5.2 Conditions for the mounting system in our experiments

There are three requirements on the mounting system for our experiment: firstly, it has to work at a cryogenic temperature. The relative length of materials changes with

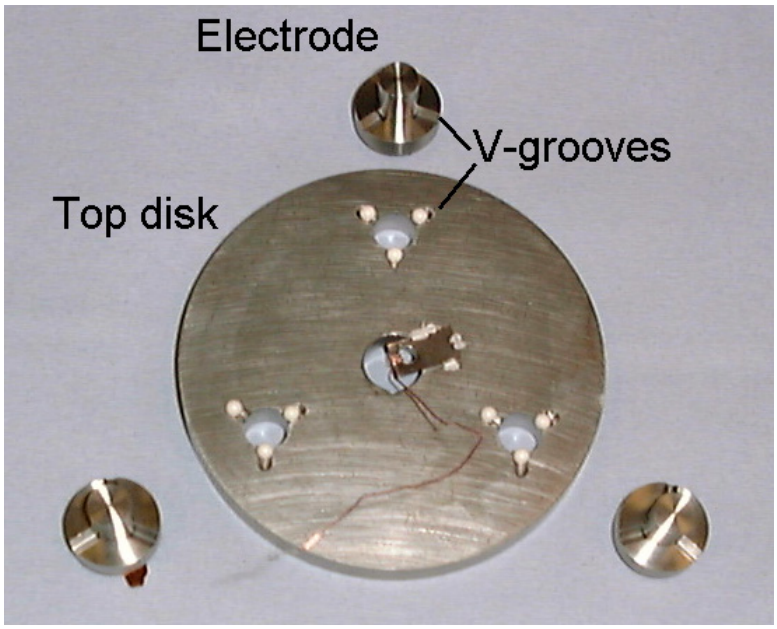

Figure 7.13: A photograph of the top disk, with alumina balls set on the v-grooves, and the electrodes.

temperature because of their different thermal expansions. For example, if there is no room for the materials used in the mounting system to move, the difference in thermal expansion could destroy some parts of the system. Secondly, as mentioned before, the samples cannot be machined. Thirdly, no adhesive can be used between the sample and the position where the sample sits. Performances of our prototype mounting methods (not described in this thesis) showed that use of adhesive (superglue and cryogenic epoxy) between them introduced significant instability in the measurements.

However, the horizontal movement (parallel to the bottom disk) of the samples is not crucial for our experiment. The capacitances are sensitive to the change in the gap, but not sensitive to the horizontal movement to the first order. In our device, the rotation axis (perpendicular to the bottom disk) of the samples is aligned to the centre

of the electrode. Therefore, the rotation of the sample is not critical either.

In summary, the mounting system for our experiment should satisfy the following conditions:

1. it has to work at cryogenic temperatures,
2. samples do not require machining,
3. no adhesive should be used between the sample and the place where the sample sits and
4. horizontal movements and axial rotations of the sample are not critical.

7.5.3 Mounting system for our experiment

In this section, we will describe the overview and the principle of the mounting system, and three aspects considered in the design of the mounting system.

Overview

We have developed a mounting system which satisfies the conditions described in the previous section. A schematic extended view of the mounting system is shown in Figure 7.14. There are several differences between the real mounting system and that shown in Figure 7.14. This figure shows one set of holes for the mounting of a cylindrical sample on the titanium disk. However, the shape of the measured samples was not a cylinder but a segment (Figure 7.16). The real disk has four such sets of holes as shown in Figure 7.12. Three of them were used to mount segmented samples and the spacer

was mounted in the center by the typical kinematic mounts, as shown in Figure 7.7. Tetrahedron-shaped blind holes instead of cones (Figure 7.12) were used to prevent instability caused by imperfect machining of cones.

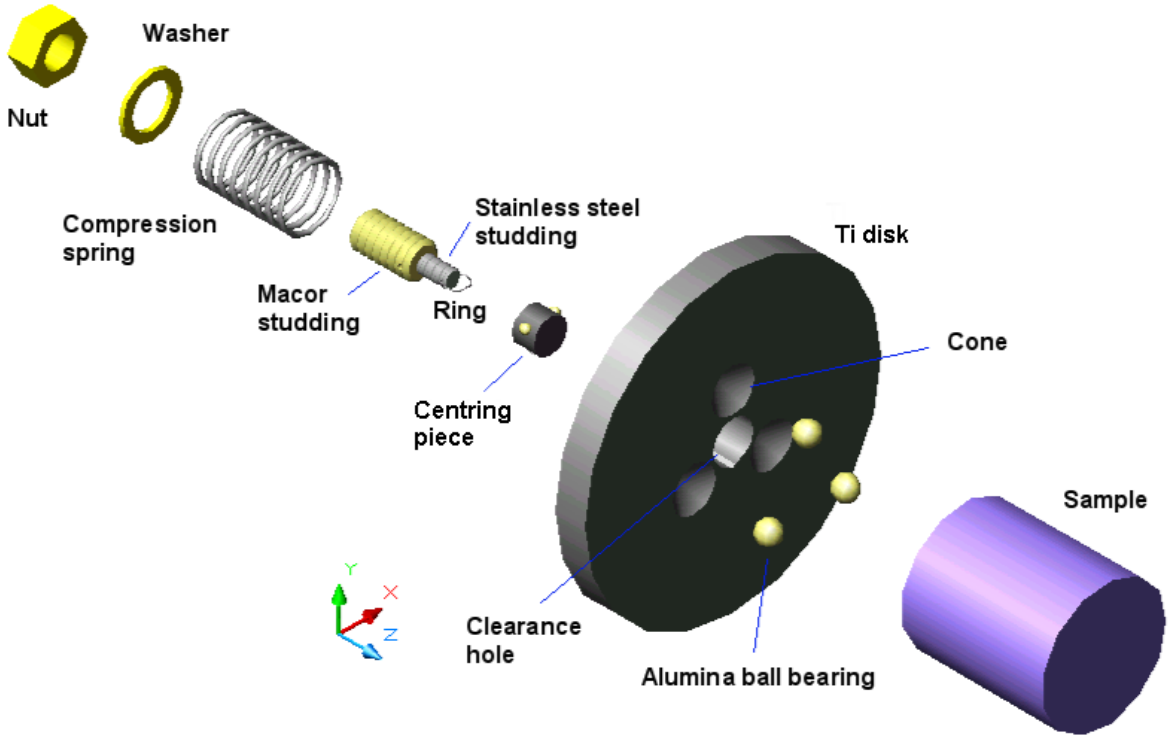

Figure 7.14: A schematic extended view of the mounting system

A piece referred to as the centring piece in Figure 7.14 is composed of a plunger screw, two macor screws with hemispherical ends and a titanium cylinder with a blind hole (Figure 7.15). The plunger screw contains a spring and the macor head can slide within the screw.

The centring piece is glued on a flat surface of a sample. Stainless steel studding is screwed into macor studding as shown in Figure 7.14. A ring attached to the stainless steel studding loops around the plunger screw of the centring piece. The ring is

sufficiently large so that the connection between the centring piece and the stainless steel studding is flexible. The sample sits on the three alumina ball bearings which sit in the cones (the tetrahedron-shaped blind holes in the real system) of the titanium disk. The pieces attached to the sample (Figure 7.16) go through a clearance hole, with a v-groove, in the disk and the centring piece fits in the clearance hole as shown in Figure 7.15. The compression spring goes outside of the studdings. A nut with a washer is screwed on the macor studding to compress the compression spring. The force due to the compressed spring pulls down the sample on the three ball bearings. The final assembly can be seen in Figure 7.5.

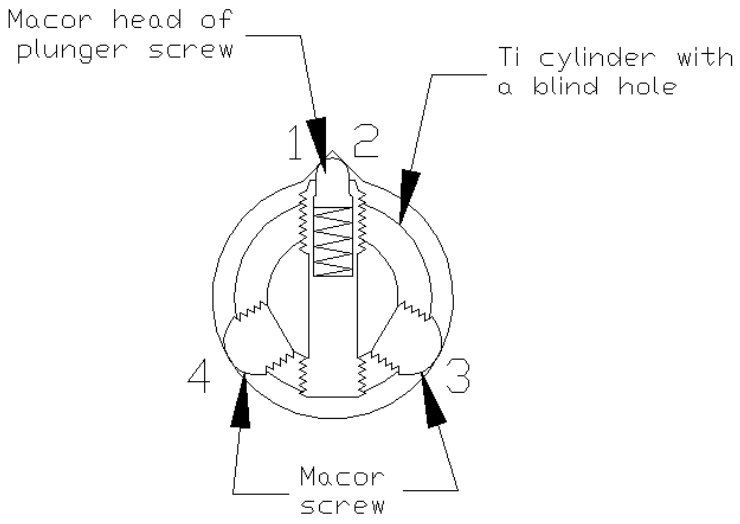

Figure 7.15: A cross section of the centring piece which fits in a clearance hole with a v-groove of the disk (this figure is drawn to scale, except the spring in the plunger screw). The diameter of the blind titanium cylinder is 9 mm and the height is 6 mm. The centring piece touches the disk at four points to constrain the three degrees of freedom (x, y and γ) of the sample. The head of the plunger screw touches the v-groove. The head of the plunger screw and the hemispherical screws are made of macor. All the other parts, except the spring in the plunger screw (the spring is made of stainless steel), are made of titanium.

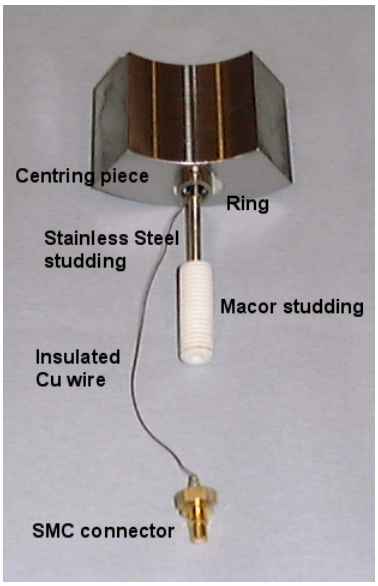

Figure 7.16: A sample with pieces for mounting attached. The height of the sample is 37.1 mm.

Principle of the mounting system

The mounting system constrains the six degrees of freedom of a sample as follows. Here we set the origin of the coordinates shown in Figure 7.14 at the center of figure of the centring piece in the clearance hole. This coordinate system will be used throughout the rest of this section.

1. the three ball bearings constrain the plane where the sample sits, namely z, α and β,

2. the v-groove through the clearance hole of the disk constrains the rotation of the sample around the z-axis, namely γ (see Figure 7.15) and

3. the centring piece constrains the horizontal shift of the sample, namely x and y (see Figure 7.15).

Even though there are seven contact points (three points touch the ball bearings and four points of the centering piece touch the bottom disk) in the mounting system, it is not over-constrained. Two contact points by the plunger screw at the v-groove does not constrain any degree of freedom completely because of the spring of the plunger screw (see Figure 7.15).

Mechanical aspects

If a force is applied to the sample, it can move in any direction around any pivot point out of the seven contact points. It is important that the sample comes back to its original position to a sufficient level when the force is released. There should not be any friction that is large enough to prevent the sample from coming back to the original position. For example, if the friction between the centring piece and the surface of the clearance hole is too big, the plane may be determined by the contact points of the centring piece and the sample may not sit on the three ball bearings.

The mounting system is designed to minimise friction. The height of the centre of the hemispherical macor heads of the centring piece and the centre of the ball bearings are aligned as shown in Figure 7.17. This alignment minimises the friction that arises between the macor heads and the surface of the clearance hole of the disk when the sample tilts around the x and y axes. Figure 7.17 shows a track of a macor head of the centering piece when the sample tilts around a ball bearing. From the track, one can see that the sample is virtually free to tilt around the x and y axes and to come back to the original position.

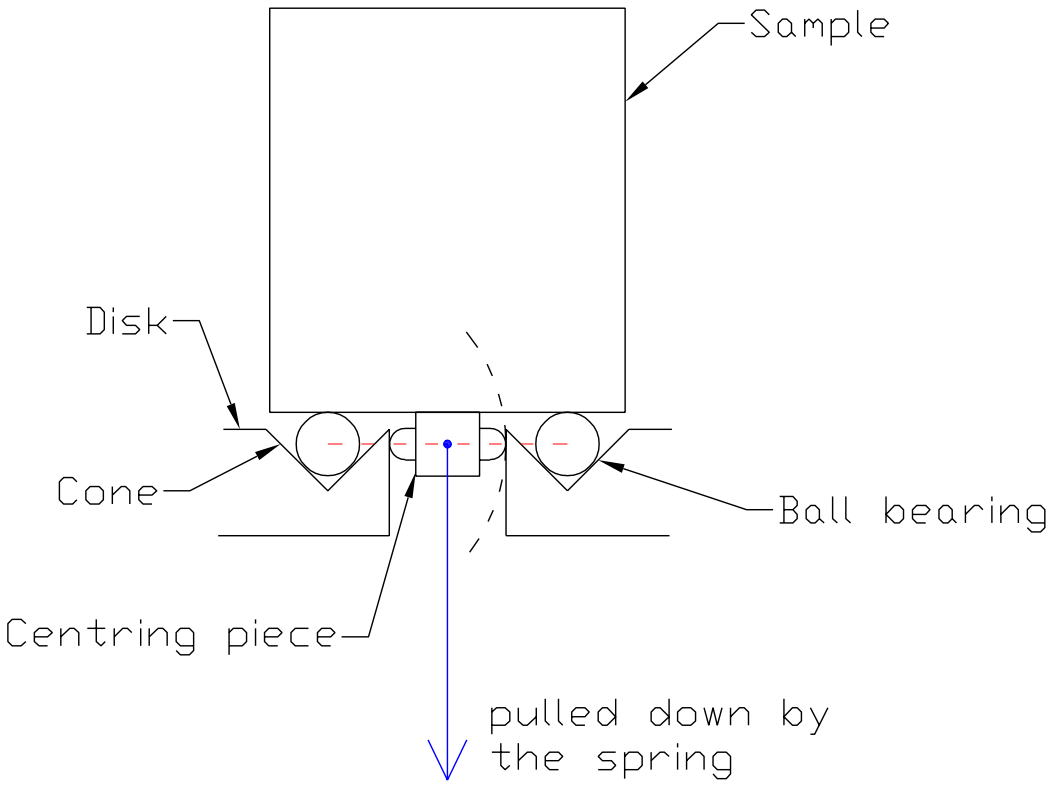

Figure 7.17: A schematic cross section of the mounting system. (The studding and the compression spring are omitted in this figure. This figure schematically shows the tetrahedron-shaped blind holes and macor screws/head of the centring piece on one plane. However, of course, they are not on the plane in the real mounting system as one can see in, for example, Figures 7.14 and 7.15.) The horizontal dashed lines show the alignment of the centres of ball bearings and the contact points of the centring piece. The dashed arc shows the track of the macor head when the sample tilts around the left ball bearing.

The force applied by the compression spring to pull down the sample on the three balls should not produce any torque. The best point to apply the force is in the plane of the centre of three ball bearings, namely roughly the middle of the centring piece (Figure 7.17). In the mounting system, the ring is looped around the plunger screw. The joint is flexible so that there is no need for aligning the point of application of the force with high accuracy.

The force applied by the compression spring has to be sufficiently small to avoid making dents on the samples and the bottom disk. We have estimated the maximum allowed load by using a formula in [105]. For this purpose, the spring should not be compressed more than 0.5 mm, which corresponds to approximately 0.5 N. Here, the weight of the pieces is included in the calculation.

As for the rotation around the z axis, the four contact points of the centring piece can be a pivot point. In any case, the plunger screw works to let the sample come back to the original position.

As regards the horizontal shifts, again, the plunger screw guides the sample back to the original position.

However, the freedom that allows the head of the plunger screw to slide allows some rotation and horizontal shift of the sample. However, as described in Section 7.5.2, the rotation and horizontal shift are not crucial for our experimental set-up.

We have carefully lifted up a sample, mounted on the disk by using the mounting system, by pushing up the nut by roughly 0.5 mm and letting it go. We have measured

the capacitance before and after the lift and repeated this process more than 10 times for the three samples mounted. The change in the capacitance was within 30 aF for all the samples, which corresponds to roughly 80 nm. This shows that the performance of our mounting system is equivalent or better than the typical kinematic mounts. However, it should be noted that the capacitance measurements are dominantly sensitive only to the change in the gap. Therefore, it can be said that our mounting system may not be good enough for some experiments that are sensitive to the horizontal shift or rotation, but it works, at least, at the same level as the typical kinematic mount for our purpose.

Electrical aspects

The sample has to be electrically isolated from the bottom disk, where the sample is mounted, as the bottom disk is connected to the ground of the capacitance bridge (Section 7.2). For this purpose, the ball bearings and the contact points of the centring piece were made from insulators of alumina and macor, respectively.

Differential thermal expansion

To make the mounting system work at a cryogenic temperature, thermal expansions of the materials used for the mounting system have to be taken into consideration.

The centring piece is glued on the sample. The main body of the centring piece is made of titanium, whose thermal expansion is close enough to beryllium. We have tried several materials, such as brass and macor. We glued these materials to a beryllium sample with several adhesives (superglue, Aroldite and cryogenic epoxy) and immersed

them into liquid nitrogen. But they came off after the immersion.

As macor shrinks more than titanium by roughly 50 % at the liquid nitrogen temperature ([106] and [76] for the thermal expansion of macor and titanium, respectively.), the spring in the plunger screw, which is compressed when it is set in the clearance hole at room temperature, expands when cooled and introduces a small horizontal shift of the sample. In order to minimize this shift, it is best to make the centring piece from the same material as the disk. However, as mentioned before, we have to use an insulator at the contact points. We chose macor as it is a machinable insulator and the thermal expansion of macor is close to titanium among other insulators.

7.6 Measurements

7.6.1 Experimental procedure

The experimental set-up and measurements were proceeded in the following order:

1. All the parts for the capacitance cell were cleaned using acetone and a air duster.
2. They were assembled to build the capacitance cell.
3. The cables were connected with the SMC connectors and wires were soldered to connect the connectors and the electrodes.
4. The capacitance cell was set in the insert and placed in the inner dewar.
5. The air in the inner dewar was pumped out with a vacuum pump, and replaced with helium gas.

6. The experiment was left for at least a few hours until the readings of the capacitance settled down after the pumping.

7. The capacitances and the temperatures at room temperatures were measured with the capacitance bridge and the thermometers, respectively.

8. Liquid nitrogen was supplied into the outer dewar until the readings of the thermometers stopped changing.

9. The capacitances were measured at the cool temperature.

10. The experiment was warmed up naturally for roughly one day.

11. The capacitances were measured at the warm temperature.

We cooled down the experiment eight times and took data. After the eighth cool down, we took out the capacitance cell from the dewar and rotated the position of the samples. With this setting, we cooled down three times and took data to check whether there is a dependency of sample positions. No significant position dependency was observed (see Section 7.7.4).

No temperature control system was employed.

7.6.2 Samples

Three samples (samples 102, 104 and 112) were chosen from the HIPed beryllium samples used for the density inhomogeneity measurements (Chapter 5). The three samples showed the least density differences.

7.7 Experimental results

7.7.1 Measured capacitance

Typical raw data of measured capacitances for samples 102, 104 and 112 are plotted in the order of measurements in Figure 7.18, respectively. Figure 7.19 shows the average capacitance of three. In these figures, capacitances measured at a warm and a cool state are indicated by warm and cool, respectively. No allowance has been made for the variation in ambient temperature in these plots.

The first thing to notice is that before the fourth warm state (warm 4), the capacitances of all samples were larger at warm states than cool states. At the fourth warm state, the capacitances of sample 104 increased from the third cool state (cool 3) but the capacitances of samples 102 and 112 decreased. The average capacitance did not show a dramatic change at the fourth warm state.

Figure 7.20 shows all the measured capacitances (scaled to make the average capacitance of each sample zero) at warm temperatures versus temperature. In this figure, one can see that the average capacitance showed a smooth curve through the temperature range, but the individual capacitances at the low temperature region (roughly $12.0 \sim 14.0\ ^{\circ}C$) and at the high temperature region (roughly $19.5 \sim 22.5\ ^{\circ}C$) are discontinuous. The data at the high temperature region were from the first three cooling downs. From the fourth warm states, the warm temperature decreased because of the cut-off of the central heating over Christmas vacation, 2001.

From these figures, it is likely that a tilt of the top disk, which makes the gap of

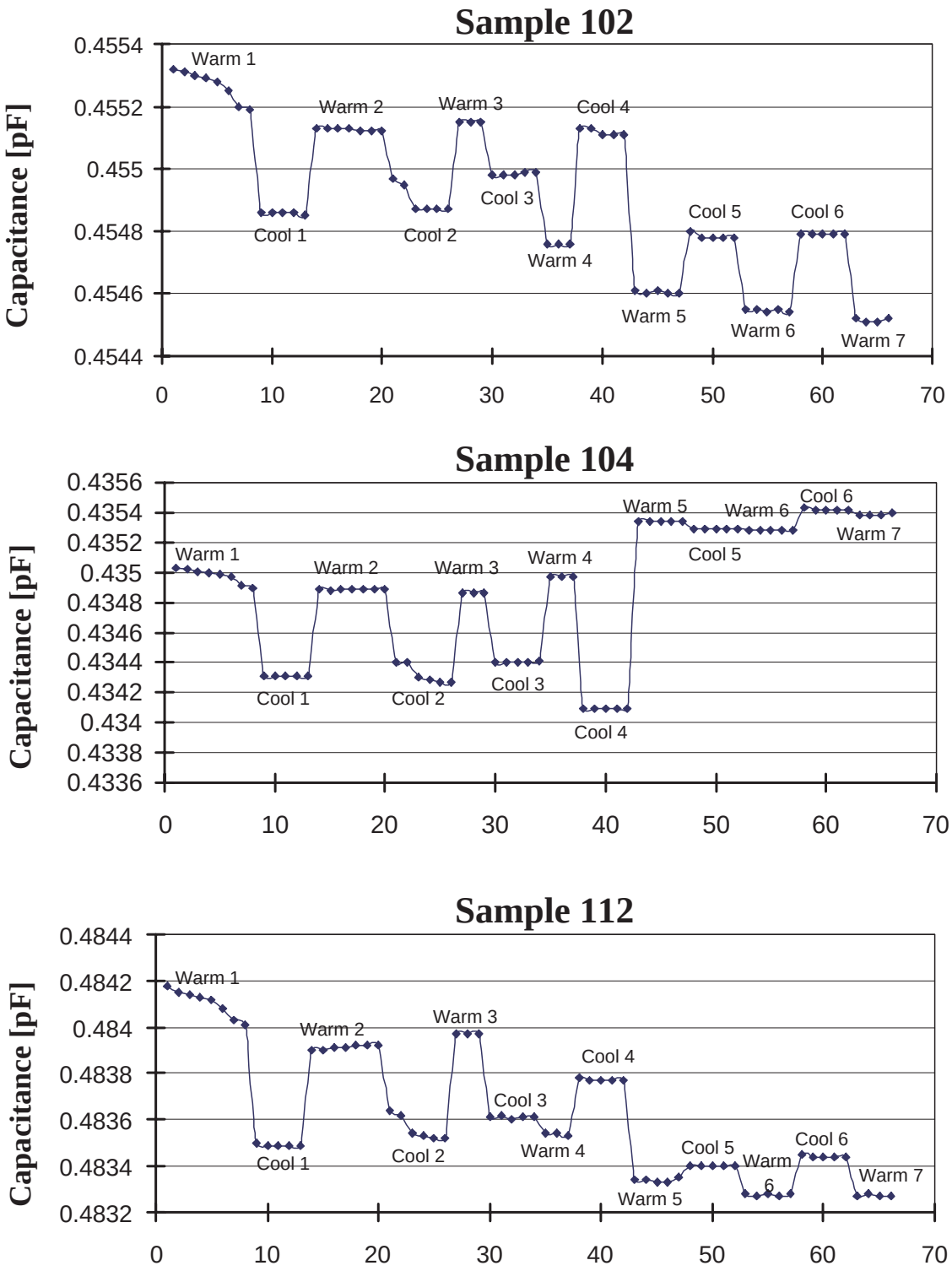

Figure 7.18: Capacitance of samples 102, 104 and 112

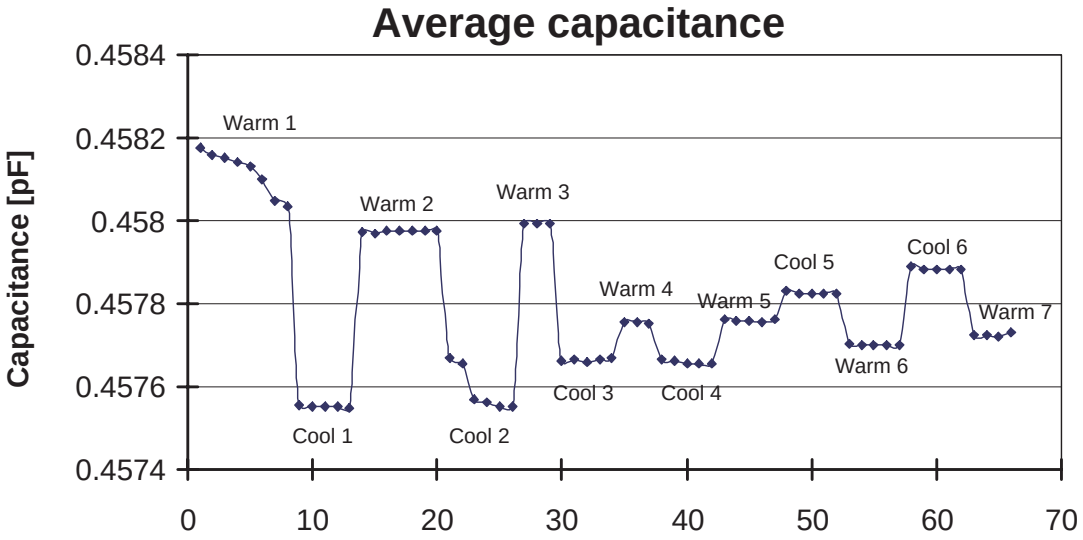

Figure 7.19: Average capacitance

sample 104 small, occurred before and after the cut-off of the central heating.

7.7.2 Estimation of differential thermal expansion

We have estimated the differential thermal expansions between the samples for each cooling down, which has a warm state before the cooling-down, a cool state and a warm state after the cooling-down.

Raw data were analysed in the following way to estimate the differential thermal expansion between the samples:

1. the capacitance at the average temperature of each warm state was estimated by least square fitting of the measured capacitances at the warm temperatures.

2. we took the average of the estimated capacitances at the two warm states and used it as the representative capacitance of the warm states.

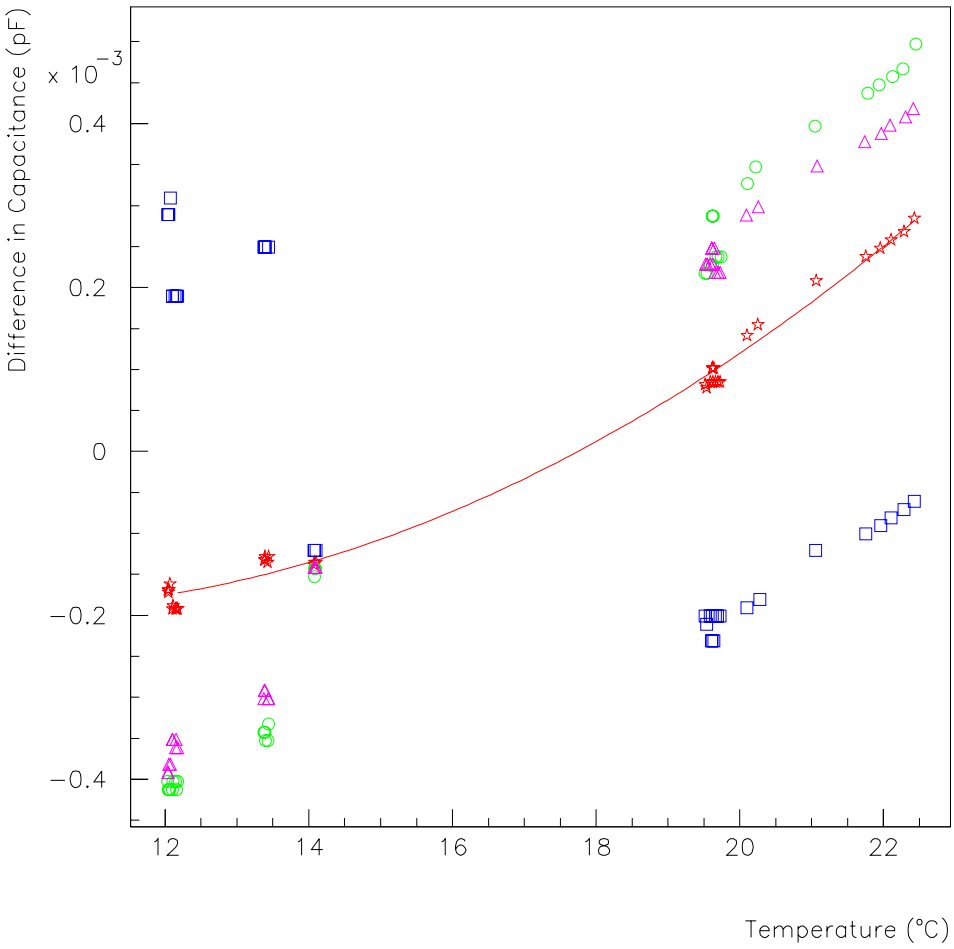

Figure 7.20: The average capacitance of each sample is subtracted from the measured capacitances and plotted versus temperature. Triangles, squares, circles and stars are the values of samples 102, 104, 112 and the average, respectively.

3. the capacitance at the cool state was estimated by least square fitting.

4. the representative capacitances of the warm state and the cool state were used to estimate differential thermal expansion by using Equation (7.17).

7.7.3 Uncertainty

Differential thermal expansion is roughly proportional to the difference in the change of capacitance between two samples (see Equation (7.17)). The estimation of differential thermal expansion between sample 1 and 2 is not affected if C_1 and C_2 changes by the same amount. This common change of capacitance can occur, for example, if there is a drift in the readings of the capacitance bridge; if there is a leak in the inner dewar and helium gas is replaced by the air; if the top disk or the spacer tilted towards sample 1 by the same amount as sample 2.

However, the estimation of differential thermal expansion is affected by non-common changes, such as the tilt of the top disk by a different amount towards the samples and some problems in an individual mounting system. These non-common effects can be estimated by comparing ΔC_{12} at the warm temperature before the cooling with one at the warm temperature after the cooling. A significant discrepancy between them can be considered as the result of the non-common effects during the cooling down. When the discrepancy/$\sqrt{2}$ is more than the uncertainty in C_1 and C_2, estimated from the least square fitting (see Section 7.7.2), we took the discrepancy/$\sqrt{2}$ as the uncertainty of C_1 and C_2. Because no temperature control system was employed, the warm temperatures

before and after the cooling down were usually different. Therefore, the discrepancy contains the temperature effects, which are due to the differences in thermal expansion between the samples. We estimated the temperature effects from the data taken at the room temperatures and subtracted it from the discrepancy. The maximum temperature effect is approximately 40 aF by considering the observed maximum temperature difference of approximately 6.5 $^{\circ}C$ (before and after the cut-off of the central heating).

However, any spurious effects that repeat when the experiment is cooled down and warmed up cannot be estimated in the way described above. Spurious effects may be checked by cooling down several times. In general spurious effects would not repeat after several cooling-downs. In our experiment, spurious effects seem dominantly due to the tilts of the top disk (Section 7.7.4).

7.7.4 Results

Figure 7.21 shows the estimated differential thermal expansions $\Delta TE/TE_{Be}$, where TE_{Be} is the integrated thermal expansion of beryllium, estimated from Swenson's data [78], over the temperature change (for example $TE_{Be} = -1.29 \times 10^{-3}$ for the temperature change from 293 K to 77 K). The drawn errors were estimated in the way described in the previous section.

The data presented in Section 7.7.1 correspond to the results of the numbers from 3 to 8 on the x-axis of Figure 7.21. The results of number 5 and 6, which showed discontinuous changes in the individual capacitances (Section 7.7.1), are significantly different from the other results. The experimental set-up of the measurements for the

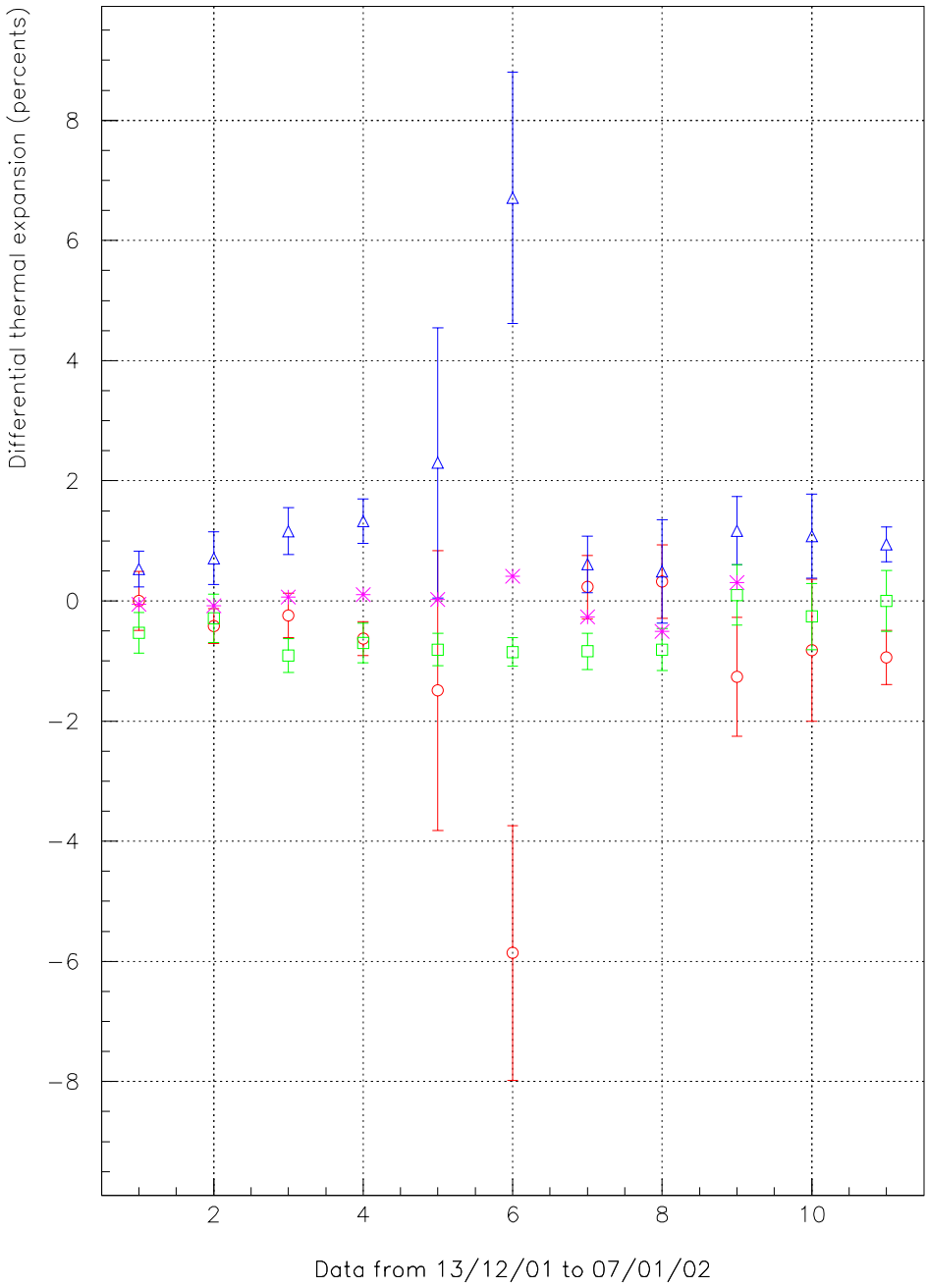

Figure 7.21: The differential thermal expansion of the beryllium samples. Squares, circles and triangles are $\Delta TE_{102,112}/TE_{Be}$, $\Delta TE_{112,104}/TE_{Be}$ and $\Delta TE_{104,102}/TE_{Be}$, respectively. Asterisks are $\Delta TE_{Avg,Be}/TE_{Be}$ (scaled to make the average of the plotted $\Delta TE_{Avg,Be}/TE_{Be}$ zero).

results of the numbers 1 and 2 was the same as one for the results of the numbers from 3 to 8. The results after rotating the position of the samples are plotted from number 9 to 11 on the x-axis of Figure 7.21.

The difference between the average thermal expansion of the three samples and the expected thermal expansion from Swenson's data ($\Delta TE_{Avg,Be}/TE_{Be} = (TE_{Avg} - TE_{Be})/TE_{Be}$) is also plotted in Figure 7.21 (scaled to make the average of the plotted $\Delta TE_{Avg,Be}/TE_{Be}$ zero). TE_{Avg} was obtained from Equation (7.6)[4]. Δd in Equation (7.6) was obtained from Equation (7.10) by substituting the average capacitances of three capacitances estimated in the way described in Section 7.7.2. The values of $\Delta TE_{Avg,Be}/TE_{Be}$ for the results of number 10 and 11 are not plotted because of the following reason: the pipe to supply helium gas into the dewar was closed without any notice by a technician because of a sudden failure in the helium supply system. Therefore, we could not estimate the permittivity to a sufficient accuracy for those data. However, this is a common effect for all the samples and did not affect the results of the differential thermal expansion significantly as shown in Figure 7.21.

As shown in Figure 7.21, no significant differences in $\Delta TE_{Avg,Be}/TE_{Be}$ were observed. It indicates that the large differences at number 5 and 6 are effects that cancel out. If the large difference of approximately 6 % is due to some problems of one sample (sample 104), the average thermal expansion should be different from others by approximately 2 %. Therefore, together with the observation described in Section 7.7.1,

[4]For simplicity, the gap was assumed as the difference in length between the reference and the sample (Equation (7.2)) when Equation (7.6) was derived. In practice, all the factors on which the gap depends, such as the height of the ball bearings, were considered.

the anomalies at number 5 and 6 are possibly due to tilts of the top disk. The standard deviation of $\Delta TE_{Avg,Be}/TE_{Be}$ for all the plotted values is 0.3 %.

By taking the weighted average of all the results, we obtain:

$$\Delta TE_{102,112}/TE_{Be} = (-0.7 \pm 0.3)\% \quad (7.18)$$

$$\Delta TE_{112,104}/TE_{Be} = (-0.6 \pm 0.3)\% \quad (7.19)$$

$$\Delta TE_{104,102}/TE_{Be} = (0.9 \pm 0.3)\% \quad (7.20)$$

where the uncertainties includes systematic errors in the quantities used in the calculation (namely, ϵ, L_S, R_{Ele}, C and TE_{Ele} in Equation (7.17)) and due to the gap difference between positions (see the discussion at the end of the Section 7.3.4). The maximum difference in the thermal expansion was $(0.9 \pm 0.3)\%$.

7.8 Discussion

We have observed the maximum differential thermal expansion of $(0.9 \pm 0.3)\%$, which is the level of the maximum allowed anisotropy of the thermal expansion of a beryllium STEP test mass (Section 6.2). This could be due to the residual stress in the samples. Stress relief of the samples may reduce the differential thermal expansion. It is reported that extensive stress relief is important to fabricate thermally stable HIPed beryllium [90] (see also Section 6.3.3).

In general, residual stress in samples seems to affect the thermal expansion. Usually measurements of thermal expansion are done using stress relieved samples (e.g. [76, 77]). Rosenfield and Averbach have measured the coefficient of thermal expansion of

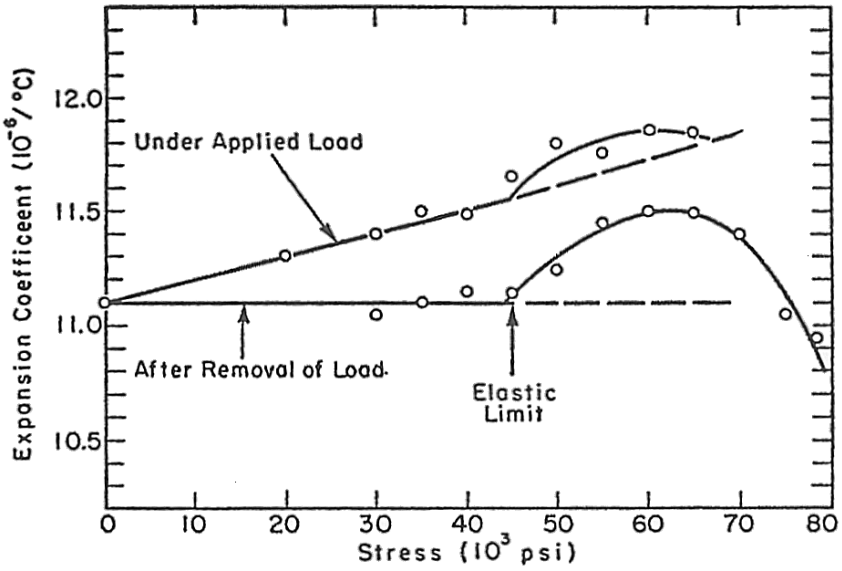

Figure 7.22: Effect of stress on the thermal expansion of a 1020 steel (quoted from [107])

specimens under tensile stress and after the stress has been removed for steels and Invar [107]. One of the results is shown in Figure 7.22. When the applied stress was below the elastic limit, the coefficient of thermal expansion returned to the original value when the stress was removed. However, if the applied stress exceeds the elastic limit, the contraction on unloading differed from the original value. In the figure, the maximum residual difference in the coefficient of thermal expansion, which occurred at the stress of approximately 6×10^4 psi[5] or 0.4 GPa, is roughly 4 %.

There may be two aspects related to the tilt of the top disk: (1) the kinematic mounts for the disks and the spacer are not to work properly if the ball bearings move (see Section 7.5.1); their movement could cause tilts. Even though the spacer and the

[5] 1 p.s.i. = 6.894757 $\times 10^3$ Pa [108]

disks are made from the same material, the ball bearings may move. For example, if there is a temperature difference between the spacer and the top disk during the worming up/cooling down, the different rate in their expansion/contraction could move the ball bearings. Friction between the v-grooves and the ball bearings could cause instability in the mounting system as the ball bearings move. In fact, the surfaces of the v-grooves in the disks for the spacer were rough even though they were etched[6], (2) because the spacer is inside of samples, the tilt effects are magnified.

Use of the typical kinematic mounts shown in Figure 7.11 would avoid the movements of the ball bearings because the positions of cones determine the positions of the ball bearings. The surfaces of the v-grooves and the cones (or alternatively tetrahedron-shaped blind holes) have to be sufficiently smooth to prevent friction and spurious effects due to roughness of the surfaces; the contact points of the ball bearings in the v-grooves or cones change with temperature because of the difference in thermal expansion of the disks (titanium) and the ball bearings (alumina). Experiments would be less affected by tilts if the spacer sits outside of samples, for example by employing a hollowed cylindrical spacer. However, we would need a larger dewar to have this configuration in the device. There would not be enough room for cables in the aluminium tube, which fits tightly to the inner dewar.

By using the device, it is possible to obtain thermal expansions of the samples

[6]Surface finishes of the v-grooves on the disks looked much rougher than ones for the tetrahedron-shaped blind holes. The v-grooves were machined by a tool with a wide edge, while the blind holes were machined by a tool with a point edge. After the v-grooves and blind holes were machined, they were etched by a solution (1 % HF, 20 % HNO_3, 54 % Acetic Acid and 25 % of Lactic acid, where % in volume).

by using Equation (7.6). We have estimated the integrated thermal expansion from the average capacitance of three samples. The average of all the plotted values of $\Delta TE_{Avg,Be}/TE_{Be}$ in Figure 7.21 was 2.3 %. The values of $\Delta TE_{Avg,Be}/TE_{Be}$ do not depend on temperature to the first order. Therefore, with the average value and Swenson's value, we obtain the integrated thermal expansion from 293 K to 77 K as $(-1.26 \pm 0.04) \times 10^{-3}$. The uncertainty is dominantly given by the uncertainty in the thermal expansion of the reference material ($TE_{Ti} = (-1.46 \pm 0.04) \times 10^{-3}$ (from 293 K to 77 K), quoted from the recommended value in [76]). Our result agrees with the Swenson's value, $(-1.29 \pm 0.02) \times 10^{-3}$ [78].

However, to determine the thermal expansion it is important to calibrate the capacitance cell using stress relieved and recommended materials, such as copper and silicon, as a reference. We have used the titanium spacer as the reference. But the spacer is not stress relieved. Therefore, the recommended value of the thermal expansion of titanium may be different from the one of this particular spacer. Also, titanium is not recommended as a reference material of thermal expansion in literature [83]. A temperature control system is essential to measure thermal expansions/coefficients of thermal expansion as a function of temperature.

As a trial, we have supplied liquid helium into the inner dewar to cool down the capacitance cell to the liquid helium temperature. But the result looked limited by the tilt of the top disk, possibly caused when the liquid helium was boiling off at the level of the top disk.

We have measured differential thermal expansion of samples in their axial direction. However, the worst effects on the STEP experiment would come from the change in the aspect ratio of the test masses. Therefore, it is important to measure the difference in thermal expansion between the axial and the radial direction. For example, this difference can be measured with the device if the samples are cubes. Firstly we can measure difference in thermal expansion between a cubic sample in the axial direction and a reference. Secondly we can rotate the cubic sample so that we can measure the difference in thermal expansion between the sample in the radial direction and the reference. We can estimate the anisotropy of the sample by comparing the results of the first and the second measurements.

7.9 Conclusions

We have seen that the device developed here has a sufficient precision to check the anisotropy in thermal expansion of HIPed beryllium for STEP.

The results of three HIPed beryllium samples, prepared from the billet for a prototype STEP test mass, showed a maximum difference of (0.9 $\pm$ 0.3) % in the thermal expansion. This is the level of the allowed anisotropy of thermal expansion for STEP test masses, derived in Section 6.2. The difference could be due to the residual stress in the samples. Annealing the samples may reduce the differential thermal expansion. For example, we can measure the differential thermal expansion of the samples after annealing them and compare the results presented here. Stress relief also may improve

the density homogeneities (see Section 8.5).

The mounting system developed here can mount a sample without machining it. This mounting system might have several applications. By using the mounting system the device can potentially be developed to measure, for instance, the thermal expansion (and isotropy of the thermal expansion) of the real STEP test masses in the final shape. Also, we could study the thermal expansion of the Pt/Ir alloy, one of the strongest candidate material for STEP test masses.

Chapter 8

Discussion

8.1 Test mass selection

We have discussed STEP test-mass selection in Section 2.4.1. In Figure 2.10, the most different pair of elements is Be-Bi. From the figure, it is clear that Be should be used. However, the heavy elements (Ta, W, Ir, Pt Au and Bi) are close each other in the figure. Therefore, we can choose any of them as a test mass material without significantly losing the sensitivity of STEP. As regards machinability, none of the heavy elements in pure form seems suitable as test masses, except Ta. They are probably too soft or brittle and, therefore, they have to be used as alloy.

At the moment, Pt is the most strongest candidate among them. Pt/Ir (Ir 10%) alloy is an alternative to pure Pt as this is probably too soft. However, Pt/Ir alloy might have a significant density inhomogeneity because it is not a single element; ie the distribution of Ir may not be sufficiently even. The average density of two different Pt/Ir ingots typically differers by about 500 ppm and it is correlated with variations of iridium content of 10 % by mass [68]. However, density measurements of sliced

Pt/Ir samples (7 samples, the diameter and height are both approximately 40 mm) from one ingot showed a density variation of less than 7 ppm [68]. The uncertainty of the measurements was about 1 ppm. The value of thermal expansion of Pt/Ir at low temperature is not available in literature (see Section 6.1). Therefore, studies on density inhomogeneities, thermal expansion and distortion of Pt/Ir alloy are necessary. However, it is difficult to obtain samples for those studies because it is very expensive.

Tantalum satisfies most of the technical requirements; it is not difficult to machine and its thermal expansion data is available in existing literature [76]. Also, there are no possible causes of density inhomogeneities nor thermal distortion; it is a single element (not a composite) and has isotropic thermal expansion. In addition, according to Goodfellow's catalogue [109], tantalum is roughly five times less expensive than Pt/Ir alloy.

8.2 Estimation of allowable local source masses for STEP

We have discussed density homogeneity and thermal distortion in this thesis. So far, we have assumed a 1-g helium bubble at 250 mm from the test masses as a source and the target noise level as $10^{-18}\mathrm{m/s^2}$ to discuss allowable levels of the gravitational quadrupole moments (see Sections 3.6 and 3.7). We will estimate allowable magnitude of a source mass from the gravitational quadrupole moments, due to the imperfections in the test mass materials, which were estimated from our experimental results. As discussed in Section 3.6.1, so far we have considered all terms in Q_{30}. However, here

we will consider spurious acceleration at the signal frequency.

From Equation (3.38) we obtain:

$$\left|\frac{q_{20}}{M_{TM}}\right| < \frac{1}{4\pi G}\sqrt{\frac{5}{3}}\frac{S_Z}{Q_{30}} \tag{8.1}$$

By taking the $\cos\theta$ term of Q_{30} (Equation (3.42)), we obtain:

$$M_{SM} < \frac{4}{3G}\sqrt{\frac{5}{21\pi}}\left|\frac{M_{TM}}{q_{20}}\right| S_Z \cdot r^4 \tag{8.2}$$

From our density inhomogeneity measurements (Chapter 5) and differential thermal expansion (Chapter 7), we obtain the quadrupole moments per unit mass ($|q_{20}/M_{TM}|$, see Section 3.4.3) as follows.

From the density inhomogeneity measurements of the beryllium samples (from the rod for a prototype outer test mass) and of the niobium samples (from the rod for a prototype inner test mass), we obtain:

$$\left|\frac{q_{20}^{outer}}{M_{TM}^{outer}}\right|_{Be} = (4.8 \pm 3.5) \times 10^{-9}\mathrm{m}^2 \tag{8.3}$$

$$\left|\frac{q_{20}^{inner}}{M_{TM}^{inner}}\right|_{Nb} = (1.4 \pm 0.1) \times 10^{-9}\mathrm{m}^2 \tag{8.4}$$

Using Equation (8.2), allowable masses of a source mass at 250 mm from the centre of mass of test masses to achieve the spurious acceleration of $10^{-18}\mathrm{m/s}^2$ are 2.6 g and 14 g for the beryllium outer test mass and the niobium inner test mass, respectively.

By assuming that an outer test mass had an anisotropic thermal expansion of (0.9 ± 0.3), which is the maximum difference observed in the beryllium outer samples (see Section 7.7.4), we obtain,

$$\left|\frac{q_{20}^{outer}}{M_{TM}^{outer}}\right|_{Be} = (1.0 \pm 0.4) \times 10^{-8}\mathrm{m}^2 \tag{8.5}$$

The allowable source mass for the outer test mass is 1.5 g.

As discussed in Section 3.7, the allowable source mass determined by the shape design of STEP test masses is about 0.5 g.

8.3 Thermal expansion measurements

We found that there were no published values of the HIPed beryllium (of grade I220) and Pt/Ir alloy at cryogenic temperature (Section 6.1). Absolute values of thermal expansion of STEP test masses may be inferred from data in existing literature with a sufficient accuracy for STEP. However, it would be possible to measure them non-destructively with the device developed for differential thermal expansion measurements (Chapter 7). Reference materials have to be chosen carefully to determine the thermal expansions.

8.4 Measurements of gravitational multipole moments of STEP test masses

We have estimated quadrupole moments of test masses, due to the imperfections, by studying samples taken from the rods from which prototype test masses were made.

By using the mounting system we developed, it would be possible to measure anisotropy in thermal expansion of STEP test masses in their final shapes. Also, thermal distortion of STEP test masses may be checked by using holographic techniques. This holographic method is under study at this university as an undergraduate project supervised by Speake.

Lockerbie demonstrated a method to determine gravitational quadrupole moments of STEP test masses by measuring imbalance of moment of inertia of test masses [45, 110]. Also, Trenkel and Speake suggested direct measurements of quadrupole moments of test masses by using a cryogenic torsion balance [111].

8.5 Relationship between density inhomogeneities and differential thermal expansion

Thermodynamically, if the applied uniaxial stress σ_s is below the elastic limit the change in expansion coefficient α_{TE} is given

$$\left(\frac{\partial \alpha_{TE}}{\partial \sigma_s}\right)_T = -\frac{1}{E^2}\left(\frac{\partial E}{\partial T}\right)_{\sigma_s} \tag{8.6}$$

where

$$\sigma_s = E \cdot \epsilon_l \tag{8.7}$$

E, T and ϵ_l are Young's modulus, temperature and strain. Or the effect of applied pressure P on the coefficient of volumetric thermal expansion β_{TE} is given by

$$\left(\frac{\partial \beta_{TE}}{\partial P}\right)_T = \frac{1}{B_T^2}\left(\frac{\partial B_T}{\partial T}\right)_P \tag{8.8}$$

where

$$P = -B_T \cdot \epsilon_v \tag{8.9}$$

B_T is the isothermal bulk modulus and ϵ_v is volume strain (fractional volume change).

From Equation (8.8), the difference in β_{TE} between two samples under a different amount of pressure may be given

$$\Delta\beta_{TE} = \frac{1}{B_T^2}\left(\frac{\partial B_T}{\partial T}\right)\Delta P \tag{8.10}$$

$$= -\frac{1}{B_T}\left(\frac{\partial B_T}{\partial T}\right)\Delta\epsilon_v \tag{8.11}$$

where a relation, $\Delta P = -B_T\Delta\epsilon_v$ from Equation (8.9), is used. By using a relation, $\Delta\epsilon_v = \Delta V/V = -\Delta\rho/\rho$, we obtain

$$\Delta\beta_{TE} = \frac{1}{B_T}\left(\frac{\partial B_T}{\partial T}\right)\frac{\Delta\rho}{\rho} \tag{8.12}$$

or by integrating both sides of this equation over temperature

$$\Delta TE_{VTE} = \frac{\Delta\rho}{\rho}\int\frac{1}{B_T}\left(\frac{\partial B_T}{\partial T}\right)dT \tag{8.13}$$

From these equations, one can see that difference in thermal expansion is related to difference in density.

For instance, in the case of copper, $\int(1/B_T)\,(\partial B_T/\partial T)\,dT \sim 0.04$ (from 300 K to 77 K) [112]. Therefore, from Equation (8.13), the difference in volumetric thermal expansion is roughly 0.1 % ($TE_{VTE_{Cu}} \sim -9\times10^{-3}$) for a density inhomogeneity of 200 ppm.

Chapter 9

Conclusions

Preliminary work for the verification of STEP test masses were presented in this thesis.

We have discussed the allowable density inhomogeneities and thermal distortion of STEP test masses by using a general formula that we derived to describe acceleration of STEP test masses with arbitrary density distribution. Previously during the process of the optimization of STEP test masses, a simpler formula assuming a homogeneous density distribution was used.

We have measured the density inhomogeneities of the candidate materials (HIPed beryllium and niobium) by hydrostatic weighing. Samples were made from the parent rods from which prototype STEP test masses were prepared. Gravitational quadrupole moment (q_{20}, the dominant term to contribute to the differential acceleration) per unit mass, due to the density inhomogeneities, was found to be $(4.8 \pm 3.5) \times 10^{-9}\mathrm{m}^2$ and $(1.4 \pm 0.1) \times 10^{-9}\mathrm{m}^2$ for an outer beryllium test mass and an inner niobium test mass made from the rods, respectively. A source mass (at 250 mm from the test masses) of 45g and 153g for the beryllium and the niobium respectively, rotating around the test

masses at the signal frequency, produces a spurious acceleration of $10^{-17}\mathrm{m/s^2}$ at the signal frequency, by coupling to those quadrupole moments.

Beryllium is most likely to have a significant level of thermal distortion among the other candidate materials because of its hexagonal crystal structure. We have developed a device to measure differential thermal expansion of the beryllium samples. This device includes mounting systems for samples that cannot be machined. The differential thermal expansion of the beryllium samples, used for the density inhomogeneity measurements, were measured non-destructively by using this device. If the measured maximum differential thermal expansion (0.9 ± 0.3 %) occurs in an outer STEP test mass as anisotropic thermal expansion and the aspect ratio is changed, the quadrupole moment per unit mass becomes $(1.0 \pm 0.4) \times 10^{-8}\mathrm{m^2}$. To achieve the STEP sensitivity of $10^{-17}\mathrm{m/s^2}$, a source mass, rotating around the test masses at signal frequency 250 mm away from test masses, has to be less than 15 g.

The contributions from the metrological aspects of test masses to the spurious acceleration seem small compared to that from the shape of the test masses. The perfect STEP test masses allow a maximum source mass of about 5 g at 250 mm from the test masses. The aerogel confinement techniques and the two-chamber helium dewar are required to restrict a helium bubble to be less than 5 g.

We have discussed appropriate grades of HIPed beryllium and preparation methods of beryllium STEP test masses. The grades made of impact ground powder, such as I70 and I220, which were originally developed for thermally stable large mirrors, would

have sufficient thermal dimensional stability. According to literature and our results of the measurements of differential thermal expansion, extensive stress relief of HIPed beryllium test masses after the final machining seems important to prevent thermal distortion.

By using the mounting system we developed, it may be possible to measure thermal expansion and anisotropy in thermal expansion of STEP test masses in their final shapes.

Appendix A

Spherical harmonics

Spherical harmonics ($Y_{lm}(\theta, \phi)$) used in this work follow the definition in [56]. The followings were used in calculations in this work.

$$Y_{00} = \frac{1}{\sqrt{4\pi}} \tag{A.1}$$

$$Y_{10} = \sqrt{\frac{3}{4\pi}} \cos\theta \tag{A.2}$$

$$Y_{20} = \sqrt{\frac{5}{4\pi}} \left(\frac{3}{2} \cos^2\theta - \frac{1}{2} \right) \tag{A.3}$$

$$Y_{21} = -\sqrt{\frac{15}{8\pi}} \sin\theta \cos\theta e^{i\phi} \tag{A.4}$$

$$Y_{22} = \frac{1}{4}\sqrt{\frac{15}{2\pi}} \sin^2\theta e^{2i\phi} \tag{A.5}$$

$$Y_{30} = \sqrt{\frac{7}{4\pi}} \left(\frac{5}{2} \cos^3\theta - \frac{3}{2} \cos\theta \right) \tag{A.6}$$

$$Y_{32} = \frac{1}{4}\sqrt{\frac{105}{2\pi}} \sin^2\theta \cos\theta e^{2i\phi} \tag{A.7}$$

Appendix B

Analysis of density inhomogeneities with simpler functions

The simplified fitting functions are as follows for the beryllium and the niobium, respectively:

$$\rho_{Be}(x,y,z) = \rho_{Be0}(1 + a_1x + a_2y + a_3z + a_4x^2 + a_5y^2 + a_6z^2 + a_7xy) \quad \text{(B.1)}$$

$$\rho_{Nb}(x,y) = \rho_{Nb0}(1 + b_1x^2 + b_2y^2) \quad \text{(B.2)}$$

where ρ_{Be0} and ρ_{Nb0} are the density of a beryllium and niobium standard sample, respectively. The values for the fitted coefficients and their uncertainties are given in Table B.1 and B.2. χ was 5.7 and 1.8 for the beryllium and the niobium, respectively.

As a result, the extra quadrupole moments due to the density inhomogeneities (q_{20}/I_Z) were found to be $(3.8 \pm 4.0) \times 10^{-6}$ or $< 7.7 \times 10^{-6}$ and $(7.7 \pm 0.7) \times 10^{-6}$ for an outer test mass made from the beryllium rod and an inner test mass made from the niobium rod, respectively. Using Equation (3.16), we estimated that these quadrupole moments would produce a spurious acceleration of $\Delta a = (3.6 \pm 3.7) \times 10^{-19}\mathrm{m/s^2}$ or $< 7.3 \times 10^{-19}\mathrm{m/s^2}$ and $(1.1 \pm 0.1) \times 10^{-19}\mathrm{m/s^2}$ for the beryllium outer test mass and

a_1	$(1.1 \pm 0.2) \times 10^{-6}$	mm^{-1}
a_2	$(-2.9 \pm 0.2) \times 10^{-6}$	mm^{-1}
a_3	$(-2.5 \pm 1.0) \times 10^{-7}$	mm^{-1}
a_4	$(1.5 \pm 1.2) \times 10^{-8}$	mm^{-2}
a_5	$(1.8 \pm 1.2) \times 10^{-8}$	mm^{-2}
a_6	$(1.3 \pm 0.9) \times 10^{-8}$	mm^{-2}
a_7	$(2.8 \pm 1.4) \times 10^{-8}$	mm^{-2}

Table B.1: Coefficients in function (B.1), which fits the beryllium results in Table 5.3.

b_1	$(-2.4 \pm 0.3) \times 10^{-7}$	mm^{-2}
b_2	$(-2.2 \pm 0.3) \times 10^{-7}$	mm^{-2}

Table B.2: Coefficients in function (B.2), which fits the niobium results in Table 5.4.

the niobium inner test mass, respectively. We note that these spurious accelerations are equivalent to the gravitational susceptibilities of $\chi_a = (0.33 \pm 0.35)$ or < 0.68 ppm and (0.1 ± 0.01) ppm for the beryllium and the niobium, respectively.

Appendix C

Dissection plan of new samples

RevNo	Revision note	Date	Signature	Checked

Projection (3rd Angle)

Dimensions in mm.
Tolerance 0.1 mm unless otherwise listed
Number of samples: 65
Each samples to be numbered.
The numbering method is in another drawing.

Part No.	Name	QTY
A	End Piece	16
B	Short End Piece	16
C	Curved Piece	8
D	Core Cube	5
E	Core Segment	20

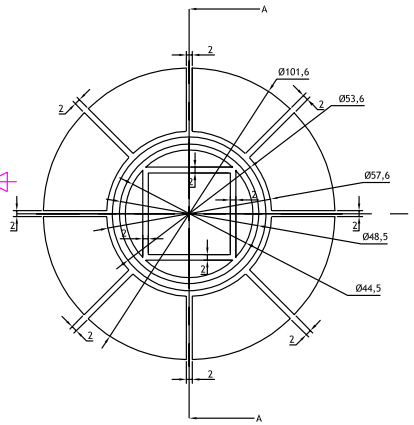

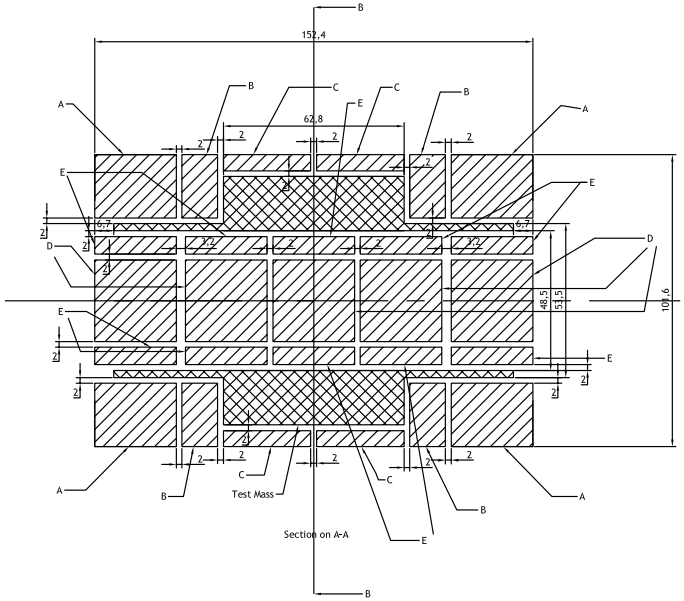

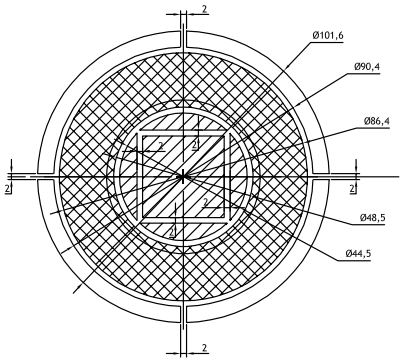

Itemref	Quantity	Title/Name, designation, material, dimension etc			Article No /Reference	
Designed by Sachie Shiomi		Checked by CC Speake and B Probyn	Approved by - date	File name ssNbBe5.dwg	Date 12/03/01	Scale 1:1
Birmingham University		Dissection of Nb and Be			Edition 0	Sheet 1/1

RevNo	Revision note	Date	Signature	Checked

Projection (3rd Angle)

Dimensions in mm.

Tolerance 0.1 mm unless otherwise listed.

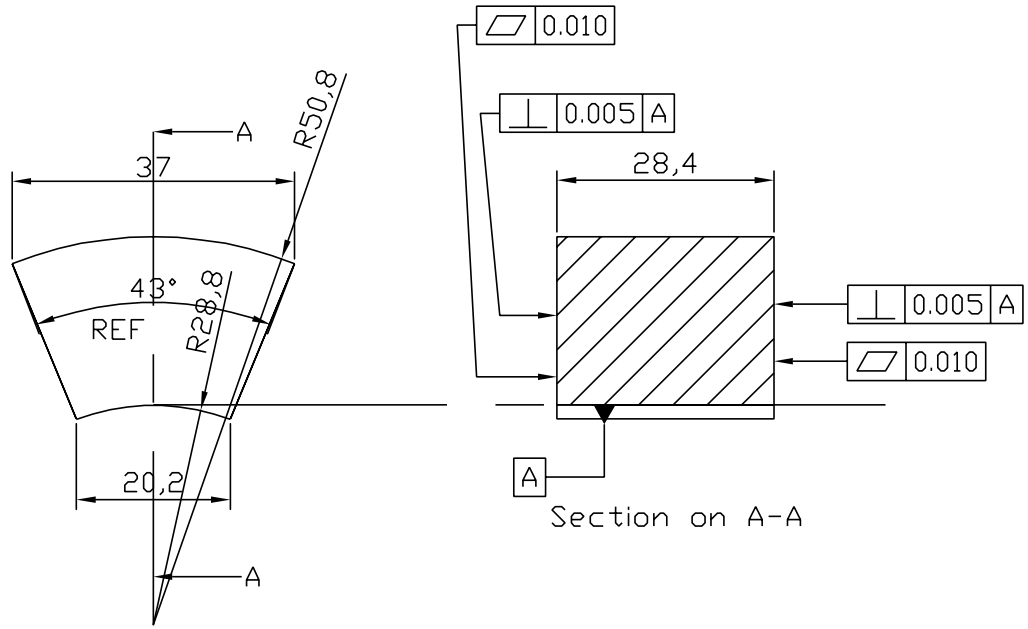

16 samples required

Itemref	Quantity	Title/Name, designation, material, dimension etc			Article No./Reference	
Designed by Sachie Shiomi		Checked by CC Speake	Approved by - date	File name ss1.dwg	Date 29/01/01	Scale 1:1
Birmingham University		End Piece				
		A		Edition 0	Sheet 1/1	

RevNo	Revision note	Date	Signature	Checked

Dimensions in mm.

Tolerance 0.1 mm.

Projection (3rd Angle)

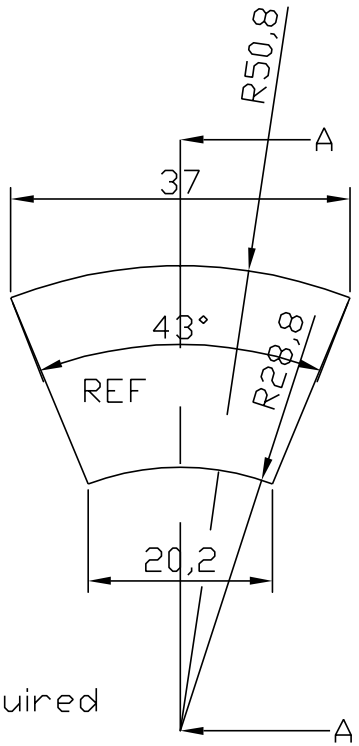

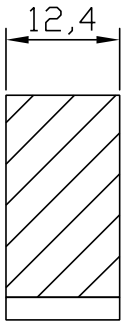

Section on A-A

16 samples required

Itemref	Quantity	Title/Name, designation, material, dimension etc			Article No./Reference	
Designed by Sachie Shiomi		Checked by CC Speake	Approved by - date	File name ss2.dwg	Date 29/01/01	Scale 1:1
Birmingham University		Short End Piece				
		B			Edition 0	Sheet 1/1

RevNo	Revision note	Date	Signature	Checked

Dimensions in mm.

Tolerance 0.1 mm.

Projection (3rd Angle)

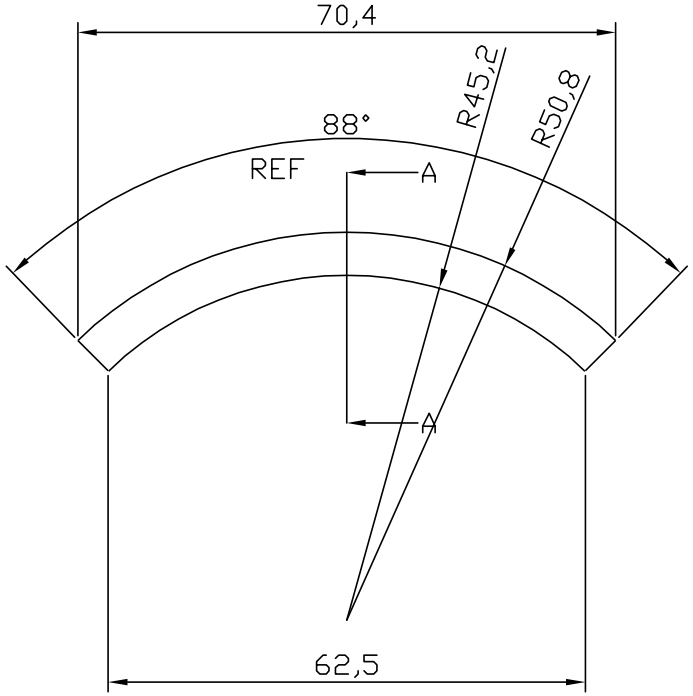

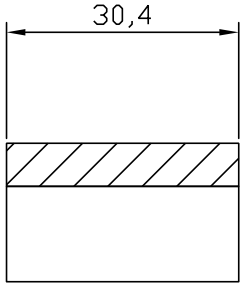

Section on A-A

8 samples required

Itemref	Quantity	Title/Name, designation, material, dimension etc			Article No./Reference	
Designed by Sachie Shiomi		Checked by CC Speake	Approved by - date	File name ss3.dwg	Date 29/01/01	Scale 1:1
Birmingham University		Curved Piece				
		c		Edition 0	Sheet 1/1	

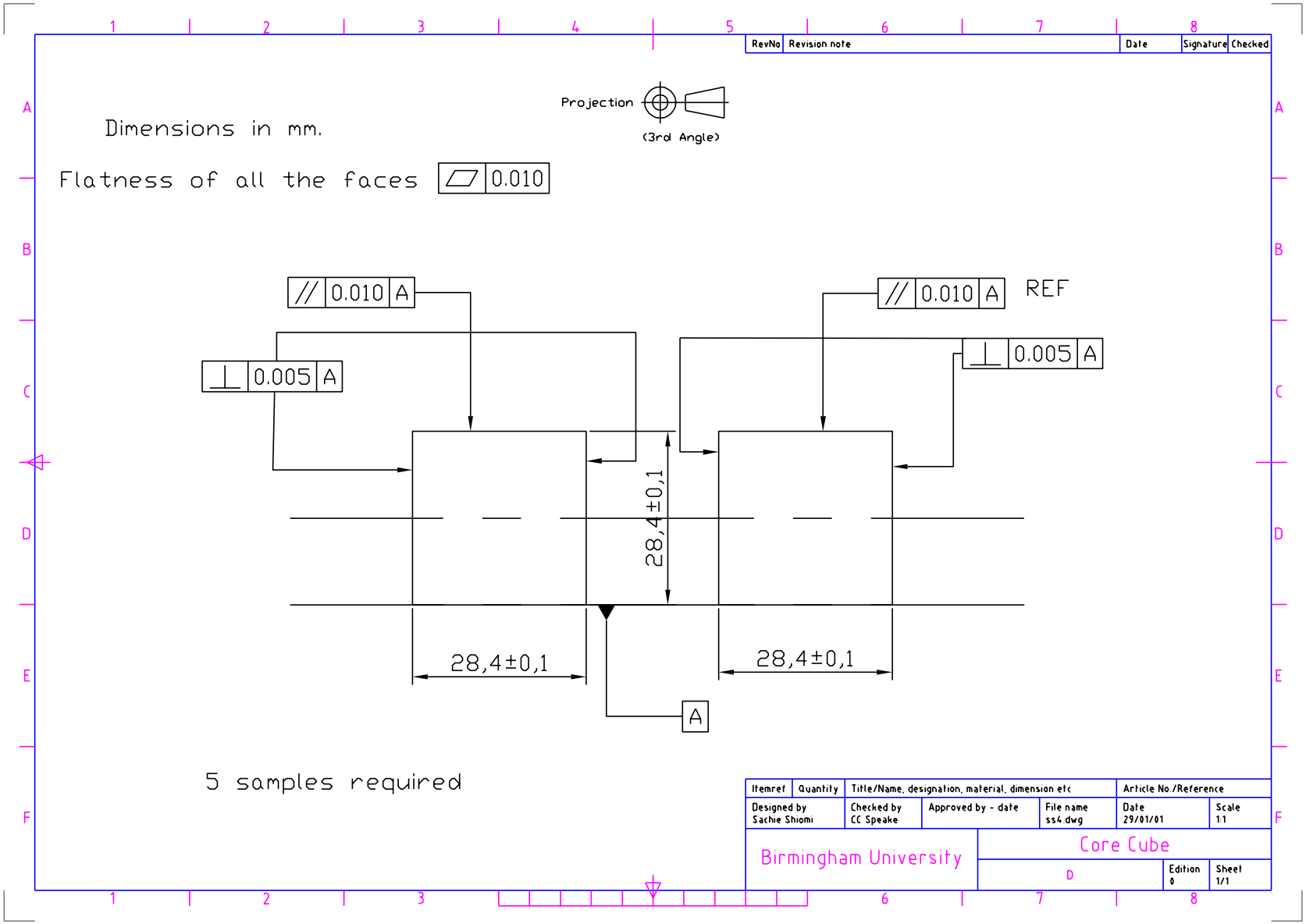
RevNo Revision note
Date
Signature
Checked
Projection
(3rd Angle)
Dimensions in mm.
Flatness of all the faces 0.010
// 0.010 A
⊥ 0.005 A
// 0.010 A REF
⊥ 0.005 A
28,4±0,1
28,4±0,1
28,4±0,1
A
5 samples required
Itemref
Quantity
Title/Name, designation, material, dimension etc
Article No./Reference
Designed by Sachie Shiomi
Checked by CC Speake
Approved by - date
File name ss4.dwg
Date 29/01/01
Scale 1:1
Birmingham University
Core Cube
D
Edition 0
Sheet 1/1

RevNo	Revision note	Date	Signature	Checked

Dimensions in mm.
Tolerance 0.1 mm.

Projection (3rd Angle)

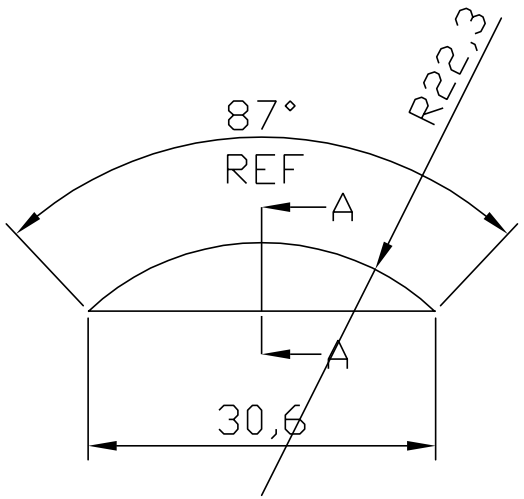

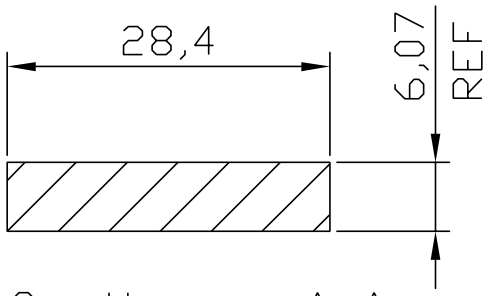

Section on A-A

20 samples required

Itemref	Quantity	Title/Name, designation, material, dimension etc			Article No./Reference	
Designed by Sachie Shiomi		Checked by CC Speake	Approved by - date	File name ss5.dwg	Date 29/01/01	Scale 1:1
Birmingham Univeristy		Core Segment				
		E		Edition 0	Sheet 1/1	

Bibliography

[1] H. Bondi, "Negative mass in general relativity", *Rev. Mod. Phys.* **29**, 423-428 (1957)

[2] R. Utiyama, *Theory of relativity* (Soutaisei riron), Japan: Iwanami syoten, printed in Japanese (1994)

[3] I. Newton, *Principia* (Motte's translation, revised by Cajori), Vol II, edited by R. T. Crawford, University of California Press, Proposition VI. Theorem VI, p. 411 (1962)

[4] S. Weinberg, *Gravitation and cosmology*, John Wiley & Sons, Inc. (1972)

[5] C. M. Will, *Theory and experiment in gravitational physics*, Cambridge University Press (1993)

[6] A. Einstein, "On the influence of gravitation on the propagation of light", *The principle of relativity*, translated by W. Perrett and G. B. Jeffery, New York:Dover Publications, Inc., 99-108 (1952), translated from "Über den Einfluss der Schwerkraft auf die Ausbreitung des Lichtes" *Annalen der Physik*, 35 (1911)

[7] A. Einstein, "The foundation of the general theory of relativity", *The principle of relativity*, translated by W. Perrett and G. B. Jeffery, New York:Dover Publications, Inc., 111-164 (1952), translated from "Die Grundlage der allgemeinen Relativitätstheorie", *Annalen der Physik*, 49 (1916)

[8] K. Nordtvedt, "Equivalence principle for massive bodies. I. Phenomenology.", *Phys. Rev.* **169**, 1014-1016 (1968)

[9] K. Nordtvedt, "Equivalence principle for massive bodies. II. Theory.", *Phys. Rev.* **169**, 1017-1025 (1968)

[10] S. Baeβler et al., "Improved test of the equivalence principle for gravitational self-energy", *Phys. Rev. Lett.* **83**, Num. 18, 3585-3588 (1999)

[11] N. Sakai, *Particle physics* (Soryushi buturigaku), Japan: Baifuukan Ltd., printed in Japanese (1996)

[12] T. D. Lee and C.N. Yang, "Conservation of heavy particles and generalised gauge transformations", *Phys. Rev.* **98**, p. 1501 (1955)

[13] E. Fischbach and C. L. Talmadge, *The Search for Non-Newtonian Gravity*, Springer-Verlag New York, Inc. (1999)

[14] K. Jagannathan and L.S.P. Singh, "Attraction/repulsion between like charges and the spin of the classical mediating field", *Phys. Rev. D* **33**, 2475-2477 (1986)

[15] C. Trenkel, *Development of a superconducting torsion balance designed to search for a new shart-range force coupling quantum mechanical spin and matter*, Ph. D. thesis, University of Birmingham, Edgbaston, Birmingham, UK (1997)

[16] G. D. Hammond, *Development of a shperical superonducting torsion balance for weak force physics*, Ph. D. thesis, University of Birmignham, Edgbaston, Birmingham, UK (1999)

[17] M. Kaku and J. T. Thompson, *Beyond Einstein (The cosmic quest for the theory of unverse)*, Japanese translation by K. Kushimoto, edited by T. Hirose, Tokyo: Koudanshia (1997)

[18] K. Abe, "Graviton", *Elementary particles* (Soryushi), Japan: Saiensu-sha Ltd., printed in Japanese, 34-36, April 1998

[19] H. Takeda, "Supersymmetric particles", *Elementary particles* (Soryushi), Japan: Saiensu-sha Ltd., printed in Japanese, 86-90, April 1998

[20] T. Damour and A. M. Polyakov, "The string dilaton and a least coupling principle", *Nucl. Phys. B* **423**, 532-558 (1994)

[21] P. Fayet, "A new long-range force?", *Phys. Lett. B* **171**, 261-266 (1986)

[22] Y. Fujii, "Dilaton and possible non-newtonian gravity", *Nature: Phys. Sci.* **234**, 5-7 (1971)

[23] T. R. Taylor and G. Veneziano, "Dilaton couplings at large distances", *Phys. Lett. B* **213**, 4, 450-454 (1988)

[24] S. Dimopoulos and G. F. Giudice, "Macroscopic forces from supersymmetry", *Phys. Lett. B* **379**, 105-114 (1996)

[25] E. G. Adelberger et al., "Searches for new macroscopic forces", *Annu. Rev. Nucl. Part. Sci.* **41**, 269-320 (1991)

[26] R. H. Dicke, "The Eötvös experiment", *Sci. Am.* **205**, 81-94 (1961)

[27] Y. Su et al., "New tests of the universality of free fall", *Phys. Rev. D* **50**, 3614-3636 (1994)

[28] G. L. Smith et al., "Short-range tests of the equivalence principle", *Phys. Rev. D* **61**, 022001 (1999)

[29] E. G. Adelberger et al., "Testing the equivalence principle in the field of the Earth: Particle physics at masses below 1 eV?", *Phys. Rev. D* **42**, 3267-3292 (1990)

[30] J.H. Gundlach et al., "Short-range test of the equivalence principle", *Phys. Rev. Lett.* **78**, 2523-2526 (1997)

[31] J. K. Hoskins et al., "Experimental test of the gravitational inverse-square law for mass separations from 2 to 105 cm", *Phys. Rev. D* **32**, 3084-3095 (1985)

[32] V. B. Braginskii and V. I. Panov, "Verification of the equivalence of inertial and gravitational mass", *Sov. Phys. JETP* **34**, 463-466 (1972)

[33] K. Fujimoto, "Experimental verifications of gravitational theories", *Gravitational theories* (Jyuryoku riron), Japan: Saiensu-shia Ltd, printed in Japanese, 21-28, October 1999.

[34] R. Newman, "Prospects for terrestrial equivalence principle tests with a cryogenic torsion pendlum", *Class. Quantum. Grav.* **18**, 2407-2415 (2001)

[35] C. S. Unnikrishnan, "Experimental gravitation in India: progress and challenges", *Class. Quantum Grav.* **11**, A195-A206 (1994)

[36] J. O Dickey et al., "Lunar Laser Ranging: A continuing legacy of the Appllo program" *Science* **265**, 482-490 (1994)

[37] C. Talmadge et al., "Model-independent constraints on possible modifications of Newtonian gravity", *Phys. Rev. Lett.* **61**, 1159-1162 (1988)

[38] J. P. Blaser et al., *STEP Report on the phase A study*, SCI(96)5, ESA, March 1996

[39] P. W. Worden, *A cryogenic test of the Equivalence Principle*, Ph. D. thesis, Stanford University, Stanford, California (1976)

[40] *STEP Phase A report*, in preperation (1998)

[41] J. Mester, "The STEP mission: principles and baseline design", *Class. Quantum. Grav.* **18**, 2475-2468 (2001)

[42] *STEP Phase A report*, in preparation (2001)

[43] J. P. Blaser et al., *STEP Report on the phase A study*, SCI(93)4, ESA/NASA, March 1993

[44] P. Worden, J. Mester and R. Torii, "STEP error model development", *Class. Quantum Grav.* **18**, 2543-2550 (2001)

[45] N. A. Lockerbie, "A dynamical technique for measuring the gravitational quadrupole coupling of the STEP and μSCOPE experimenal test masses", *Class. Quantum Grav.* **17**, 4195-4206 (2000)

[46] C. C. Speake, "Further notes on possible mass designs for the STEP WEP accelerometers", *STEP study report*, 7th November 1992

[47] R. Dolesi et al., "Effect of gravity on helium II in aerogel", *Adv. Space Res.* **25**, 1215-1218 (2000)

[48] S. Wang, R. Torii and S. Vitale, "Silica aerogel vibration testing", *Class. Quantum Grav.* **18**, 2551-2559 (2001)

[49] T. Damour, "Testing the equivalence principle: why and how?", *Class. Quantum Grav.* **13**, A33-A41 (1996)

[50] P. Touboul and M. Rodrigues, "The MICROSCOPE space mission", *Class. Quantum Grav.* **18**, 2487-2498 (2001)

[51] http://www.onera.fr/dmph/accelerometre/conferences.html

[52] B. Foulon, Personal communication, 11th April, 2000

[53] A. M. Nobili et al., "Galileo Galilei (GG) Proposed space experiment to test the Equivalence Principle and preliminary results from the prototype on the ground", to appear in Proceedings of 1999 NASA/JPL International Conference on Fundamental Physics in Space

[54] *Galileo Galilei Phase A report*, http://eotvos.dm.unipi.it/ nobili/ggweb/phaseA

[55] N. A. Lockerbie, A. V. Veryaskin and X. Xu, "Differential gravitational coupling between cylindrically-symmetric, concentric test masses and an arbitrary gravitational source: relevance to the STEP experiment", *Class. Quantum Grav.* **10**, 2419-2430 (1993)

[56] J. D. Jackson, *Classical electrodynamics*, 3rd edition, John Wilery & Sons, Inc. (1998)

[57] S. Shiomi et al., "Measurement of density inhomogeneities in HIPed beryllium and niobium for STEP test masses", *Class. Quantum Grav.* **18**, 2533-2541 (2001)

[58] Christian D'Urso and E. G. Adelberger, "Translation of multipoles for a 1/r potential", *Phys. Rev. D* **55**, 7970-7972 (1997)

[59] E. U. Condon and G. H. Shortley, *The theory of atomic spectra*, Cambridge Univesrity Press, Table 2^3, p. 76 (1935).

[60] C. C. Speake, Personal communication, April 2001

[61] C. C. Speake et al, "A report on metrological consideration for the construction of the mini-STEP test-masses", *STEP study report*

[62] S. Shiomi, *Preliminary study to estimate disturbance from gravitational quadrupole moments couplings due to density inhomogeneities and thermal distortion of test masses for STEP*, Mid-Course Report, School of Physics and Astronomy, The University of Birmingham, 15th December 1999

[63] A. Connes, T. Damour and P. Fayet, "Aspherical gravitational monopoles", *Nucl. Phys. B* **490**, 391-431 (1997)

[64] J. W. Barrett, "The asymmetric nomopole and non-newtonian forces", *Nature* **341**, 131-132 (1989)

[65] A. H. Cook, "A new determination of the constant of gravitation", *Contemp. Phys.* **9**, 227-238 (1968)

[66] "Test Mass, Outer", Drawing No. SU98-100007, STEP, Stanford university, W. W. Hansen Experimental Physics Laboratory, Stanford, CA 94305-1927

[67] "Test Mass, Inner", Drawing No. SU98-100000, STEP, Stanford university, W. W. Hansen Experimental Physics Laboratory, Stanford, CA 94305-1927

[68] R. S. Davis and T. J. Quinn, "Density inhomogeneity as determined by hydrostatic weighing", *Proceedings of the STEP Symposium Pisa Italy, 6-8 April 1993*, 283-

289, edited by R. Reinhard (European Space Agency publication ESA WPP-155, 1996)

[69] C. C. Speake, Personal communication, February 2002

[70] J. Mester, Personal communication, July 2001

[71] M. P. Fitzgerald et al., "A method to measure Newton's gravitational constant", *Metrol.* **31**, 301-310 (1994)

[72] T. J. Quinn et al., "A new determination of G using two methods", *Phys. Rev. lett.* **87**, Num. 11, 111101 (2001)

[73] R. S. Davis, Personal communication, August 2000

[74] D. K. Gill, Personal communication, 30th April 2001

[75] R. S. Davis, Personal communication, February 2001

[76] Y. S. Touloukian et al., *Thermal Expansion (Metallic elements and alloys)*, Volume 12 of Thermophysical Properties of Matter, edited by Y. S. Touloukian and C. Y. Ho, New York-Washington: IFI/Plenum (1975)

[77] Y. S. Touloukian et al., *Thermal Expansion (Metallic elements and alloys)*, Volume 13 of Thermophysical Properties of Matter, edted by Y. S. Touloukian and C. Y. Ho, New York-Washington: IFI/Plenum (1975)

[78] C. A. Swenson, "HIP beryllium: Thermal expansivity from 4 to 300 K and heat capacity from 1 to 108 K" *J. Applied Physics* **70**, No. 6, 3046 - 3051 (1991)

[79] W. R. Goggin and J. W. Moberly, "Thermal dimensional instabilities of beryllium mirrors", *Appl. Optics* **9**, No 12, 2691-2696 (1970)

[80] R. A. Paquin, "Hot isostatic pressed beryllium for large optics", *Opt. Eng.* **25**, No. 9, 1003-1008 (1986)

[81] A. A. Fahmy and A. N. Ragai, "Thermal-expansion behavior of two-phase solids", *J. Applied Physics* **41**, Num 13, 5108-5111 (1970)

[82] National Astronomical Obserbatory, *Rika Nenpyo*(Chronological Scientific Tables 2001), Japan: Maruzen Co., Ltd., printed in Japanese (2000)

[83] G. K. White, "Reference materials for thermal expansion: certified or not?", *Thermochim. Acta* **218**, 83-99 (1993)

[84] G. K. White and R.B. Roberts, "Thermal expansion of reference materials: tungsten and α-Al_2O_3", *High Temp. High Pressures* **15**, 321-328 (1983)

[85] B. Valder, Personal communication, August 2001

[86] *Beryllium Science and Technology, Vol 2*, edted by D. R. Floyd and J. N. Lowe, New York and London: Plenum Press (1979)

[87] G. F. Tikhinskij et al., "New beryllium materials", *J. Nucl. Mater.*, 233-237, p.p. 828-831 (1996)

[88] R. A. Paquin, Personal communication, 12th July 2001

[89] J. S. Browder, "Low-temperature thermal expansion of beryllium as an optical material", *1986 Anual Meeting · Opt. Soc. Am. J.*, p. 83 (1986)

[90] R. A. Paquin et al, "New fabrication process for dimensionally stable beryllium mirrors", *SPIE Int. Soc. Opt. Eng. Proc.* **2775**, 481-490 (1996)

[91] D. H. Hashiguchi and J. M. Marder, "Property evaluation of spherical beryllium powder billets", *Advances in Powder Metallurgy*, Volume 2, Princeton, N.J.: Metal Powder Industries Federation, 37-49 (1990)

[92] T. B. Parsonage, "Advances in beryllium optical technology utilizing spherical powder", *SPIE Astronomy confrence*, MAO-004-1, March 1998

[93] T. B. Parsonage, Personal communication, July 2001

[94] D. K. Gill, Personal communication, 19th Sepbember, 2001

[95] D. G. Michel, "Cryogenic holographic distortion testing", *SPIE Proc.* **2227**, 2-6 (1994)

[96] G. C. Augason and et al., "Cryognic distortion, at 4.4 K, of a 50 cm diameter, spherical, beryllium mirror fabricated to reduce cryogenic distortion and hysterisis", *SPIE Vol.* **2543**, 141-151 (1995)

[97] G. K. White, "Measurement of thermal expansion at low temperature", *Cryogenics*, 151-158 (1961)

[98] C-C. Chang, Personal communication, February 2002

[99] Instruction manual, *Type 1615-A capacitance bridge Type 1620-A, -AP capacitance measuring assembly*, General Radio Company, March 1968

[100] L. Hartshorn, *Radio-frequency measurements by bridge and resonance methods*, Chapman & Hall Ltd. (1941)

[101] *Farnell Catalogue*, Farnell

[102] T. Quinn, Personal Communication, December 2001

[103] "Potential health effects from exposure to beryllium", *Brush Wellman technical sheet, Safety Facts*, SF200 - Version 1.2, June 1999

[104] H. J. J. Braddick, *The physics of experimental method*, 2nd edition, Chapman & Hall Ltd, London, Chapter 3.2, 1963

[105] R. J. Roark, *Formulas for stress and strain*, 3rd edition, McGRAW-HILL BOOK COMPANY, Inc., p. 287 (1954)

[106] Catalogue, *MACOR® (machinable glass ceramic)*, Corning Limited, p 5

[107] A. R. Rosenfield and B. L. Averbach, "Effects of stress on expansion coefficient", *J. Applied Physics* **27**, No. 2, 154- 156 (1956)

[108] *Science data book*, edited by R. M. Tennent, Oliver & Boyd (1998)

[109] *Goodfellow Catalogue*, Goodfellow

[110] N. A. Lockerbie, "Dynamical measurements of the gravitational quadrupole coupling to experimental test masses", *Class. Quantum Grav.* **18**, 2521-2531 (2001)

[111] C. Trenkel and C. C. Speake, "Direct measurements of STEP test mass quadrupole moments", submitted to *Class. Quantum Grav.*, 2002

[112] H. M. Ledbetter and E. R. Naimon, "Elastic properties of metals and alloys. II. Copper", *J. Phys. Chem. Ref. Data* **3**, No. 4, 897-935 (1974)